Properties and Applications of the Photorefractive Material Ce:KNSBN

Meisong Ding

A thesis submitted in partial fulfillment of the requirements
for the degree of Doctor of Philosophy

Sponsoring Establishment: University of Abertay Dundee
Submitted: November 2000

I certify that this thesis is the true and accurate version of the
thesis approved by the examiners.

Signed [redacted] (Director of Studies) Date 22 January 2001

Declaration

I hereby declare that while registered as a candidate for the degree for which this thesis is presented I have not been a candidate for any other award. I further declare that, except where stated, the work in this thesis is original and was performed by myself.

Acknowledgements

I would like to thank my supervisors, Dr. Colin Cartwright and Prof. Allan Gillespie for their kindness, patience and assistance throughout the time of my research. Thanks to Prof. Zhaoqi Wang for his helpful suggestions, and the University of Abertay Dundee for the financial support during my study.

All the academic staff, technical staff and secretaries in the School of Science and Engineering have been very helpful with all aspects of life as a postgraduate.

I would also like to thank my fellow students for their kindness throughout my time in the EPI Centre.

Properties and Applications of the Photorefractive Material Ce:KNSBN

Meisong Ding

Abstract

Ce:KNSBN is a new photorefractive material in the KNSBN family, which has some advantages compared to other crystals. Based on two-wave mixing theory, different methods are used to investigate the photorefractvie properties of the Ce:KNSBN crystal. Most parameters of the Ce:KNSBN crystal are in the same orders with those of Cu:KNSBN crystal.

The diffraction efficiency from the Ce:KNSBN crystal is affected by the applied electric field. The applied field increases the response rate of the grating formation and enhances the diffraction efficiency. There exists an optimum applied field and grating spacing related to the maximum diffraction efficiency, and the history of applied field influences the value of diffraction efficiency. Fanning loss and thermal effects should be considered in the diffraction theory for the Ce:KNSBN crystal.

The phase conjugate properties of the Ce:KNSBN crystal are demonstrated in the four-wave mixing configuration and in the SPPC CAT conjugator. The experimental results agree with the analytical solution under some conditions. The He-Ne laser generates higher SPPC in the Ce:KNSBN crystal than that by the argon-ion laser. The Doppler frequency detuning technique is first, to our knowledge, applied in the SPPC CAT configuration. The SPPC reflectivity is enhanced and the uniformity of the reflectivity is improved by this technique.

List of Symbols

Roman Letters:

A_j	Amplitude of jth beam
$\vec{E}$	Electric field
E_0	Applied electric field
E_1	Space-charge field (stead-state)
E_d	Diffusion field
E_W	Normalised space charge field
E_q	Saturation field
E^{sc}	Space-charge field
G	Effective gain
G_e	Enhancement coefficient
I	Beam intensity
I_j	Intensity of jth beam
I_0	Total Intensity
I_s	Saturation Intensity
$\hbar$	Planck's constant divided by 2π
$\vec{j}$	Current density
k_B	Boltzmann's constant
$\vec{k}_j$	Wave number of jth beam
$\vec{K}$	Grating vector
	(K, the magnitude of the grating vector)
L	Crystal thickness
L_d	Diffusion length
m	Input intensity ratio
m'	Beam intensity modulation
N_A	Acceptor density

N_D	Donor density
N_D^i	Ionised donor density
N	Density of electrons
N_{eff}	Effective photorefractive charge density
n	Index of refractive
n_0	Unperturbed index of refraction
Δn	Change in refractive index
n_e	Index of refraction for extraordinarily polarized light
n_o	Index of refraction for ordinarily polarized light
q	Charge of an electron
r_{ij}	Electro-optic coefficient
r	Pump beam ratio
r_{eff}	Effective electro-optic coefficient
R_c	Phase conjugate reflectivity
s	Photoexcitation cross section
t	Time
T	Absolute temperature

Greek Letters:

α	Intensity absorption
β	Propagation constant
β_T	Thermal emission rate
$<\varepsilon>$	Dielectric constant
ε_0	Free space permittivity
ε	Relative dielectric constant
ϕ	Phase shift of intensity interference pattern
Φ	Space charge grating phase shift
Γ	Coupling gain coefficient
γ	Real part of the coupling gain coefficient

γ_R	Electron-ionized trap recombination rate
η	Diffraction efficiency
φ	Slant angle of the grating
κ_c	Coupling constant
$\Lambda(\Lambda_g)$	Grating spacing
λ	Optical wavelength
μ	Carrier mobility
μ_0	Free space permeability
ω	Angular optical frequency
θ	Incident angle of writing beams
ρ	Propagation vector
ρ^{sc}	Space-charge density
ρ_0	Optical activity
σ	Conductivity
σ_s	Photoionization cross-section
σ_d	Dark conductivity
σ_{ph}	Photoconductivity
τ	Characteristic time constant
τ_R	Recombination time constant
ζ	Hole-electron competition factor

Contents

Chapter 1 Introduction

The photorefractive effect is an optical phenomenon in some electro-optic crystals where the local index of refraction is changed by the spatial variation of the light intensity. It is generally believed to arise from optically generated charge carriers, which migrate when the crystal is exposed to a spatially varying pattern of illumination with photons having sufficient energy. Migration of the charge carriers due to drift, diffusion, and the photovoltaic effect produces a space-charge separation, which then gives rise to a strong space-charge field. Such a field induces a refractive index change via the electro-optic (Pockels) effect. The photorefractive effect can be employed to explain several interesting optical phenomena in these electro-optic crystals — photorefractive materials.

1.1 Motivation for the research

Due to the potential applications in many aspects of optical information processing, such as volume holographic storage, coherent light amplification, optical phase conjugation, optical communication, optical interconnect, and optical computing etc. [1] – [3], the properties of photorefractive materials have been studied with great interest in recent years. Some leading photorefractive crystals, such as $BaTiO_3$, $KNbO_3$, $LiNbO_3$, $LiTaO_3$, $Sr_xBa_{1-x}Nb_2O_6$ (SBN), $(K_{1-y}Na_y)_{2A-2}(Sr_{1-x}Ba_x)_{2-A}Nb_2O_6$ (KNSBN), $Bi_{12}SiO_{20}$ (BSO), $Bi_{12}GeO_{20}$ (BGO), GaAs, InP, CdTe and $Ba_{2-x}Sr_xK_{1-y}Na_yNb_5O_{15}$ (BSKNN) were studied

extensively by many researchers. However, some unexpected properties of the previous photorefractive materials limit their practical applications. For example: $LiNbO_3$ has a relatively lower photorefractive sensitivity and stronger light scattering which decreases the strength of the propagating beam considerably; $KNbO_3$ is easy to crack due to the phase transition from point group *4mm* to *mm2* when it is cooled down to room temperature after the crystal growth; $BaTiO_3$ has excellent photorefractive properties, but is difficult to grow into perfect single crystals, the existence of 90° and 180° domains makes it difficult to pole and it also has a phase transition from point group *4mm* to *mm2* at room temperature; SBN shows good photorefractive properties, but it has a lower Curie point which causes it to be liable to depole. Therefore, looking for new photorefractive materials with high quality and fast response times is a very exciting research field to date. The KNSBN crystal, being first grown and studied by Chen and Xu [4], has shown some advantages, including its larger electro-optic coefficients, a relatively higher Curie temperature (120 – 170 °C, little change with the ratio of K, Na, Sr, Ba), and some excellent mechanical properties. In addition, it is a little easier to grow than some other crystals. Because there are no 90° domains, this kind of crystal is easy to pole.

Our research on the basic properties of the new photorefractive material Ce:KNSBN will enrich the knowledge of the KNSBN family. The specific phenomena and characteristics in Ce:KNSBN crystal would induce some useful applications.

1.2 Samples used in the research

All experiments carried out in this thesis were conducted using two samples of Ce-doped $(K_{1-y}Na_y)_{2A-2}(Sr_{1-x}Ba_x)_{2-A}Nb_2O_6$ (KNSBN) of dimensions $5.0\times5.0\times5.0mm^3$ and $5.5\times5.5\times5.5mm^3$ respectively. Both of them were grown by the pulling method with a Crystalox MCGS-3 System in Shandong University (P. R. China). Their compositions were designed as $A = 1.2$, $x = 0.25$ and $y = 0.5$. The Ce-doping level was 0.04 wt %, the Curie temperature is 130 °C and its 6 faces were polished (1pc).

The electrical contact was made to the sample of dimensions $5.5\times5.5\times5.5mm^3$ by using silver-paint electrodes on the c face, to investigate the applied electric field effects on the diffraction efficiency (chapter 4). The other sample of dimensions $5.0\times5.0\times5.0mm^3$ was used in the experiments of measuring the photorefractive parameters of Ce:KNSBN crystal, the phase conjugate properties, its applications and etc.

1.3 Outline of the thesis

Chapter 2 is the background, where we introduce the photorefractive effect, using the band transport model to discuss the formation of the index grating and giving a general expression of the space-charge field in photorefractive materials. We briefly review the research on KNSBN crystals, and describe the KNSBN crystal structure by comparing it with SBN and BTO crystals. We list some common applications of photorefractive materials.

To investigate the properties of the Ce:KNSBN crystal based on the two wave mixing method, chapter 3 introduces the principle of two wave mixing theory, showing some basic equations of beam coupling, gain and index amplitude etc. Using different methods, we measure, derive and calculate most photorefractive parameters of the Ce:KNSBN crystal.

In chapter 4 the diffraction efficiency of volume gratings in the Ce:KNSBN crystal, especially the effects of applied electric field on the diffraction efficiency are discussed. We introduce Bragg diffraction from the volume gratings, and derive the expression for diffraction efficiency for the transmission gratings. We measure the diffraction efficiency for different applied electric fields and grating spacings, and use different expressions to calculate the diffraction efficiency. We discuss the phenomena observed in our experiment.

Chapter 5 is about phase conjugation. We introduce the general concept of phase conjugation, the analytical solutions under various approximations, and the theory of self-pumped phase conjugation (SPPC). We demonstrate the phase conjugate properties in the four-wave mixing configuration, and compare the experimental results with the theoretical expression based on the one-grating approximation. We measure and discuss the SPPC properties in the CAT configuration, and compare the results from the pumping beams with different wavelengths.

In chapter 6 we are first, to our knowledge, to apply a Doppler frequency detuning technique to the SPPC CAT configuration. We demonstrate that Doppler frequency detuning could not only enhance the SPPC reflectivity, but also improve the uniformity of the reflectivity over a reasonable area. We also discuss the possible mechanism for this useful application.

The last chapter is the summary of our work.

Chapter 1: References

1. L. Solymar, D. J. Webb and A. Grunnet-Jepsen, "The physics and applications of photorefractive materials", Oxford University Press, Oxford, 1996
2. P. Gunter and J. P. Huignard, "Photorefractive materials and their application", Topics in Applied Physics, vols. 61 and 62, Springer, Berlin, 1988
3. P. Yeh, "Introduction to Photorefractive Nonlinear Optics", Wiley, New York, 1993
4. H. Chen and Y. Xu, Physics, vol. 10, p729, 1981

Chapter 2 Background

2.1 Photorefractive Effect

The photorefractive effect is a phenomenon in which the local index of refraction of a medium is changed by the illumination of a beam of light with spatial variation of the intensity [1] - [2]. Such an effect was first discovered in 1966 when researchers found that the transmission of laser beams through electro-optic crystals led to an index inhomogeneity which distorted the wavefront of the transmitted laser beam. The effect was referred to as "Optical Damage" [3]. The photorefractive effect has since been observed in many electro-optic crystals [4] including $BaTiO_3$, $KNbO_3$, $LiNbO_3$, $LiTaO_3$, Sr_xBa_{1-x} Nb_2O_6 (SBN), $Ba_{2-x}Sr_xK_{1-y}Na_yNb_5O_{15}$ (BSKNN), $Bi_{12}SiO_{20}$ (BSO), $Bi_{12}GeO_{20}$ (BGO), GaAs, InP, CdTe and $(K_{1-y}Na_y)_{2A-2}(Sr_{1-x}Ba_x)_{2-A}Nb_2O_6$ (KNSBN). Here, we will briefly discuss a simple physical model that describes most of the observed photorefractive phenomena.

2.1.1 Band Transport Model

We consider a simple model that is very useful for explaining most of the observed photorefractive phenomena. In the model, photorefractive media are assumed to contain certain types of impurities or imperfections [4] – [5]. For the sake of simplicity in explaining the concept, we assume that all donor impurities are identical and have exactly

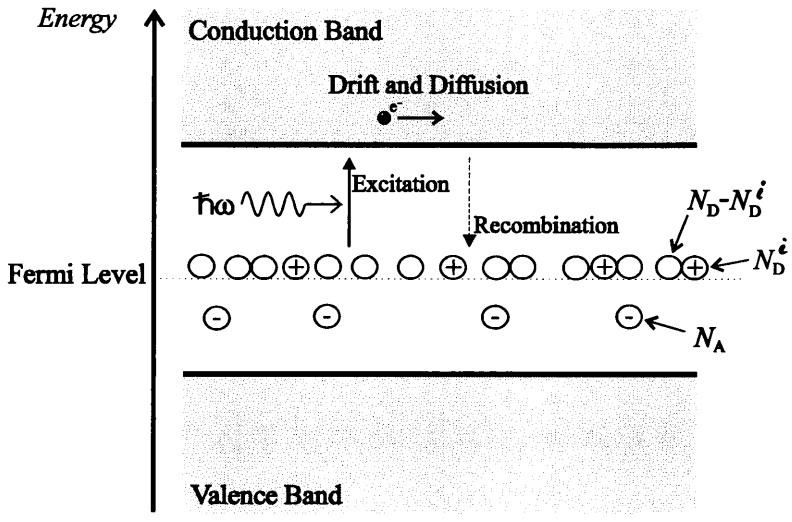

Fig. 2.1 Model of photorefractive effect.

the same energy state somewhere in the middle of the bandgap (see Fig.2.1). These donor impurities can be ionized by absorbing photons. As a result of the ionization, electrons are generated in the conduction band and leave empty states behind. Such ionized impurities are capable of capturing electrons. Let the density of donor impurities be N_D of which N_D^i are ionized. The rate of electron generation is $(sI + \beta)(N_D - N_D^i)$, whereas the ratio of trap capture is $\gamma_R N N_D^i$, where N is the electron density, s is the cross section for photoexcitation, I is the light intensity, β is the rate of thermal generation of electrons and γ_R is the electron-ionized trap recombination rate. The rate equation for N_D^i, neglecting thermal generation of carriers (i.e., $\beta << sI$), can thus be written

$$\frac{\partial N_D^i}{\partial t} = sI(N_D - N_D^i) - \gamma_R N N_D^i \tag{2.1}$$

For every impurity ionized, an electron is generated. On the other hand, an electron is eliminated when a recapture that fills an empty impurity occurs. The rate of generation of electrons is the same as that of the ionized impurities except that the electrons are mobile whereas the impurities are stationary. This is essential for the photorefractive effect. The transport of electrons may affect the electron density. The rate equation for electron density can thus be written

$$\frac{\partial N}{\partial t} - \frac{\partial N_D^i}{\partial t} = \frac{1}{q}\nabla \cdot \vec{j} \tag{2.2}$$

where $\vec{j}$ is the current density and $-q$ is the electron charge ($q = 1.602 \times 10^{-19}$ C). The presence of these charge carriers (electrons) leads to a space-charge field which in turn affects the transport of the carriers. The current density consists of contributions from the drift of charge carriers due to the electric field and the diffusion due to the gradient of carrier density. It can be written

$$\vec{j} = qN\mu\vec{E} + k_B T\mu\nabla N \tag{2.3}$$

where μ is the mobility tensor, $\vec{E}$ is the electric field, $k_B T$ is the product of the Boltzmann constant and temperature. The electric field obeys the following Poisson equation,

$$\nabla \cdot \varepsilon \vec{E} = \rho^{sc}(\vec{r}) = -q(N + N_A - N_D^i) \tag{2.4}$$

where ε is the dielectric tensor, $\rho^{sc}(\vec{r})$ is the charge density, and N_A is the density of acceptor impurity. The presence of acceptor impurities is essential to maintain the charge neutrality. In the absence of light illumination, the charge neutrality is written

$$\left(N + N_A - N_D^i\right) = 0 \tag{2.5}$$

In the case when the electron density is small, we have $N_D^i = N_A$ in the absence of light. In other words, the density of ionized donor impurities equals the density of acceptor impurities. In (2.3), $qN\mu\vec{E}$ represents the current density due to drift, and $k_B T\mu\nabla N$ represents the current density due to diffusion. We have neglected the current due to the photovoltaic effect.

As indicated in Fig. 2.1, there are donor impurities and acceptor impurities. The density of donors is often much larger than that of the acceptor impurities. Here we assume that all acceptors are also identical. In the case when there are no electrons in the conduction band and no holes in the valence band, the density of ionized donor impurities is identical to that of the acceptor impurities. The neutral donor impurities are capable of donating electrons for photexcitation and the ionized ones are capable of capturing these photoelectrons. In the model, the acceptor impurities are for the purpose of charge neutrality only. They do not directly participate in the photorefractive effect.

2.1.2 Formation of the index grating

We now consider the incidence of two laser beams into a photorefractive medium. If the polarization states of these two waves are not orthogonal, they will form an interference pattern. The intensity can be written as

$$I(\vec{r}) = I_0 + \mathrm{Re}\left\{I_1 e^{-i\vec{K}\cdot\vec{r}}\right\} \tag{2.6}$$

where I_0 and I_1 are constants. The magnitude of the grating wave vector is related to the period (Λ) of the interference pattern by $K = 2\pi / \Lambda$.

Consider now the presence of such an intensity inside a photorefractive medium. In the bright regions, photoionized charges are generated by the absorption of photons. These charge carriers can diffuse away from the bright regions leaving behind positively charged ionized donor impurities. If these charge carriers are trapped in the dark regions, they will remain there because there is no light to reexcite them. This leads to a charge separation as depicted in Fig. 2.2. As a result of the illumination with periodic intensity in the photorefractive medium, the dark regions are negatively charged and the bright regions are positively charged (see Fig. 2.2). The buildup of space charge separation will continue until the diffusion current is counterbalanced by the drift current. The space-charge density can thus be written

$$\rho^{sc} = \rho_0{}^{sc} \cos \vec{K} \cdot \vec{r} \tag{2.7}$$

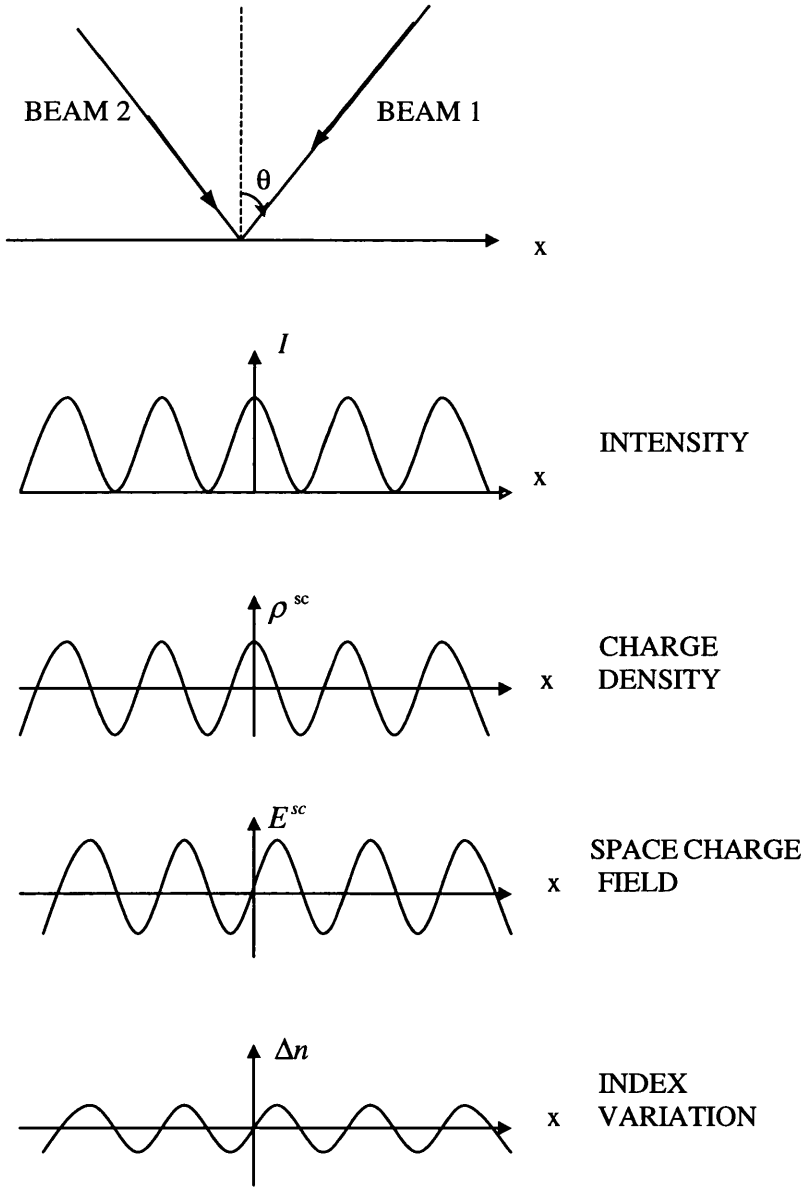

Fig. 2.2. Photorefractive effect.

where ρ_0^{sc} is a constant. An integration of the Poisson Equation (2.4) leads to

$$\vec{E} = \rho_0^{sc} \frac{\vec{K}}{\vec{K} \cdot \varepsilon \vec{K}} \sin\left(\vec{K} \cdot \vec{r}\right) \tag{2.8}$$

We note that the space-charge field is shifted in space by $\pi/2$ relative to the intensity pattern. This space-charge field will induce a change in the index of refraction via the Pockels effect. Figure 2.2 illustrates the spatial variation of the light intensity, space-charge density, space-charge field and the induced index change.

In summary, the photorefractive effect consists of five fundamental processes which occur in electro-optic crystals: 1) photoionization of impurities and the generation of charge carriers, 2) transport of these charge carriers, 3) trapping of charge carriers and the formation of a space-charge density, 4) formation of the photoinduced space-charge electric field, and 5) formation of index grating via the linear electro-optic effect (Pockels' effect). The photorefractive effect is a macroscopic phenomenon and requires the generation and transport of a large number of charge carriers (typically, of the order of 10^{15} cm^{-3}). The speed of grating formation is thus fundamentally limited by the finite time needed to absorb a large number of photons at a given power level [6].

2.1.3 Space-charge field

Given an illumination intensity of (2.6), we need to solve for the space-charge field as a function of both $\vec{r}$ and t using (2.1) – (2.4). Closed form general solutions are, however,

not available. The steady-state solution for the amplitude of the space-charge field is often written [7]

$$E_1 = \frac{iE_d - E_0}{1 + E_d / E_q + iE_0 / E_q} \frac{I_1}{I_0} \tag{2.9}$$

where we assume that $I_1 << I_0$ and the applied electric field is parallel to the grating wave vector, E_0 is the amplitude of the applied field, and E_d, E_q are characteristic fields of the medium given by

$$E_d = K \frac{k_B T}{q}, \qquad E_q = \frac{qN_A}{\langle \varepsilon \rangle K} \tag{2.10}$$

In (2.10), $\langle \varepsilon \rangle = \vec{K} \cdot \varepsilon \vec{K} / (\vec{K} \cdot \vec{K}) = \varepsilon \varepsilon_0$ is the dielectric tensor, ε and ε_0 are the relative dielectric constant and the free space permittivity respectively. The growth of the space-charge field is approximately given by

$$E_0^{sc} = E_1 \left(1 - e^{-t/\tau}\right) \tag{2.11}$$

Where E_0^{sc} is the amplitude of the space-charge field and τ is a characteristic time constant of the medium.

All photorefractive materials are electro-optic crystals. The presence of an electric field in these media induces a change in the index of refraction via the linear electro-optic effect (Pockels' effect):

$$\Delta\left(\frac{1}{n^2}\right)_{ij} = r_{ijk}\ E_k^{sc} \tag{2.12}$$

Where r_{ijk} are the electro-optic coefficients and E_k^{sc} is kth component of the space-charge field. Summation over $k = 1, 2, 3$ (or x, y, z) in (2.12) is assumed. The space-charge field is given by

$$E^{sc} = \mathrm{Re}\left\{E_1 e^{-i\vec{K}\cdot\vec{r}}\right\} \tag{2.13}$$

with E_1 given by (2.9). According to (2.12) and (2.13), a volume index grating is formed when a photorefractive crystal is illuminated by two beams of coherent light. In the case of pure diffusion with $E_0 = 0$, the space charge field is spatially shifted relative to the intensity by $\pi/2$, according to (2.9).

2.2 KNSBN photorefractive crystal

In the past decade most research work on KNSBN crystals has focused on the growth of crystals with improved quality and on the applications using the crystals. Various dopants have been added to the melt during crystal growth to modify the photorefractive

properties of KNSBN crystals. Ce [8], Cu [9, 10], Cr [11] and Mn [12] dopings are found to be effective for the enhancement of the photorefractive response in the visible or NIR spectral regions due to the additional absorption bands of these dopants in KNSBN crystals. A nice trade-off between photorefractive response speed and sensitivity is obtained in Co-doped KNSBN crystals [13].

2.2.1 KNSBN crystal structure

Strontium barium niobate $Sr_xBa_{1-x}Nb_2O_6$ (SBN, $x = 0.61$ for the congruent compound, where melt and crystal have the same composition) with the open tungsten bronze structure has been considered one of the most promising materials because of its large transverse electro-optic coefficient r_{33} [14]. The congruent composition of SBN crystals allows SBN to be grown as large-size crystals with natural facets and free of striations. Based upon the growth techniques of SBN crystals, photorefractive potassium sodium strontium barium niobate $(K_{1-y}Na_y)_{2A-2}(Sr_{1-x}Ba_x)_{2-A}Nb_2O_6$ (KNSBN, with A a filling factor) crystals with filled tungsten bronze structure were successfully developed in the 1980s [14] – [17]. KNSBN crystals resemble $BaTiO_3$ crystals in a lot of aspects. Both crystals have large longitudinal electro-optic coefficients and possess a tetragonal structure at room temperature. However, KNSBN crystals exhibit some advantages over $BaTiO_3$. The phase transition temperature T_c of KNSBN crystals from the paraelectric phase 4/mmm to the ferroelectric phase 4 mm can be controlled by crystal composition. No phase transitions exist near room temperature in KNSBN crystals. $BaTiO_3$ crystals sometimes have a destructive tetragonal-orthorhombic phase transition at about 10 °C,

and 90° domains exist in $BaTiO_3$, making it difficult to keep and handle $BaTiO_3$ crystals in a single domain state at room temperature. KNSBN crystals with large size and free of striations are easily grown, but it is difficult to obtain a large-size $BaTiO_3$ crystal. At room temperature ferroelectric KNSBN crystals belong to the tungsten bronze family of crystals with a general chemical composition formula $(A1)_4(A2)_2C_4B_{10}O_{30}$ where A1, A2, C and B are 15-, 12-, 9- and 6-fold oxygen coordinated sites in the crystal lattice structure. A1 and A2 sites are totally filled by Sr^{2+}, Ba^{2+}, K^+ and Na^+ for the filling factor A = 1.2 and partially filled for $1 \leq A < 1.2$. B sites are filled by Nb^{5+} ions and C sites are completely empty. For comparison, only five of six available A1 and A2 sites (83.3%) are filled by Sr^{2+} and Ba^{2+} in SBN crystals on the average. From the view of ion occupancy, KNSBN crystals have a more orderly structure than SBN crystals.

2.3 Applications of photorefractive materials

There are enormous applications having been proposed for photorefractive materials. Whilst a few prototype devices have been produced that make use of some form of photorefractive signal processing element, these have almost all been constructed as technology demonstrators, and there is to our knowledge only one commercial product on the market [18]. Nevertheless, there is hope that with the rapid progress being made in photorefractive materials research it will not be long before other photorefractive devices do achieve commercial success.

So by applications here we refer to systems that make use of dynamic gratings recorded in photorefractive crystals to perform some (potentially useful) function. The system may consist of just the photorefractive crystal itself or a complex arrangement of many different optical and optoelectronic devices. The common applications of photorefractive materials are as follows:

1) Image amplification and image processing, which include thresholding, edge enhancement, the ability to identify changes in an image (novelty filtering), and spatial light modulation.

2) Pattern recognition, for which the most important operation is correlation.

3) The various issues surrounding the storage and subsequent replay of many images within a single photorefractive crystal: such as multiplexing techniques, storage capacity and recording schedules.

Because of the exceptionally large longitudinal electro-optic coefficients r_{51}, KNSBN crystals would be excellent photorefractive candidates for various nonlinear optical applications like self-pumped phase conjugation, holographic storage and optical waveguide devices.

Chapter 2: References

1. V. L. Vinetskii, N. V. Kukhtarev, S. G. Odulov, and M. S. Soskin, "Dynamic self-diffraction of coherent light beams," Sov. Phys.-Usp., vol. 22, pp. 742-756, 1979.
2. N. V. Kukhtarev, V. B. Markov, S. G. Odulov, M. S. Soskin, and V.L. Vinetskii, "Holographic storage in electro-optic crystals, beam coupling and light amplification," Ferroelectrics, vol. 22, pp. 961-964,1979.
3. A. Ashkin, G. D. Boyd, J. M. Dziedzic, R. G. Smith, A. A. Ballman, J. J. Levinstein, and K. Nassau, "Optically induced refractive index inhomogeneities in $LiNbO_3$," Appl. Phys. Lett., vol. 9, pp. 72-74, 1966.
4. P. Gunter and J. P. Huignad, Photorefractive Materials and Their Applications, I and II., New York: Springer-Verlag, 1987
5. L. Sovymar, D. J. Webb and A. Grunnet-Jepsen, The Physics and Applications of Photorefractive Materials, New York: Oxford University Press, 1996
6. P. Yeh, "Fundamental limit of the speed of photorefractive effect and its impact on device applications and material research," Appl. Opt., vol. 26, pp. 602-605, 1987.
7. P. Yeh and C. Gu, Photorefractive Nonlinear Optics, World Scientific Published Co. Pte. Ltd., Singapore, 1995
8. D. Sun, J. Chen, X. Lu, Y. Song, Z. Shao, H. Chen, J. Xu, Y. Wu, S. Liu, and G. Zhang, J. Appl. Phys., vol. 70, p33, 1991
9. H. Wang, M. Tian, J. Lin, S. Huang, J. Yu, H. Chen and G. Jiang, Opt. Comm., vol. 115, p563, 1995
10. H. Zhang, B. Guo, H. Jiang, Y. Shih and L. Yan, Appl. Phys. B, vol. 61, p207, 1995
11. J. Bergquist, Y. Tomita and M. Shibata, Appl. Phys. A, vol. 55, p61, 1992

12. Y. L. Zhang, X. S. Xie, D. Mo, E. Y. B. Pun and L. P. Shi, J. Appl. Phys., vol. 79, p8835, 1996

13. Y. Li, S. Liu, M. Yang, K. Yang, K. Xu and F. Hou, Opt. Lett., vol. 22, p212, 1997

14. R. R. Neurgaonkar, W. K. Cory, J. R. Oliver, M. D. Ewbank and W. F. Hall, Opt. Eng. Vol. 26, p392, 1987

15. H. Chen and Y. Xu, Physcis, vol. 10, p729 (1981)

16. R. R. Neurgaonkar, W. K. Cory, J. R. Oliver, W. W. Clark III, G. L., Wood, M. J. Miller and E. J. Sharp, J. Cryst. Growth, vol. 84, p629, 1987

17. H. Chen and Y. Xu, J. Cryst. Growth, vol. 96, p357, 1989

18. G. A. Rakuljic and V. Leyva, "Volume holographic narrow band optical filter", Opt. Lett. 18, pp459-461, 1993

Chapter 3 Wave mixing in photorefractive media

When two beams of coherent electromagnetic radiation intersect inside a photorefractive medium, the periodic variation of the intensity due to interference will induce a volume index grating. The grating wave vector is given by $\vec{K} = \pm(\vec{k}_2 - \vec{k}_1)$, where $\vec{k}_1$ and $\vec{k}_2$ are wavevectors of the beams. The presence of the index grating affects the propagation of these two beams. In fact, these waves are strongly diffracted by the index grating because Bragg scatterings are perfectly phase-matched. Thus beam 1 is propagating along the direction of beam 2. Similarly beam 2 is scattered by the same grating and the diffracted beam is propagating along the direction of beam 1. This leads to energy coupling and the scattering known as self-diffraction.

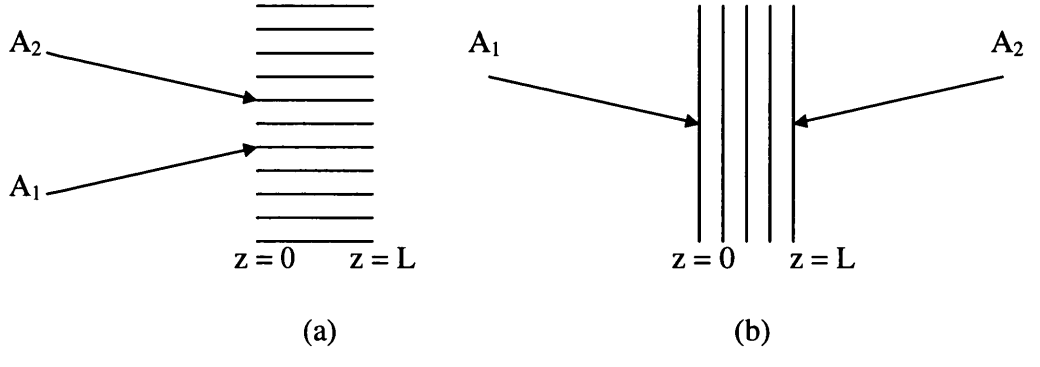

Fig. 3.1 Two wave mixing in photorefractive media. (a) Codirectional two-wave mixing and (b) contradirectional two-wave mixing.

3.1 Two-wave mixing

We consider the interaction of two laser beams inside a photorefractive medium (see Fig. 3.1). If the two beams are of the same frequency, a stationary interference pattern is formed. Let the electric field of the two waves be written

$$E_j = A_j e^{i(\omega t - \vec{k}_j \cdot \vec{r})}, \qquad j = 1,2 \tag{3.1}$$

Where A_1, A_2 are the wave amplitudes, ω is the angular frequency, and $\vec{k}_1$, $\vec{k}_2$ are the wave vectors. According to the model described in the chapter 2, the intersection of these two beams induces a volume index grating via the photorefractive effect. In general, the index grating has a spatial phase shift relative to the interference pattern. The index of refraction including the fundamental component of the intensity-induced gratings can be written [1]

$$n = n_0 + \frac{n_1}{2} e^{i\phi} \frac{A_1^* A_2}{I_0} \exp(-i\vec{K} \cdot \vec{r}) + c.c. \tag{3.2}$$

Where $I_0 = I_1 + I_2 \equiv |A_1|^2 + |A_2|^2$ and n_0 is the index of refraction when no light is present, ϕ is real and n_1 is a real and positive number. For the sake of simplicity, we assume a scalar grating. The phase ϕ indicates the degree to which the index grating is shifted spatially with respect to the light interference pattern. In photorefractive media that operate by diffusion only (i.e., no external static field), the magnitude of ϕ is $\pi/2$

with its sign depending on the direction of the c axis. $\vec{K}$ is the grating wave vector and I_0 is the sum of the intensities. The parameter n_1 depends on the grating spacing and its direction, as well as on the applied electric field and the material properties of the crystal, e.g., electro-optic coefficient, according to (2.9) and (2.12).

The finite spatial phase shift between the interference pattern and the induced volume index grating has been known for some time. The presence of such a phase shift allows the possibility of nonreciprocal steady-state transfer of energy between the beams [1]. To investigate the coupling, we substitute (3.2) for the index of refraction and $E = E_1 + E_2$ for the electric field into the wave equation.

We assume that both waves propagate in the xy plane. Generally speaking, if the beams are of finite extent (i.e., comparable to the intersection of the beams), the amplitudes may depend on both x and z. Here we assume, for the sake of simplicity, that the transverse dimensions of the beams are of infinite extent so that the boundary condition requires that the wave amplitudes A_1 and A_2 be functions of z only (see Fig. 3.1). We will solve for the steady state so that A_1 and A_2 are also taken to be time-independent.

Using the slowly-varying amplitude approximation, i.e., $\left|(d^2/dz^2)A_j\right| << \left|\beta_j (d/dz) A_j\right|$, $j = 1, 2$ and assuming a codirectional coupling with

$$\beta_1 = \beta_2 = k\cos\theta = \frac{2\pi}{\lambda} n_0 \cos\theta \tag{3.3}$$

Where 2θ is the angle between the beams inside the medium, and n_0 is the index of refraction of the medium, we obtain

$$\frac{d}{dz}A_1 = -\frac{1}{2I_0}\Gamma|A_2|^2 A_1 - \frac{\alpha}{2}A_1 \tag{3.4}$$

$$\frac{d}{dz}A_2 = \frac{1}{2I_0}\Gamma^*|A_1|^2 A_2 - \frac{\alpha}{2}A_2 \tag{3.5}$$

Where we have added terms that account for attenuation and α is the absorption coefficient, and Γ is the complex coupling gain coefficient

$$\Gamma = i\frac{2\pi n_1}{\lambda\cos\theta}e^{-i\phi} \equiv \gamma + i\Gamma_I \tag{3.6}$$

The parameters γ and Γ_I, can be written

$$\gamma = \frac{2\pi n_1}{\lambda\cos\phi}\sin\phi \qquad \text{and,} \qquad \Gamma_I = \frac{4\pi n_1}{\lambda\cos\theta}\cos\phi\,. \tag{3.7}$$

The solutions for the intensities $I_1(z)$ and $I_2(z)$ are [1]

$$I_1(z) = I_1(0)\frac{1+m^{-1}}{1+m^{-1}e^{\gamma z}}e^{-\alpha z} \tag{3.8}$$

$$I_2(z) = I_2(0)\frac{1+m}{1+me^{-\gamma z}}e^{-\alpha z} \tag{3.9}$$

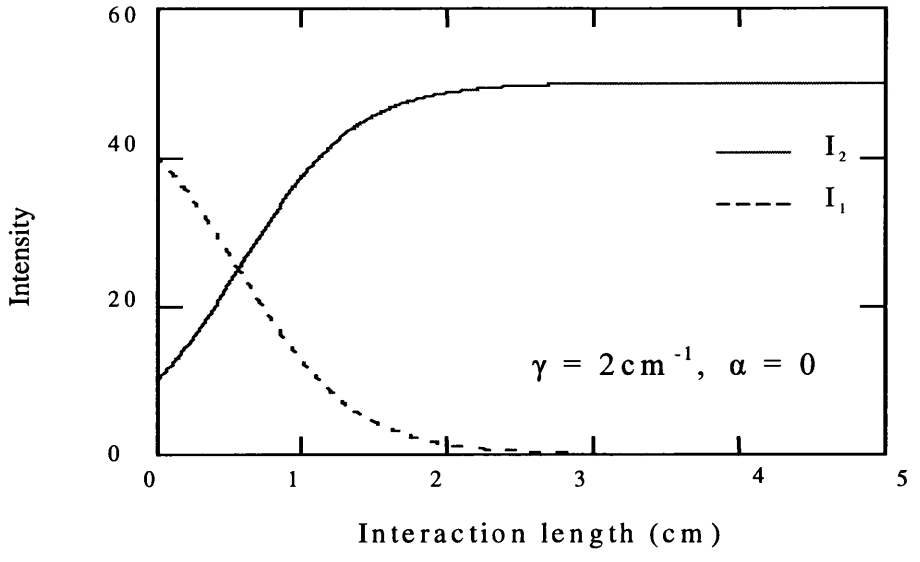

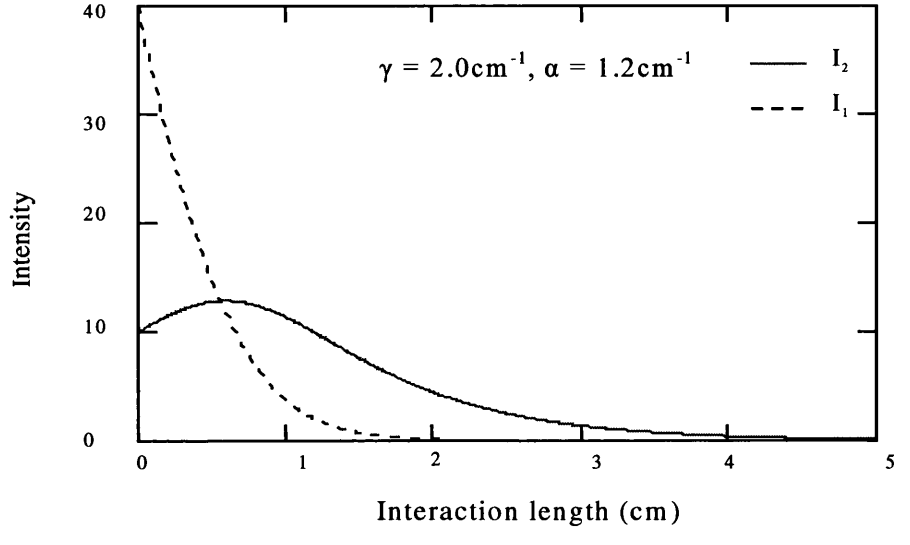

Fig. 3.2 Intensities I_1 and I_2 as functions of interaction length z

where m is the input intensity ratio $m = I_1(0)/I_2(0)$. Figure 3.2 plots the intensities as functions of interaction length z. The input intensities are I_1 (0) = 40, I_2 (0) = 10 respectively. Note that in the absence of absorption (α = 0), as in the top of Fig. 3.2, $I_2(z)$ is an increasing function of z and I_1 (z) is a decreasing function of z, provided γ is positive. The sign of γ depends on the direction of the c axis. As the result of the coupling for $\gamma > 0$ (γ = 2, in Fig. 3.2), Beam 2 gains energy from Beam 1. If this two-wave-mixing gain is large enough to overcome the absorption loss, then Beam 2 is amplified. If we refer to A_2 as the signal beam, then a useful parameter is the gain

$$g = \frac{I_2(L)}{I_2(0)} = \frac{1+m}{1+me^{-\gamma L}} e^{-\alpha L} \tag{3.10}$$

For example, in the bottom of Fig. 3.2, if the interaction length L = 0.5 cm (the thickness of our Ce:KNSBN crystal), γ = 2 cm^{-1}, α = 1.2 cm^{-1}, the gain g = 1.279. However, in the same condition, if the interaction L = 2 cm, the gain g = 0.442, which is less than 1. Usually we like to use the effective gain G, which is defined as

$$G = \frac{I_{out}(with - pump - beam)}{I_{out}(without - pump - beam)} \tag{3.11}$$

where I_{out} is the output signal beam intensity.

3.2 Time evolution of grating formation

The refractive index grating formation is a dynamic process involving a nonlinear interaction between the optical fields and the equations that describe the behavior of photoexcited mobile charge carriers in the host material. When the optical beams first traverse the crystal they encounter only a spatially constant refractive index. Migration of the photoexcited charge causes the formation of a refractive index grating whose maxima generally do not coincide with the position of the optical interference pattern maxima. As this occurs, light from one beam is diffracted into the propagation direction of the other beam. This in turn modifies the interference pattern modulation depth, which results in further modification of the refractive index spatial profile. This process is termed self-diffraction. Equilibrium is reached on a time scale that depends on host material parameter values and the optical intensity of the two interfering optical beams.

The amplitude of the space-charge field of the steady-state solution, Equation (2.9), can be written as the real (A) and the imaginary (B) components [2-3]

$$A \equiv \mathrm{Re}(E_1) = \frac{-E_0}{(1+E_d/E_q)^2 + (E_0/E_q)^2} \tag{3.12}$$

$$B \equiv \mathrm{Im}(E_1) = \frac{E_d\left(1+E_d/E_q + E_0^2/E_d E_q\right)}{(1+E_d/E_q)^2 + (E_0/E_q)^2} \tag{3.13}$$

where E_0 is the applied electric field, $E_d = Kk_BT/q$ is the diffusion field and $E_q = qN_A/\varepsilon\varepsilon_0 K$ is the maximum sustainable space-charge field ($K = 4\pi\frac{n}{\lambda}\sin\theta$ is the amplitude of the grating vector).

The theoretical time evolution of the grating formation was calculated by Kukhtarev [2, 3]. His solution was for the first Fourier harmonic of the grating, accurate for low modulation depths. For convenience, we summarize his results with a notation consistent with our equations. The expression for time evolution of the real and the imaginary components of the space-charge field is

$$a(t) \equiv \mathrm{Re}\left[E_0^{sc}(t)\right] = A - \exp(-t/\tau)(B\sin\omega t + A\cos\omega t) \tag{3.14}$$

$$b(t) \equiv \mathrm{Im}\left[E_0^{sc}(t)\right] = B + \exp(-t/\tau)(A\sin\omega t - B\cos\omega t) \tag{3.15}$$

In the limit as time goes to infinity, Eqs. (3.14) and (3.15) reduce to the saturation values A and B given by Eqs. (3.12) and (3.13), respectively. The photorefractive response time τ and the oscillation frequency ω are

$$\tau = \frac{\varepsilon\varepsilon_0}{\mu\tau_R\sigma_s N_D I_0 q} \times \frac{\left[1+\mu\tau_R\left(k_BTK^2/q\right)\right]^2 + \left(\mu\tau_R KE_0\right)^2}{\left(1+k_BTK^2\varepsilon\varepsilon_0/q^2N_A\right)\left[1+\mu\tau_R\left(k_BTK^2/q\right)\right] + \left(\mu\tau_R KE_0\right)^2\left(\varepsilon\varepsilon_0/\mu\tau_R N_A q\right)} \tag{3.16}$$

$$\omega = \frac{\mu\tau_R \sigma_s N_D I_0 q}{\varepsilon\varepsilon_0} \frac{\mu\tau_R KE_0 (\varepsilon\varepsilon_0 / \mu\tau_R N_A q - 1)}{\left[1 + \mu\tau_R (k_B TK^2 / q)\right]^2 + (\mu\tau_R KE_0)^2} \tag{3.17}$$

where $\varepsilon\varepsilon_0$ is the dielectric constant, q is the electronic charge, N_A (N_D) is the density of acceptor (donor) sites, k_B is Boltzmann's constant, T is the temperature, σ_s is the photoionization cross section, I_0 is the sum of write-beam intensities I_1 and I_2, and μ and τ_R are the carrier mobility and recombination time constant, respectively. The time evolution of the index modulation amplitude during writing is given by

$$n_1(t) = \frac{r_{eff}\varsigma}{2n} m' E_q \left[\frac{E_0^2 + E_d^2}{E_0^2 + (E_d + E_q)^2}\right]^{1/2} \times [1 - 2\exp(-t/\tau)\cos\omega t + \exp(-2t/\tau)]^{1/2} \tag{3.18}$$

where r_{eff} is the effective electro-optic coefficient, ς is the hole-electron competition factor, $m' = 2(I_1 I_2)^{1/2} / (I_1 + I_2)$ is the beam modulation. During incoherent erasure, $n_1(t - t_0)$ decays exponentially with time constant τ from its initial value at $t = t_0$. At zero applied field ω is zero, and the writing and the erasing evolve exponentially with the same time constant τ.

3.3 Basic parameters of the Ce:KNSBN crystal

Some parameters, such as coupling gain coefficient, absorption coefficient, determine the characterization of the two-wave mixing. In this section we will discuss the method for

measuring the basic parameters (coupling gain coefficient Γ, absorption coefficient α, and saturation intensity I_s) and give the experimental results.

3.3.1 Method of parameter measurement

First we introduce another important parameter, the saturation intensity I_s, which is defined as

$$I_s = \beta_T / s \tag{3.19}$$

Where β_T is the thermal emission rate, and s is the photoionization constant, which is proportional to the photoionization cross section σ_s

$$s = \sigma_s / h\nu \tag{3.20}$$

Then, for two-wave mixing in a photorefractive crystal, let the ratio χ be

$$\chi = I_s / I \tag{3.21}$$

where I is the total intensity in a crystal, the ratio χ determines the two-wave mixing stage.

When $\chi \geq 1$, two-wave mixing is at the intermediate stage (before saturation). The influence of I_s on two-wave mixing needs to be considered and the intensity property of two-wave mixing is characterized by the effective coupling gain coefficient Γ_{eff}

$$\Gamma_{eff} = \Gamma / (1 + I_s / I) \tag{3.22}$$

where Γ is the coupling coefficient, Γ_{eff} is intensity-dependent.

When $\chi << 1$, two-wave mixing is at the saturation stage. The contribution of I_s need not to be considered

$$\Gamma_{eff} = \Gamma \tag{3.23}$$

Γ_{eff} is intensity-independent at this stage.

At the saturation stage, the coupling gain coefficient Γ is obtained by first measuring the effective gain G, then calculating from following formula

$$G = \frac{1+m}{1+me^{-\Gamma L}}, \tag{3.24}$$

where L and m are the interaction length and the ratio of the incident pump to signal beam intensity, respectively. This conventional method was commonly used in many papers [4] – [6], but can not be used to determine I_s by replacing Γ with $\Gamma / (1 + I_s / I_0)$ in Eq.(3.22), where I_0 is total incident intensity, because Eq.(3.22) remains effective only for $I_s / I_0 << 1$. In other words, Eq.(3.22) is only suitable for the case that two-wave

mixing is in the saturation stage. Therefore, the conventional method becomes invalid when the contribution of I_s needs to be considered.

When the contribution of saturation intensity (I_s) is considered, the intensity-dependent two-wave mixing coupled-wave equation can be written as [7]

$$\frac{dI_1}{dz} = -\frac{\Gamma}{I + I_s} I_1 I_2 - \alpha I_1, \tag{3.25}$$

$$\frac{dI_2}{dz} = \frac{\Gamma}{I + I_s} I_1 I_2 - \alpha I_2 \tag{3.26}$$

where indexes 1 and 2 express pump and signal beam, respectively, and $I = I_1 + I_2$ is the total intensity of the interacting beams in a crystal. Note I is a function of z. From Eq. (3.25) and (3.26) one can derive

$$I(z) = I_0 \exp(-\alpha z) \tag{3.27}$$

where $I_0 = I_1(0) + I_2(0)$. Setting Eq. (3.27) into Eqs. (3.25) and (3.26), we can obtain the solution for the output signal intensity $I_2(L)$ as following

$$I_2(L) = \frac{I_0(1+m)\exp(-\alpha L)}{1 + m\delta^{\Gamma/\alpha}} \tag{3.28}$$

$$\delta = \frac{\exp(-\alpha L) + I_s / I_0}{1 + I_s / I_0} \tag{3.29}$$

According to the definition of effective gain G, from Eq. (3.28) and (3.29), G can be written as

$$G = \frac{1+m}{1+m\delta^{\Gamma/\alpha}} \tag{3.30}$$

If $I_s/I_0 << 1$, I_s/I_0 can be neglected in Eq.(3.29), and then $I_2(L)$ and G degenerate to the form of the saturation stage. Otherwise it is better to measure the coefficients Γ, I_s and α simultaneously.

Let $Y = I_0/I_2(L)$, $b = exp(\alpha L)$, and $k = \delta^{\Gamma/\alpha}$. From Eq. (3.28) and (3.29), we obtain a linear equation of Y as the function of m

$$Y = b + km \tag{3.31}$$

Obviously, b is the intercept and k is the slope of the straight line. If the straight line is determined, the values of α and $\delta^{\Gamma/\alpha}$ can be obtained. In order to determine Γ and I_s, we need take I_0 under two different values, denoted by I_{01} and I_{02}, to determine the straight line because there are two unknown variables, Γ and I_s in the term of $\delta^{\Gamma/\alpha}$. However, α is dependent on the total intensity as well. Let α_1 and α_2 denote the absorption coefficients corresponding to I_{01} and I_{02}, respectively. Thus we obtain two straight lines as

$$Y = b_j + k_j m, \qquad j = 1, 2 \tag{3.32}$$

where $b_j = \exp(\alpha_j L)$, $k_j = \delta^{\Gamma/\alpha_j} \exp(\alpha_j L)$ and

$$\delta_j = \left[\exp(-\alpha_j L) + I_s / I_{0j}\right]/(1 + I_s / I_{0j}), \qquad j = 1,2 \tag{3.33}$$

Let $\varsigma = \ln b_2 \ln(k_2 / b_2)/[\ln b_1 \ln(k_1 / b_1)]$, we derive α_1, α_2, I_s and Γ as

$$\alpha_j = \frac{\ln(b_j)}{d}, \quad j = 1,2 \tag{3.34}$$

$$I_s = I_{02} \frac{(I_{01}/b_1 + I_s)^{\varsigma} - (I_{01} + I_s)^{\varsigma}/b_2}{(I_{01} + I_s)^{\varsigma} - (I_{01}/b_1 + I_s)^{\varsigma}} \tag{3.35}$$

$$\Gamma = \left[\ln(k_1 / b_1) \ln b_1\right] / \left[d \ln\left(\frac{I_{01}/b_1 + I_s}{I_{01} + I_s} \right) \right] \tag{3.36}$$

Equation (3.35) should be solved numerically.

3.2.2 Experiment and results

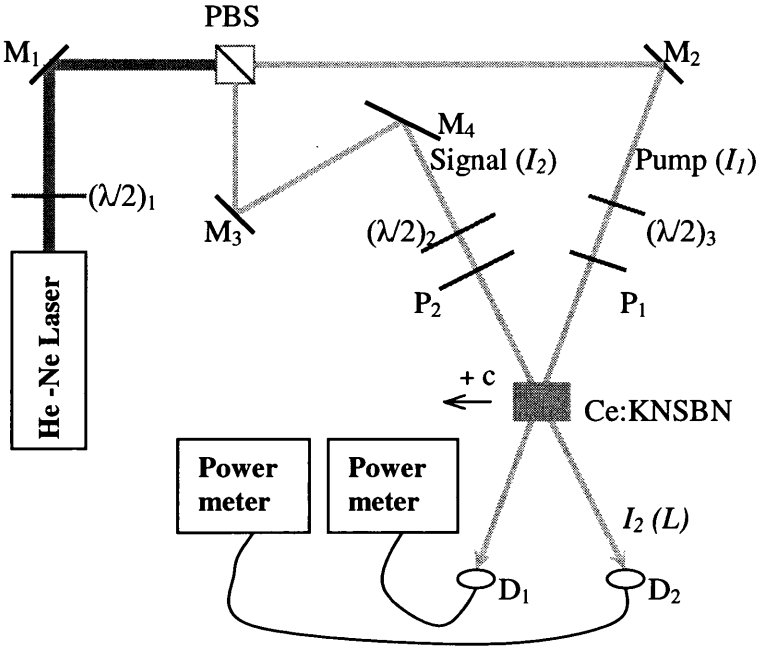

Fig. 3.3 Two-wave mixing set-up for measuring the parameters of Ce:KNSBN. $(\lambda/2)_i$ are half-wave-plates; M_i are reflective mirrors; P_i are polarizers; PBS is a polarise-beam-splitter; and D_i are detectors.

We used the two-wave mixing configuration shown in Figure 3.3 to simultaneously measure the three parameters of the Ce:KNSBN mentioned above, i.e. the coupling gain coefficient Γ, the absorption coefficient α, and the saturation intensity I_s. The c axis of Ce:KNSBN was oriented to be in the incident plane and perpendicular to the bisector of the two incident beams. The beam (λ = 632.8 nm) from the 40 mW He-Ne laser was

divided into two as the pump and the signal beams, both of them were extraordinary polarized in the plane of the paper. The angle between two beams was about 8.7°. The beam from the He-Ne laser was slightly divergent, the diameter of the incident beams on the crystal was more than 5 mm. A 3×3 mm^2 iris was placed in front of the photoelectric detector to minimize the influence of scattered light, and to confirm that the detected intensity was the transmitted portion that had totally interacted with the other beam in the crystal.

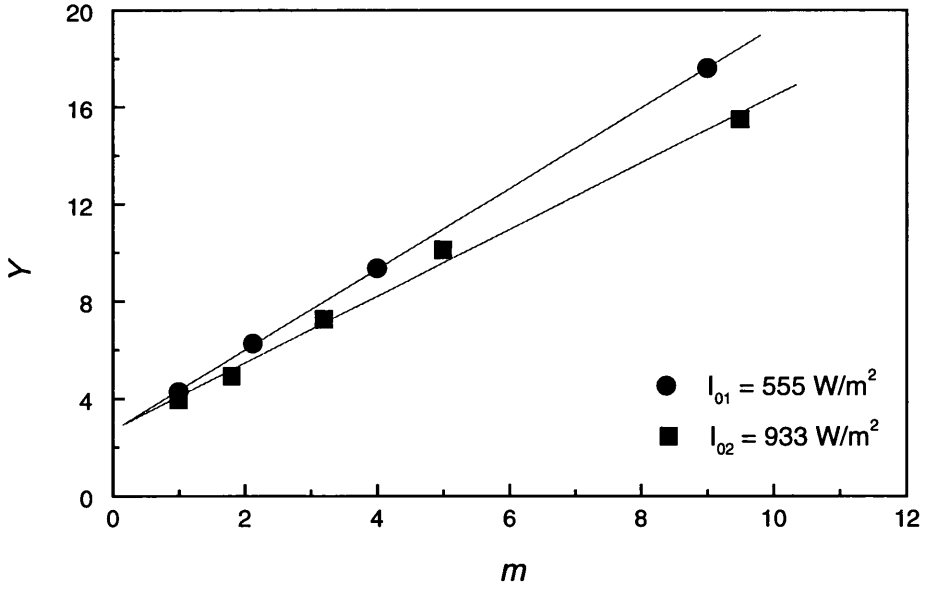

Fig. 3.4 Measured ratio Y of total incident intensity I_0 to the output signal I_2 (L) as function of the incident intensity ratio $m = I_1(0) / I_2(0)$. The lines in the graph were linear fits of the data.

Fig. 3.4 shows the ratio Y of total incident intensity I_0 to the output signal intensity $I_2(L)$ as the function of the incident intensities ratio $m = I_1(0)/I_2(0)$ under two different total incident intensity $I_{01} = 555$ W/m^2, $I_{02} = 933$ W/m^2 respectively. The linear fits of the data gave the value of b_1, b_2, k_1 and k_2. From equations (3.34) – (3.36), we calculated the measured parameters of Ce:KNSBN as

1) the absorption coefficient α,

   $\alpha_1 = 1.96$ cm^{-1}, related to incident intensity $I_{01} = 555$ W/m^2,

   $\alpha_2 = 2.00$ cm^{-1}, related to incident intensity $I_{02} = 933$ W/m^2;

2) the saturation intensity $I_s = 957$ W/m^2;

3) the coupling coefficient $\Gamma = 2.14$ cm^{-1}.

It should be noted that all values of intensities in the equations of this section are the ones inside the crystal, however, the measured intensities are the ones in air. The reflectivity R of the crystal face needs to be considered. We measured the reflectivity of the crystal as $R = 0.22$. In the calculations, the two incident intensities we used were $I_{01} = 0.78\times555$ W/m^2, $I_{01} = 0.78\times933$ W/m^2 respectively. The calculated value from equations (3.34) – (3.36), in fact, is an average of the measured data under different values of pump-to-signal ratio m. We have pointed out that the coupling gain coefficient measured by the conventional method has errors when the contribution of the saturation intensity can not be neglected, such as in the problems of the intensity or temperature dependence of two-wave mixing. These can be avoided by using the method we chose.

In order to check the parameters we got, we measured the effective gain G as a function of total incident intensity I_0 (the incident intensity inside the crystal, i.e., the reflectivity of the crystal is considered), with m = 1.5. The solid curve was the calculated result using Eq. (3.30), with L = 0.5014 cm, m = 1.5, α = 2.0 cm^{-1}, Γ= 2.14 cm^{-1} and I_s = 957 W/m^2. L is the interaction length, in our experiment, $L = d/\cos\theta$, where d is the thickness of the crystal, and θ is the half angle between two incident beams. The calculated curve is in agreement with the experimental data. The deviations were mainly due to the fluctuation of output power from the He-Ne laser, and may result from the fact that the intensity-dependence of α is not considered in Eq. (3.30).

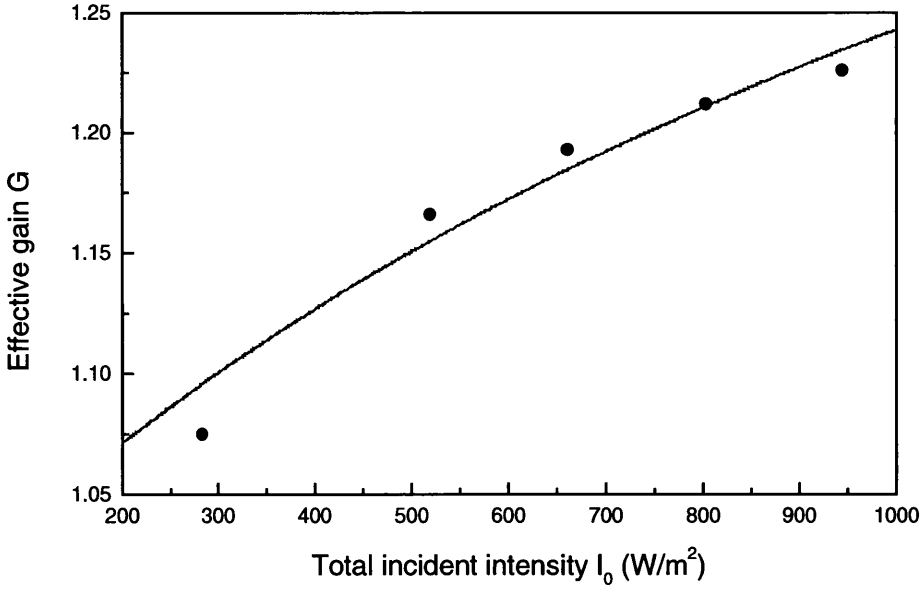

Fig. 3.5 Effective gain G as a function of total incident intensity I_0 (into the crystal). Solid curve was the calculated results using Eq. (3.23), with L = 0.5014 cm, m = 1.5, α = 2.0 cm^{-1}, Γ= 2.14 cm^{-1} and I_s = 1046 W/m^2

3.4 Properties of the Ce:KNSBN crystal

The mechanism by which light induces a change in the refractive index of crystal is the photorefractive effect, in which charges in the crystal migrate in the presence of light regions of higher optical intensity to regions of lower optical intensity. The resulting charge-density pattern creates an electrostatic field, which alters the refractive index of the materials by means of the linear electro-optic (Pockels) effect. The magnitude of this light-induced refractive-index change, and hence its scattering efficiency, depends on the Pockels coefficients of the crystal, the angle of the optical beams with the crystal *c* axis, and on the number density of charge carriers participating in light-induced charge migration. In this section we will discuss more Pockels coefficients of the Ce:KNSBN by using the two-wave mixing method.

3.4.1 Coupling gain coefficient

In last section the coupling gain coefficient we got is only an average of the measured data under different values of pump-to-signal ratio *m*. Actually the gain coefficient is also dependent on the amplitude of the grating vector, or the cross angle between two incident beams. Investigating its dependence on the grating wavelength, we can derive some Pockels coefficients, such as the effective photorefractive charge density N_{eff} and the hole-electron competition factor ζ.

The measured coupling gain coefficient Γ can be defined as [8]

$$\Gamma = \frac{1}{L}\ln\left(\frac{I_s' I_p'}{I_p I_s}\right) \tag{3.37}$$

where $I_s'(I_s)$, $I_p'(I_p)$ are the transmitted intensity of the signal and the pump beams with (without) coupling, L is the interaction length.

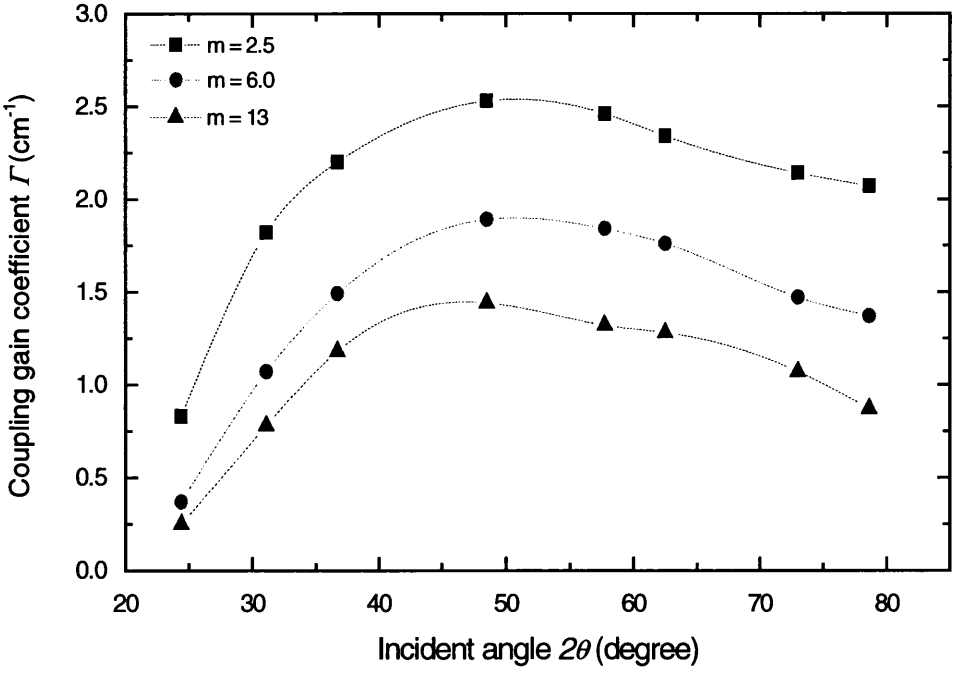

Fig. 3. 6 Two-wave coupling results of Ce:KNSBN crystal. λ = 514 nm. The dash lines joining the points are merely to guide the eye.

Figure 3.6 shows the experimental results of the two-wave mixing coupling gain coefficient Γ of the Ce:KNSBN crystal as a function of the incident angle for different pump-to-signal ratio m. We find that the measured data of coupling gain coefficient is dependent on the pump-to-signal ratio, the larger the m is, the smaller the value of Γ we could get, and the maximum values of Γ for different m are all corresponding to the incident angle of $2\theta \approx 50°$. We will discuss this phenomenon again after comparing the calculated results in section 3.5.1.

The effective photorefractive charge density N_{eff} and the hole-electron competition factor ζ can be found from the measurement of Γ as a function of the grating wavelength Λg by the procedure described in the reports on investigating the properties of Ce-doped SBN [9, 10]. There exists an expression for Γ with no applied field:

$$\frac{\lambda}{\Gamma \Lambda_g} = \frac{n\varepsilon\varepsilon_0}{q r_{eff} \zeta N_{eff}} \left(\frac{\lambda}{\Lambda_g} \right)^2 + \frac{\lambda^2 n q}{4\pi^2 r_{eff} \zeta k_B T} \tag{3.38}$$

where λ is the wavelength in vacuum, n is the index of refraction, $N_{eff} = N_A(1 - N_A / N_D)$, and r_{eff} is the effective electro-optic coefficient. For crystals of point 4mm group, such as SBN and KNSBN, r_{eff} can be represented by the following expressions:

$$r_{eff} = n_o^4 r_{13} \cos\beta \tag{3.39}$$

for ordinarily polarized light, and

$$r_{eff} = \frac{1}{2}\left[n_o^4 r_{13}(\cos 2\theta - \cos 2\beta) + 4n_o^2 n_e^2 r_{42} \sin^2 \beta + n_e^4 r_{33}(\cos 2\theta + \cos 2\beta)\right] \quad (3.40)$$

for extraordinarily polarized light.

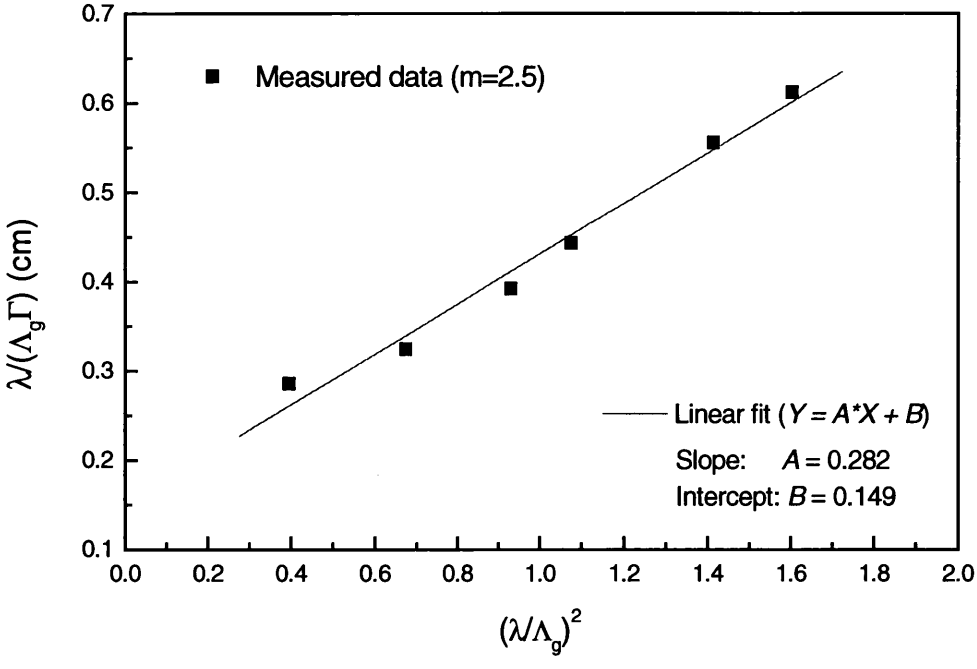

Fig. 3.7 Measured coupling gain coefficients Γ (m = 2.5, as in Fig. 3.6) as a function of the grating wavelength Λ_g, which is plotted in the form of $\lambda/(\Lambda_g\Gamma) \sim (\lambda/\Lambda_g)^2$. The line in the graph is the linear fitting of the data, the fitted parameters are $A = \dfrac{n\varepsilon\varepsilon_0}{q r_{eff} \zeta N_{eff}}$ and $B = \dfrac{\lambda^2 nq}{4\pi^2 r_{eff} \zeta k_B T}$

Figure 3.7 is a plot of $\lambda/(\Lambda_g \Gamma)$ versus $(\lambda/\Lambda_g)^2$ for the measured coupling gain coefficient Γ of the pump-to-signal ratio m = 2.5 (shown in Fig. 3.6) with the extraordinarily polarized incident beam. The intercept and slope of the linear fit are A = 0.149 cm and B = 0.282, respectively. From Eq. (3.38) we have $A = \frac{n\varepsilon\varepsilon_0}{q r_{eff} \zeta N_{eff}}$ and $B = \frac{\lambda^2 n q}{4\pi^2 r_{eff} \zeta k_B T}$. Using the typical parameters of KNSBN crystal [11], $\varepsilon_{11} = 588, \varepsilon_{33} = 500$, $n_o = 2.27, n_e = 2.30$, we got the product of the effective electro-optic coefficient and the hole-electron competition rate $r_{eff}\zeta$ = 403×10^{-12} m/V, and the effective photofractive charge density N_{eff} = 8.5×10^{16} cm^{-3}, respectively.

3.4.2 Response rate of the crystal

The response time (τ) is defined as the time for the transmissive signal beam intensity to reach (1 - 1/e) of its steady state value. The response rate (τ^{-1}) is the inverse of the response time. If no external electric field is applied to the crystal and if the grating constant is much larger than the diffusion length of the dominant charge carrier (L_d), the photorefractive response rate can be written as [12]

$$\tau^{-1} \approx \frac{1}{\varepsilon\varepsilon_0}(\sigma_d + \sigma_{ph}) = \frac{1}{\varepsilon\varepsilon_0}\left(\sigma_d + \frac{q\lambda\alpha\mu\tau_R I_0}{hc}\right) \tag{3.41}$$

where σ_d and σ_{ph} are the dark conductivity and photoconductivity, respectively, h is Planck's constant, and c is the speed of light. The diffusion length L_d is estimated by

$$L_d = \sqrt{\frac{\mu \tau_R k_B T}{q}} \tag{3.42}$$

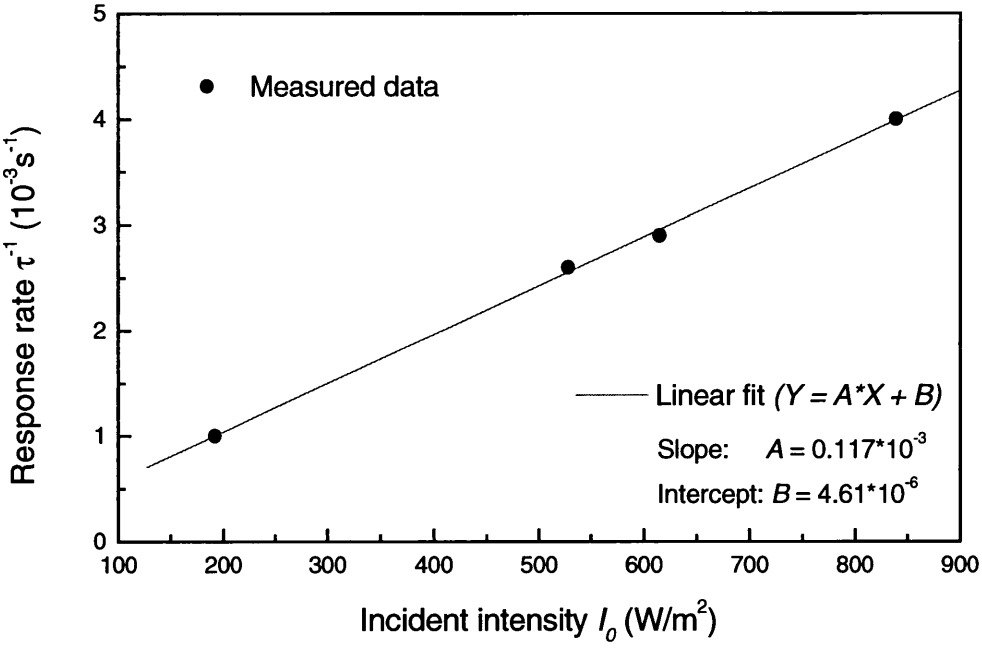

Fig. 3.8 Dependence of two-wave coupling response rate on the incident beam intensity of Ce:KNSBN. The incident angles are $2\theta = 8.7°$, the pump-to-signal ratio m ~1, and λ = 632.8 nm. The line in the graph is the linear fitting of the measured data, the fitted parameters are $A = \frac{q\lambda\alpha\mu\tau_R I_0}{\varepsilon\varepsilon_0 hc}$ and $B = \frac{\sigma_d}{\varepsilon\varepsilon_0}$

Figure 3.8 shows the experimental results of the response rate as a function of the total incident intensity, where the incident angle is $2\theta = 8.7°$, the pump-to-signal ratio m ~ 1,

and λ = 632.8 nm. The slope and the intercept of the linear fit of the data are A = 0.117×10^{-3} s and B = 4.61×10^{-6} $m^2W^{-1}s^{-1}$, respectively. According to Eq. (3.41), we got that the product of the carrier mobility and the recombination time constant $\mu\tau_R$ = 3.1×10^{-12} cm^2/V, and the dark conductivity σ_d = 0.8×10^{-10} $(\Omega cm)^{-1}$, respectively. From Eq. (3.42) we calculated the diffusion length L_d = 2.8 nm.

3.5 Calculated results

Using the parameters we have measured, we can investigate more properties of the photorefractive crystal by theoretical calculation. In this section we will show the coupling gain coefficient and the space-charge field of Ce:KNSBN as the function of incident beam angle in the two-wave mixing coupling.

3.5.1 Coupling gain coefficient

According to Ducharme and Feinberg [13], the relation between the two-wave mixing coupling gain coefficient Γ and the incident beam angle can be described as below:

$$\Gamma = \frac{A\sin\theta}{1+B^{-2}\sin^2\theta}\frac{\cos 2\theta_i}{\cos\theta_i} \tag{3.43}$$

where $\theta(\theta_i)$ is the external (internal) half-angle between the two incident beams ($sin\theta = nsin\theta_i$, n is the index of refraction of the crystal) and the two parameters A and B are given by

$$A = r_{eff}\zeta \frac{8\pi^2 n^3 k_B T}{q\lambda^2} \tag{3.44}$$

$$B = \frac{q\lambda}{4\pi}\sqrt{\frac{N_{eff}}{\varepsilon\varepsilon k_B T_0}} \tag{3.45}$$

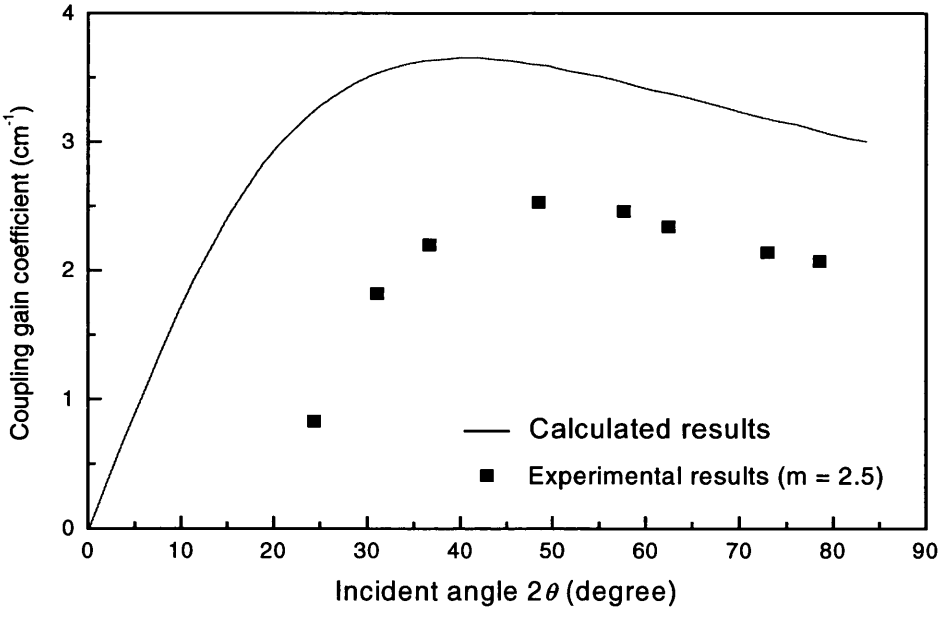

Fig. 3.9 Coupling gain coefficient Γ versus incident beams angle. The experimental results have the similar function relationship as the calculated ones, however, there is a difference in their absolute values.

Using the parameters of Ce:KNSBN we got, and the other typical ones of KNSBN crystal [11] — $r_{13} = 50\times10^{-12} m/V, r_{33} = 50\times10^{-12} m/V, r_{42} = 50\times10^{-12} m/V$, we calculated the coupling gain coefficient as the function of incident beams angle. Figure 3.9 shows the calculated results comparing with the experimental ones. We found that the maximum measured Γ is 2.5cm^{-1}, and the maximum calculated one is 3.6cm^{-1}. Although the experimental results have the similar function relationship as the calculated ones, there is a difference in their absolute values. All coupling gain coefficients from our experiment are about 1cm^{-1} smaller than those from the calculation, corresponding to the same incident beam angle. There are two possible explanations: 1) In the calculation, the quoted parameters might not be suitable for the specific crystal we used in our experiment. Due to different growing techniques, that similar crystals have different properties is well accepted in the field of photorefractive materials. 2) The difference is the result of strong fanning in the Ce:KNSBN crystal. Our theoretical analysis took no account of the fanning effect, however, the beam fanning did exist in all photorefractive crystals, especially for the thick sample as we used in the experiments.

3.5.2 Space-charge field

All the photorefractive phenomena displayed a dependence on the photoinduced space-charge electric field forming in the crystals. The amplitude of the steady-state space-charge electric field is related to the incident beams angle in two-wave mixing. As mentioned before, the diffusion field E_d and the maximum sustainable space-charge field

E_q are defined as $E_d = Kk_BT/q$ and $E_q = qN_{eff}/\varepsilon\varepsilon_0 K$, respectively, where $K = 4\pi\frac{n}{\lambda}\sin\theta$ is the amplitude of the grating vector. Fig. 3.10 shows the dependence of the diffusion field E_d and the maximum sustainable space-charge field E_q on the incident beam angle θ in Ce:KNSBN crystal. We can find that the diffusion field becomes greater while the incident angle θ increases. Since the grating spacing Λ_g is determined as $\Lambda_g = \lambda/(2n\sin\theta)$, the result we got can be explained as that the smaller is the grating spacing, the greater is the gradient of the electron distribution and the stronger are the forces of diffusion.

Figure 3.11 shows the space-charge field of Ce:KNSBN, in the case of pure diffusion with $E_0 = 0$, as a function of incident beam angle θ. According to Eq. (2.9), or Eqs. (3.12) and (3.13), when the applied electric field $E_0 = 0$, its real component is zero, the space-charge field is purely imaginary. The amplitude of the space-charge field is

$$E_1 = E_d/(1 + E_d/E_q). \tag{3.46}$$

From Eq. (3.46) there exists an optimum value of K, since E_d is proportional to K and E_q is inversely proportional to K. The optimum occurs when $E_d = E_d$. The optimum value of K is

$$K_{opt} = \sqrt{\frac{q^2 N_{eff}}{\varepsilon\varepsilon_0 k_B T}} \tag{3.47}$$

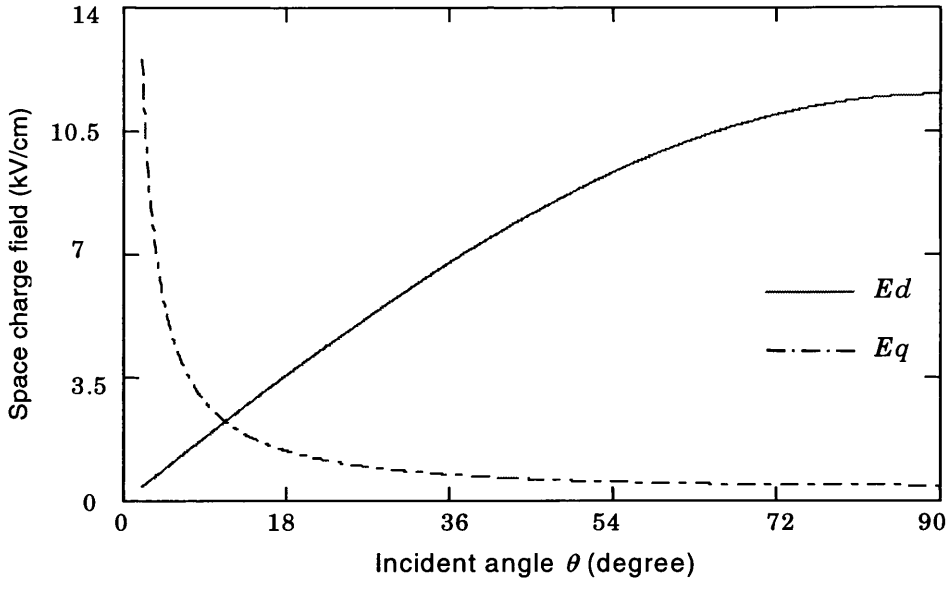

Fig. 3.10 The diffusion field E_d and the maximum sustainable space-charge field E_q of Ce:KNSBN as functions of incident beam angle θ.

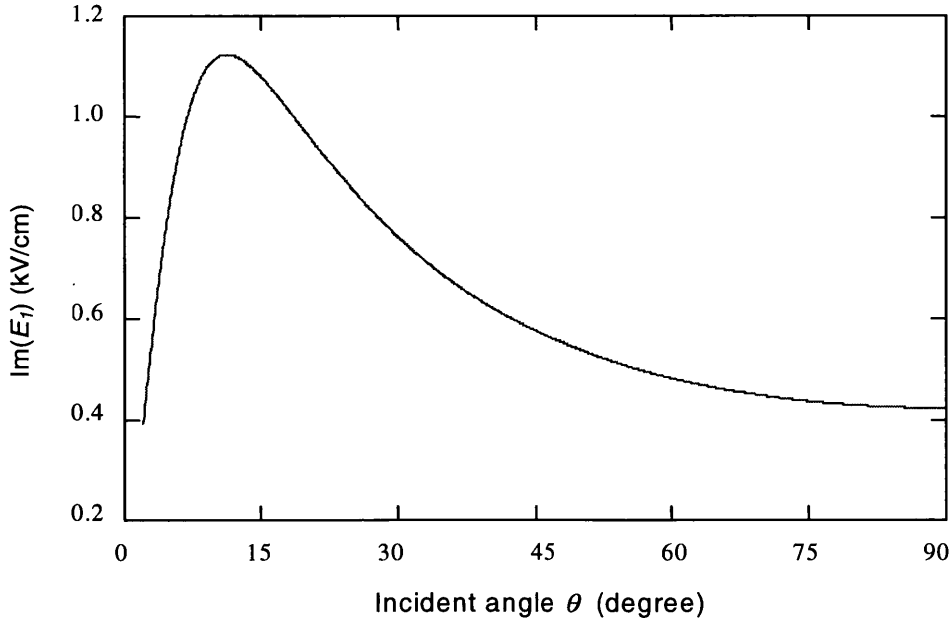

Fig. 3.11 The space-charge field of Ce:KNSBN, in the case of pure diffusion with E_0 = 0, as a function of incident beam angle θ.

The corresponding incident angle $(\theta)_{opt} \sim 11°$, as shown in Fig. 3.11, or the grating spacing $(\Lambda_g)_{opt} = 0.72$ μm. And the maximum space-charge field $(E_1)_{max} = 1.12$ kV/cm^{-1}.

3.6 Conclusions

Using the two-wave mixing method, we studied the photorefractive properties of Ce doped KNSBN material, and found most parameters of the new photrefractive Ce:KNSBN crystal, as listed in table 1.1. Especially, we investigated the coupling gain coefficient, which is one of the most important characteristics of photorefractive materials, by different ways — considering the two-wave mixing stage, normal measurement, and theoretical calculation, and found that fanning effect might limit the two-wave mixing coupling in the Ce:KNSBN crystal.

Table 1.2 gives some parameters of the photorefractive Cu-doped KNSBN crystal [8], its Cu-doping level 0.04wt% is the same as our Ce-doping level in the crystal, but its thickness is only 1.0 mm, and the thickness of our Ce:KNSBN is 5.0 mm. Comparing the properties of these two types of KNSBN crystal, we found most of their parameters were in the same orders. But the coupling gain coefficient of this Cu-doped KNSBN crystal was much greater than that of our Ce:KNSBN sample. The maximum Γ of our Ce:KNSBN crystal is 3.6 cm^{-1} (calculated result), which is 6 times less than Γ_{max} of the Cu:KNSBN. However, the product of carrier mobility and recombination time constant $\mu\tau_R$ for our Ce: KNSBN crystal was about 5 times greater than the product of $\mu\tau_R$ for the Cu:KNSBN.

Table 1.1 Parameters of the photorefractive Ce-doped KNSBN crystal

Parameter	Definition	Value	Comments
Γ	Coupling gain coefficient	2.14 cm^{-1}	Average for m, $\theta = 4.33°$
α	Intensity absorption	2.0 cm^{-1}	$I_0 = 933$ W/m^2, $\lambda = 632.8$ nm
I_s	Saturation intensity	957 W/m^2	$\lambda = 632.8$ nm
N_{eff}	Effective photorefractive charge density	8.52×10^{16} cm^{-3}	
$r_{eff}\zeta$	Product of effective electro-optic coefficient and hole-electron competition factor	403×10^{-12} m/V	
$\mu\tau_R$	Product of carrier mobility and recombination time constant	3.1×10^{-12} cm^2/V	
σ_d	Dark conductivity	0.8×10^{-10} $(\Omega cm)^{-1}$	
L_d	Diffusion length	2.8 nm	
$(E_1)_{max}$	Maximum space-charge electric field	1.12 kV/cm	Pure diffusion case, applied field $E_0 = 0$
$(\theta)_{opt}$	Optimum incident angle	11°	Pure diffusion case
$(\Lambda_g)_{opt}$	Optimum grating spacing	0.72 μm	Pure diffusion case

Table 1.2 Parameters of the photorefractive Cu-doped KNSBN crystal [8]

Parameter	**Definition**	**Value**	**Comments**
Γ	Coupling gain coefficient	22.14 cm^{-1}	Maximum value $\theta = 16.5°$
α	Intensity absorption	1.19 cm^{-1}	$\lambda = 514$ nm
N_{eff}	Effective photorefractive charge density	5.16×10^{16} cm^{-3}	
$r_{eff}\zeta$	Product of effective electro-optic coefficient and hole-electron competition factor	125×10^{-12} m/V	
$\mu\tau_R$	Product of carrier mobility and recombination time constant	0.63×10^{-12} cm^2/V	
σ_d	Dark conductivity	0.214×10^{-10} $(\Omega cm)^{-1}$	

In the end of this chapter, we demonstrate the typical signal output in the two-wave mixing experiment. The output of the signal beam through the Ce:KNSBN crystal at different time periods as shown in the figure 3.12:

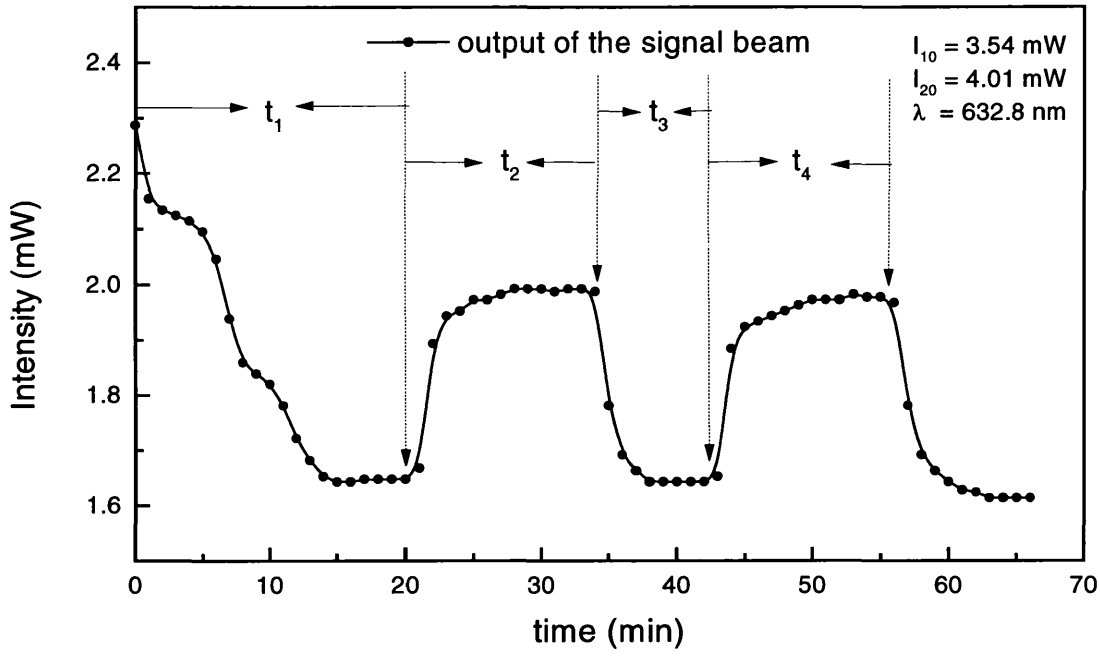

Fig. 3.12 The typical signal output in two-wave mixing experiment. t_1) only signal beam I_2 switched on; t_2) pump beam I_1 was on as well; t_3) pump beam I_1 was blocked, only signal beam I_2 was left; t_4) pump beam I_1 was on again.

1. Only signal beam I_2 switched on. Although the input of signal beam was I_{20} = 4.01mW, there was only some portion of the incident intensity to transmit through the crystal in the beginning, due to the reflecting and absorption effects. Then the self-pumped phase conjugated beam was building up (which was counter-

propagating against the incident beam) in the part of period t_1. The transmitting signal beam reached its first equilibrium state, its intensity is only a small portion of the incident intensity (~ 40 %, in our example).

2. Pump beam I_1 was on as well. In the beginning of this period t_2, there existed a dynamic process of the index grating formation, its time scale (writing time) depended on the crystal parameter values and the intensity of the two interfering incident beams. When the index grating was formed, i.e. the space-charge field in the crystal reached its steady-state, the two-wave mixing coupling caused energy transfer from the bump beam to the signal beam, the transmitting signal beam reached its second equilibrium state. It should be noted that the direction of energy transfer depends on the c axis direction of the photorefractive crystal.

3. Pump beam I_1 was blocked, only signal beam I_2 was left. Since the index grating was based on the spatial variation of the light intensity caused by two interfering incident beams, the signal beam would reach its equilibrium state in the crystal as in period t_1. During it reached the first equilibrium state, the signal beam erased the index grating formed in period t_2. In the case of pure diffusion with applied field $E_0 = 0$, the erasing time is the same as the writing time.

4. Pump beam I_1 was on again. It would repeat the processes in the period t_2.

Chapter 3: References:

1. P. Yeh, "Two-wave mixing in nonlinear media," IEEE J. Quantum Electron, vol. 25, pp. 484-519, 1989.
2. N. V. Kukhtarev, "Kinetics of hologram recording and erasure in electrooptic crystals", Sov. Tech. Phys. Lett., vol. 2, pp438-440, 1976
3. N. V. Kukhtarev, V. B. Markov, S. G. Odulov, M. S. Soskin and V. L. Vineskii, "Holographic storage in electrooptic crystals", Ferroelectrics, vol. 22, pp949-960, 1979
4. R. S. Rana, D. D. D. Nolte, R. Steldt and E. M. Monberg, J. Opt. Soc. Am. B, vol. 9, p1614, 1992
5. Paul H. Beckwith and William R. Christian, Opt. Lett., vol. 14, p642, 1989
6. Lijen Cheng and A. Partovi, Appl. Phys. Lett., vol. 49, p1456, 1986
7. M. Bass et al. *Handbook of Optic*, vol. II, 2nd ed. McGraw-Hill, New York, 1994
8. X. Shen, J. Zhao, X. Lu, Q. Jiang, J. Zhang, H, Xia, L. Song, S. Zhang, J. Han and H. Chen, "Photorefractive properties of Cu-doped KNSBN crystals with different doping levels and different dimensions", J. Appl. Phys., vol. 86, No. 6, pp3371-3376, 1999
9. G. L. Wood, W. W. Clark III, M. J. Miller, E. J. Sharp, G. J. Salamo and R. R. Neurgaonkar, "Broadband photorefractive properties and self-pumped phase conjugation in Ce-doped SBN:60", IEEE J. Quantum Electron. QE-23, pp2126-2134, 1987

10. J. E. Ford, J. Ma, Y. Fainman, S. H. Lee, Y. Taketomi, D. Bize, and R. R. Neurgaonkar, "Multiplex holography in strontium barium niobate with applied field", J. Opt. Am. A, vol. 9, No. 7, pp1183-1192, 1992

11. P. L. Ramazza and Mingjun Zhao, "Experimental study of two-wave mixing amplification in Cu-doped KNSBN", Opt. Comm., vol. 102, pp93-99, 1993

12. L. A. Boatner, E. Kratzig and R. Orlowski, Ferroelectrics, vol. 27, p247, 1980

13. S. Ducharme and J. Feinberg, J. Opt. Soc. Am. B, vol. 3, p383, 1986

Chapter 4 Diffraction efficiency

Holographic recording in thick media (volume grating) is of particular interest for high-capacity information storage and for the efficient white-light display of holograms. The high efficiency of light conversion which is attainable with thick dielectric gratings is also important for microimaging, and it could make it practical to use holographic optical components in a variety of optical systems. In many of the applications of photorefractive materials the aim is to write a dielectric grating. For example, an object wave containing some useful information, say a digital data page in which the information is encoded with black spots for 0's and white spots for 1's, this object wave may then be interfered in the photorefractive material with a plane reference wave to write a hologram. When the hologram is illuminated by the reference wave the object beam is reconstructed. The question is: what is the intensity of the object beam for a given reference beam intensity, or in other words what is the diffraction efficiency? In this case we need to know the diffraction efficiency for illumination by the same reference beam.

4.1 Bragg diffraction from volume gratings

We have mentioned that when two beams of coherent electromagnetic radiation intersect inside a photorefractive medium, the periodic variation of the intensity due to interference will induce a volume index grating. The grating wave vector is given by

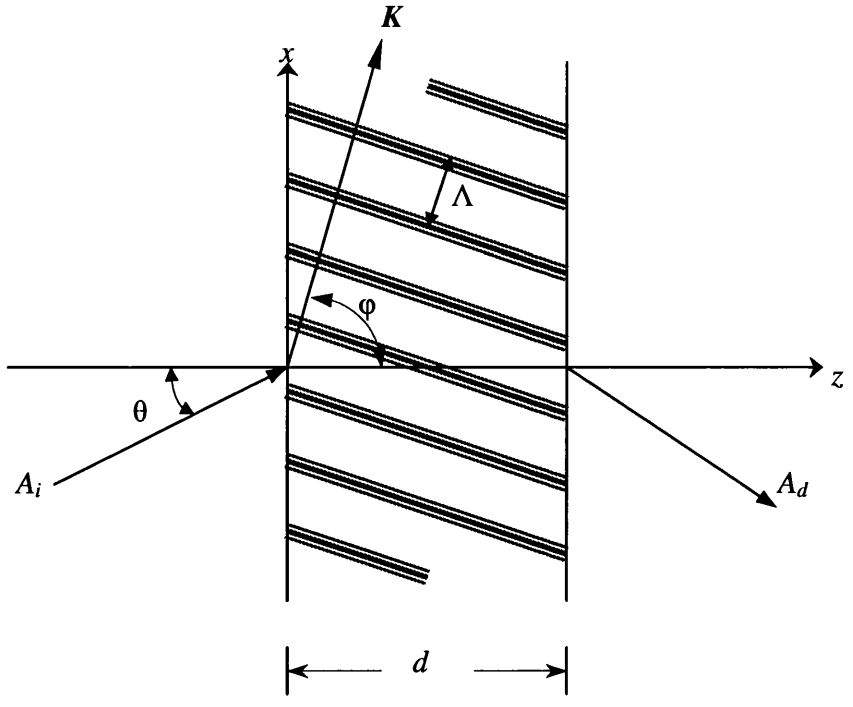

Fig. 4.1 Volume grating with slanted fringes. The grating parameters are: θ — angle of incidence in the medium, ***K*** — grating vector (perpendicular to the fringe plane), Λ — grating period, φ — slant angle, and d — grating thickness.

$\vec{K} = \pm(\vec{k}_2 - \vec{k}_1)$, where $\vec{k}_1$ and $\vec{k}_2$ are wavevectors of the beams. Fig. 4.1 shows a volume grating which is used in our analysis. The z axis is chosen perpendicular to the surfaces of the medium, the x axis in the plane of incidence and parallel to the medium boundaries and the y axis perpendicular to the paper. The fringe planes are oriented perpendicular to the plane of incidence and slanted with respect to the medium boundaries at an angle of φ. The grating vector $K = 2\pi / \Lambda$, where Λ is the period of the grating. The same average dielectric constant is assumed for the region inside and outside the grating boundaries. The angle of incidence wave is θ.

Wave propagation in the grating is described by the scalar wave equation

$$\nabla^2 E + k^2 E = 0 \tag{4.1}$$

where $E(x, z)$ is the complex amplitude of the y component of the electric field, which is assumed to be independent of y and to oscillate with an angular frequency ω. The propagation constant $k(x, z)$ is spatially modulated and related to the relative dielectric constant $\varepsilon(x, z)$ and the conductivity $\sigma(x, z)$ of the medium by

$$k^2 = \frac{\omega^2}{c^2}\varepsilon - j\omega\mu_0\sigma \tag{4.2}$$

where c is the light velocity in free spacing and μ_0 is the permeability of the medium which we assume to be equal to that of free spacing. The fringes of the volume grating are represented by a spatial modulation of ε or σ

$$\varepsilon = \bar{\varepsilon} + \varepsilon_1 \cos\left(\vec{K} \cdot \vec{x}\right) \tag{4.3}$$

$$\sigma = \bar{\sigma} + \sigma_1 \cos\left(\vec{K} \cdot \vec{x}\right) \tag{4.4}$$

where ε_1 and σ_1 are the amplitudes of the spatial modulation, $\bar{\varepsilon}$ is the average dielectric constant and $\bar{\sigma}$ the average conductivity. ε and σ are assumed to be modulated in phase. To simplify the notation we use the radius vector $\vec{x}$ and the grating vector $\vec{K}$

$$\vec{x} = \begin{bmatrix} x \\ y \\ z \end{bmatrix}; \qquad \vec{K} = K \begin{bmatrix} \sin\varphi \\ 0 \\ \cos\varphi \end{bmatrix}; \qquad K = 2\pi / \Lambda.$$

Equations (4.2) - (4.4) can be combined in the form

$$k^2 = \beta^2 - 2j\alpha\beta + 2\kappa_c\beta \left(e^{j\vec{K}\cdot\vec{x}} + e^{-j\vec{K}\cdot\vec{x}}\right) \tag{4.5}$$

where we have introduced the average propagation constant β and the average absorption constant α:

$$\beta = \frac{2\pi\sqrt{\bar{\varepsilon}}}{\lambda} \tag{4.6}$$

$$\alpha = j\mu\frac{c\bar{\sigma}}{2\sqrt{\bar{\varepsilon}}} \tag{4.7}$$

and the coupling constant κ_c was defined as

$$\kappa_c = \frac{1}{4}\left(\frac{2\pi}{\lambda}\frac{\varepsilon_1}{\sqrt{\bar{\varepsilon}}} - j\mu_0\frac{c\sigma}{\sqrt{\bar{\varepsilon}}}\right) \tag{4.8}$$

This coupling constant describes the coupling between the incident wave A_i and diffracted wave A_d. For $\kappa_c = 0$ there is no coupling between A_i and A_d, therefore, there is no diffraction.

Optical media are usually characterized by their refractive index and their absorption constant. If the following conditions are met

$$\frac{2\pi n}{\lambda} >> \alpha \; ; \quad \frac{2\pi n}{\lambda} >> \alpha_1 ; \quad n >> n_1 \tag{4.9}$$

here n is the average refractive index; n_1 and α_1 are amplitudes of the spatial modulation of the refractive index and the absorption constant, respectively; λ is the wavelength in free spacing, we can write with good accuracy

$$\beta = 2\pi \frac{n}{\lambda} \tag{4.10}$$

and for the coupling constant

$$\kappa_c = \pi \frac{n_1}{\lambda} - j\frac{\alpha_1}{2} \tag{4.11}$$

The spatial modulation indicated by n_1 or α_1 forms a grating which couples the two waves A_i and A_d, and leads to an exchange of energy between them. We describe these waves by complex amplitudes $A_i(z)$ and $A_d(z)$ which are along z as a result of this energy interchange or because of an energy loss from absorption. The total electric field in the grating is the superposition of the two waves:

$$E = A_i(z)e^{-j\vec{\rho}\cdot\vec{x}} + A_d(z)e^{-j\vec{\sigma}\cdot\vec{x}} \tag{4.12}$$

The propagation vectors ρ and σ contain the information about the propagation constants and the directions of propagation of $A_i(z)$ and $A_d(z)$. ρ is assumed to be equal to the propagation vector of the free incident wave in the absence of coupling. σ is forced by the grating and related to ρ and the grating vector by

$$\sigma = \rho - K \tag{4.13}$$

which has the appearance of a conservation of momentum equation.

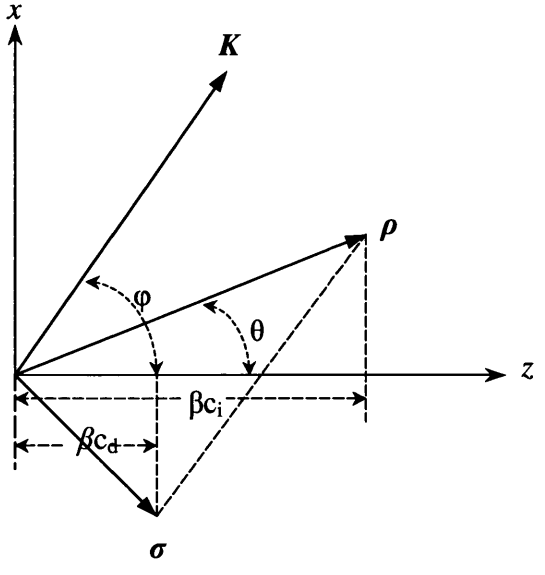

Fig. 4.2 ρ and σ, the propagation vectors of the incident wave A_i and diffraction wave A_d, and their relation to the grating vector K. The obliquity factors βc_i and βc_d are indicated.

Figure 4.2 shows the vectors of interest and their orientation. The components of $\boldsymbol{\rho}$ are ρ_x and ρ_z, which are given by

$$\boldsymbol{\rho} = \begin{bmatrix} \rho_x \\ 0 \\ \rho_z \end{bmatrix} = \beta \begin{bmatrix} \sin\theta \\ 0 \\ \cos\theta \end{bmatrix} \tag{4.14}$$

From equations (4.13) and (4.14), we get the $\boldsymbol{\sigma}$ components σ_x and σ_z

$$\boldsymbol{\sigma} = \begin{bmatrix} \sigma_x \\ 0 \\ \sigma_z \end{bmatrix} = \beta \begin{bmatrix} \sin\theta - \dfrac{K}{\beta}\sin\varphi \\ 0 \\ \cos\theta - \dfrac{K}{\beta}\cos\varphi \end{bmatrix} \tag{4.15}$$

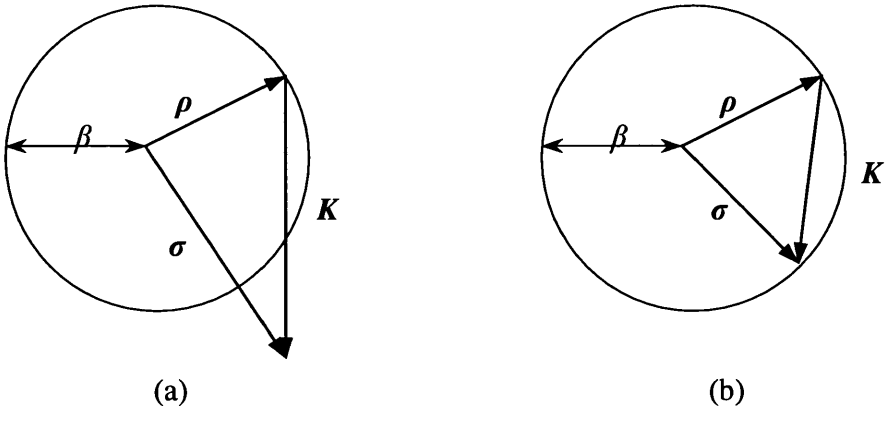

Fig. 4.3 Vector diagram (conservation of momentum) for (a) near and (b) exact Bragg incidence.

The vector relation (4.13) is shown in Fig. 4.3 together with a circle of radius β. The general case is shown in Fig. 4.3 (a), where the Bragg condition is not met and the length of σ differs from β. Fig. 4.3 (b) shows the same diagram for incidence at the Bragg angle θ_0. In this special case the lengths of both ρ and σ are equal to the free propagation constant β, and the Bragg condition

$$\cos(\varphi - \theta) = \frac{K}{2\beta} \tag{4.16}$$

is obeyed. For unslanted gratings, $\varphi = \pi/2$, and using the definitions of $K = 2\pi / \Lambda$ and $\beta = 2\pi \frac{n}{\lambda}$, respectively, Eq. (4.16) becomes

$$\sin\theta = \frac{\lambda}{2n\Lambda} \tag{4.17}$$

which is the normal form of the Bragg condition used in most papers, and the incident wave ($\theta = \theta_0$) is said to be "Bragg-matched" to the grating.

4.2 Diffraction efficiency for the transmission gratings

The incident wave A_i and the diffracted wave A_d can be solved by the coupled wave equations [1]

$$A_i(z) = r_1 \exp(\gamma_1 z) + r_2 \exp(\gamma_2 z) \tag{4.18}$$

$$A_d(z) = s_1 \exp(\gamma_1 z) + s_2 \exp(\gamma_2 z) \tag{4.19}$$

where r_1, r_2, s_1 and s_2 are constants which depend on the boundary conditions, and the constants $\gamma_{1,2}$ are

$$\gamma_{1,2} = -\frac{1}{2}\left(\frac{\alpha}{c_i} + \frac{\alpha}{c_d}\right) \pm \frac{1}{2}\left[\left(\frac{\alpha}{c_i} - \frac{\alpha}{c_d}\right)^2 - 4\frac{\kappa^2}{c_i c_d}\right]^{\frac{1}{2}} \tag{4.20}$$

For transmission gratings, $c_d > 0$, the boundary conditions are

$$A_i(0) = 1, \qquad A_d(0) = 0 \tag{4.21}$$

Inserting (4.21) into equations (4.18) and (4.19), we get

$$r_1 + r_2 = 1 \tag{4.22}$$

$$s_1 + s_2 = 0 \tag{4.23}$$

And combining the relations

$$s_1 = -s_2 = -j\frac{\kappa}{c_d(\gamma_1 - \gamma_2)} \tag{4.24}$$

We can obtain the expression for the amplitude of the diffracted wave at the output of the grating

$$A_d(d) = j\frac{\kappa}{c_d(\gamma_1 - \gamma_2)}[\exp(\gamma_2 d) - \exp(\gamma_1 d)] \tag{4.25}$$

this is a general expression, which is valid for all types of thick transmission grating including the cases of off-Bragg incidence, of lossy gratings and of slanted fringe planes.

The diffraction efficiency can be defined as

$$\eta = \frac{c_d}{c_i} A_d A_d^* \tag{4.26}$$

where A_d is the (complex) amplitude of the output signal for a reference wave A_i incident with unit amplitude. η is the fraction of the incident light power which is diffracted into the signal wave. A_d is equal to $A_d(d)$ for transmission grating.

For the case of unslanted gratings ($\varphi = \pi/2$) and Bragg incidence ($\theta = \theta_0$) Eq. (4.25) simplifies to

$$A_d = -j\exp(-\alpha d / \cos\theta_0)\sin(\kappa d / \cos\theta_0) \tag{4.27}$$

where κ is complex. The expression for the diffracted efficiency of unslanted gratings is

$$\eta = A_d A_d^* = \left[\sin^2\left(\pi \frac{n_1 d}{\lambda \cos\theta_0}\right) + sh^2\left(\frac{\alpha_1}{2\cos\theta_0}\right)\right] \exp\left(-\alpha \frac{2d}{\cos\theta_0}\right) \tag{4.28}$$

For completeness we give the diffracted efficiency for the lossless dielectric grating, i.e. $\alpha = \alpha_1 = 0$. Equation (4.28) thus becomes the well-known Kogelnik expression [1]

$$\eta = \sin^2\left(\pi \frac{n_1 d}{\lambda \cos\theta_0}\right) \tag{4.29}$$

which was first obtained by several workers whose prime interest was light diffraction by acoustic waves about half the century ago [2, 3].

Hong and Saxena [4] presented an analytic solution of the coupled-wave equations including energy coupling between the recording beams and neglecting grating bending. The steady-state result can easily be extended to the dynamic case by using the time-dependent expressions for spacing-charge field (see section 3.2) to obtain

$$\eta(t) = \sin^2\left[\frac{1}{2}\delta\{a^2(t) + b^2(t)\}^{1/2} \times \left(\frac{4}{\Gamma(t)}\left\{\arctan\left[\frac{\exp\Gamma(t)L/2}{\sqrt{m}}\right] - \arctan\left(\frac{1}{\sqrt{m}}\right)\right\}\right)\right] \tag{4.30}$$

where $\delta = 2\pi r_{eff}\zeta / \lambda n \cos\theta$, $r_{eff}\zeta$ is the product of effective electro-optic coefficient and hole-electron competition factor, m is the incident beam ratio, and the time-dependent gain coefficient $\Gamma(t) = -2\delta b(t)$. $a(t)$ and $b(t)$ are the time evolution expressions of the real and the imaginary components of the spacing-charge field as defined in Eqs. (3.14) and (3.15). The first terms in Eq. (4.30) $\frac{1}{2}\delta\{a^2 + b^2\}^{1/2}$ represent the index modulation developed in the absence of coupling. And the term $\frac{4}{\Gamma(t)}\left\{\arctan\left[\frac{\exp\Gamma(t)L/2}{\sqrt{m}}\right] - \arctan\left(\frac{1}{\sqrt{m}}\right)\right\}$ acts as a reduced effective crystal thickness ($0 \le L_{eff} \le L$) reflecting the reduced index modulation caused by the initial beam intensity ratio, including the effects of energy coupling between the recording beams. In the limit as Γ approaches zero (the grating in phase with the interference pattern), L_{eff} goes to $m'L$, here $m' = 2(I_1 I_2)^{1/2}/(I_1 + I_2)$ is the beam modulation, and Eq.(4.30) reduces to Kogelnik's expression from a uniform volume grating,

$$\eta(t) = \sin^2\left[\frac{\pi L n_1(t)}{\lambda \cos\theta}\right] \tag{4.31}$$

where $n_1(t)$ is the time evolution of the index modulation amplitude, as expressed in Eq. (3.18).

4.3 Experimental results

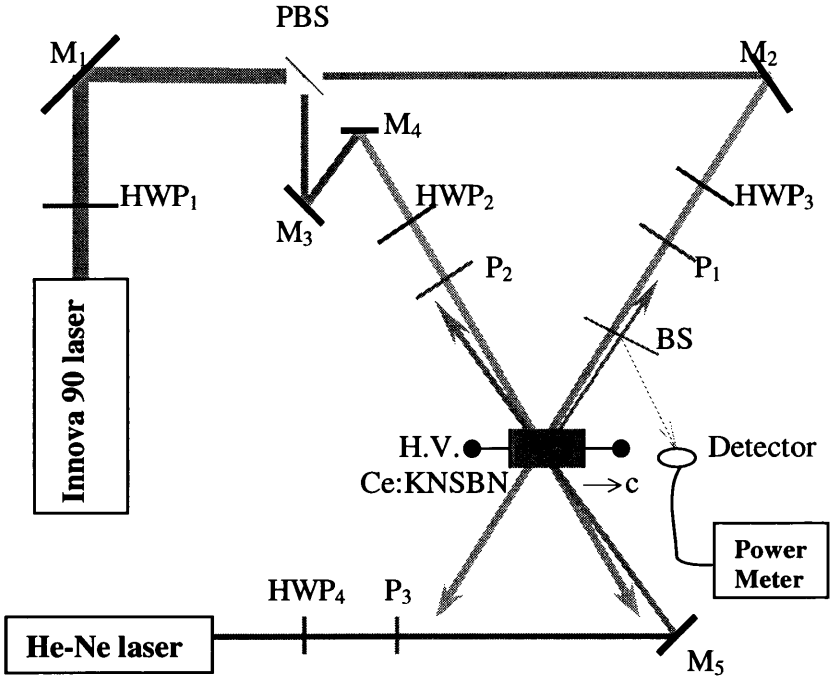

Fig.4.4 Experimental set-up for measuring the diffraction efficiency. HWP_i are half-wave-polarizers; M_i are reflective mirrors; P_i are polarizers; and H.V. is a high-voltage. BS is beam-splitter and PBS is a polarize-beam-splitter.

Figure 4.4 is the experimental set-up for measuring the diffraction efficiency. The Ce:KNSBN we use is a cubic crystal of 5.5 mm × 5.5 mm × 5.5 mm. Electrical contact is made to the sample by using silver-paint electrodes on the *c* face. The electric field is applied by a high-voltage supply. The gratings oriented along the *c* axis are written by two Innova-90 laser beams (λ = 514nm) with an average intensity of 10 mW/cm^2, the incident beam ratio m = 1. The grating spacing (Λ_g) is depended on the angle (θ) between

the two beams $\Lambda_g = \frac{\lambda}{2n\sin(\theta)}$. A He-Ne laser beam ($\lambda$ = 632.8 nm) with an intensity of 0.8 mW/cm^2 was used as the 'probe-beam'. The intensity of light diffracted from the grating is measured using a photo-detector connected to a power meter. The diffracted intensity is a direct indication of the amplitude of photorefractive response of the Ce:KNSBN crystal. The He-Ne laser output is energetically insufficient to greatly affect the photorefractive gratings and so, together with its low intensity, provides non-destructive monitoring. The definition of diffraction efficiency used here is that of the diffracted intensity divided by the intensity of the He-Ne beam illuminated on the crystal.

4.3.1 Time evolution of the diffraction efficiency

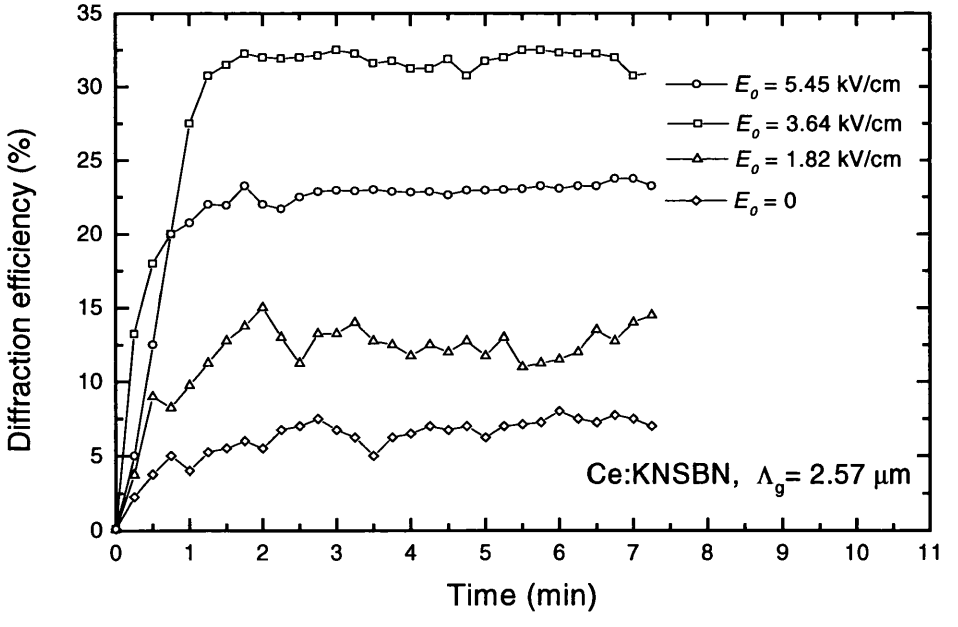

Fig. 4.5 Time evolution of the diffraction efficiency of gratings recorded in Ce:KNSBN at various applied fields. Λ_g= 2.57 μm.

Figure 4.5 illustrates the time evolution of the diffraction efficiency with a grating spacing Λ_g = 2.57 μm. The results were obtained for 4 values of applied electric field ranging from 0 to 5.45 kV/cm. Prior to each measurement any previous gratings were erased by uniformly illuminating the crystal with only one of the writing beams. The diffraction efficiency was monitored as it evolved over a period of several minutes. It can be seen from the figure that the time evolution to a saturated state becomes less while the applied electric field increase, and the application of an external electric field enhances the diffraction efficiency (by approximately a factor of 5 for E_0 = 3.64 kV/cm) but that interestingly there appears to be an optimum value for the applied field i.e. the maximum diffraction efficiency occurs for E_0 = 3.64 kV/cm.

4.3.2 Applied electric field history's effect

It is well known that gratings can be stored in a Ce:KNSBN crystal in the dark for several days and in some cases this can lead to confusing results unless it is ensured that at the start of an experiment any previously recorded gratings have been effectively erased. To the best of our knowledge however there have been no reports about the electric field history having any influence on the diffraction efficiency.

Figure 4.6 illustrates how the diffraction efficiency varies as the electric field is varied through a continuous cycle. The experimental conditions are such that again Λ_g = 2.57 μm and the gratings were erased prior to each measurement. The diffraction efficiency

values and their associated errors were determined from results such as shown in Figure 4.5, i.e. the diffraction efficiency and its error were calculated from a set of values obtained after several minutes. In terms of Figure 4.6 the measurements for route 'A' began at zero applied field (E_0 = 0) to E_0 = 5.45 kV/cm, and then back to E_0 = 0; The field direction was then reversed by swapping terminals and the cycle to E_0 = -5.45 kV/cm and back to E_0 = 0 completed. For route 'B' the cycle is in reverse order i.e. 0 to -5.45 kV/cm etc. It should be repeated that prior to each measurement of diffraction efficiency any previous gratings were erased.

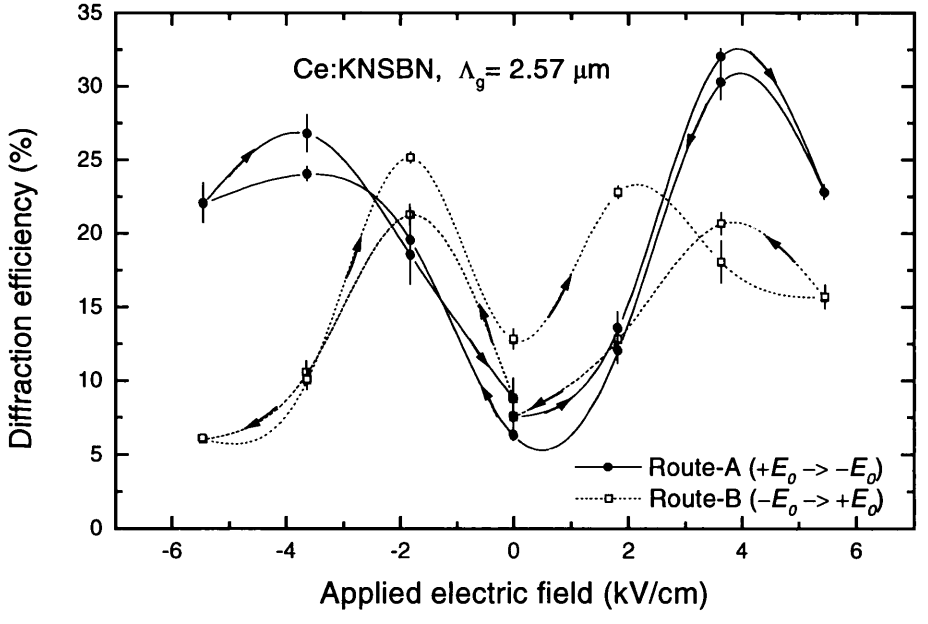

Fig. 4.6 A complete cycle, for two different routes, showing how the diffraction efficiency depends on the history of the electric field applied to the crystal — the lines joining the points are merely to guide the eye. Λ_g = 2.57μm.

Inspection of Figure 4.6 leads to a number of observations:

a) For almost all values of applied electric field, including zero but ignoring the end points of the cycles, there are at least two possible results for the measured diffraction efficiency.

b) For a given route (*A* or *B*) the curve is not symmetric i.e. the optimum field depends on polarity.

c) For one complete cycle, e.g. 0, + E_0, 0, - E_0, and 0, the diffraction efficiency returns, within errors, to its original value, i.e. the cycles, are closed.

d) The optimum field and its resulting diffraction efficiency depends on the cycle direction e.g. the diffraction efficiency at E_0 = 3.64 kV/cm is different for routes *A* and *B*, i.e. on the history of the applied field.

e) The diffraction efficiency for a particular applied field and route also depends on the history of the applied field e.g. for route '*B*' the diffraction efficiency at E_0 = 1.82 kV/cm has two quite different values.

For comparison we present a similar set of results for a fringe spacing Λ_g = 1.88 μm in Figure 4.7. It can be seen that although there are differences in detail the same broad trend is again emerging, and similar comments to those above apply. In fact this is true for all grating spacings we have investigated in the range from 1.88 μm to 4.6 μm.

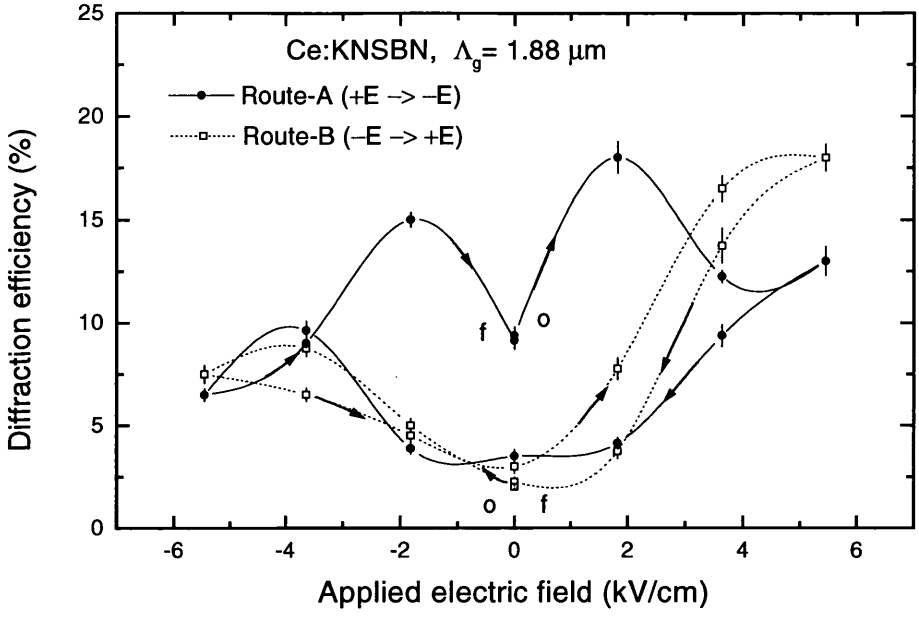

Fig. 4.7 As for Figure 4.6 with Λ_g = 1.88 μm

4.3.3 Optimum applied electric field and grating spacing

We present in figure 4.8 the dependence of the diffraction efficiency on the applied field as a function of grating spacing. In order to avoid ambiguity due to the history or memory effect all gratings were erased prior to a measurement and each result was obtained at the same part of the same route i.e. the history was identical for each measurement.

Inspection of Figure 4.8 leads to a number of observations:

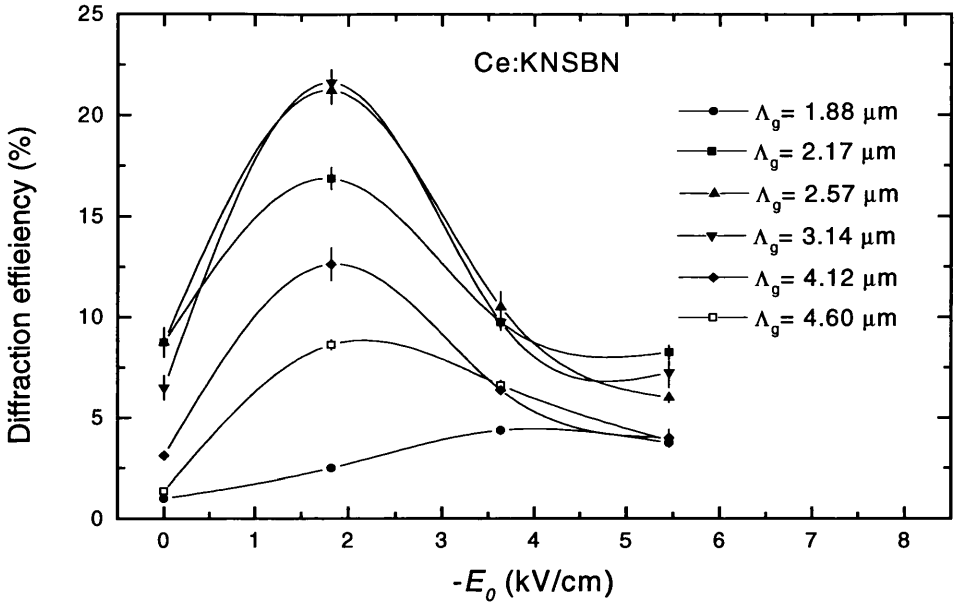

Fig. 4.8 Variation of diffraction efficiency with applied field (identical history) as a function of grating spacing Λ_g. Again the solid lines are to guide the eye.

a) The maximum diffraction efficiency occurs at a grating spacing of Λ_g = 3.14 μm and applied field E_0 = -1.82 kV/cm (the field polarity for this set of results corresponds to negative values for E_0 in figures 4.6 and 4.7).

b) Comparison of the results for Λ_g = 2.57 μm and 1.88 μm show agreement with figures 4.6 and 4.7 respectively on route '*B*' on the 'outward' journey from E_0 = 0.

c) For the range Λ_g = 2.17 μm to Λ_g = 4.60 μm the optimum field is approximately constant at E_0 = 1.82 kV/cm.

d) The diffraction efficiency initially increases with the applied field and then begins to drop at about 1.82 kV/cm.

4.4 Calculations and discussions

Using the parameters of Ce:KNSBN we measured at zero applied electric field (see chapter 3), we can calculate the diffraction efficiency as the functions of evolution time, applied electric field, and grating spacing according to the equations in section 4.2. In this section we will give some calculation results and compare with those from the experiments.

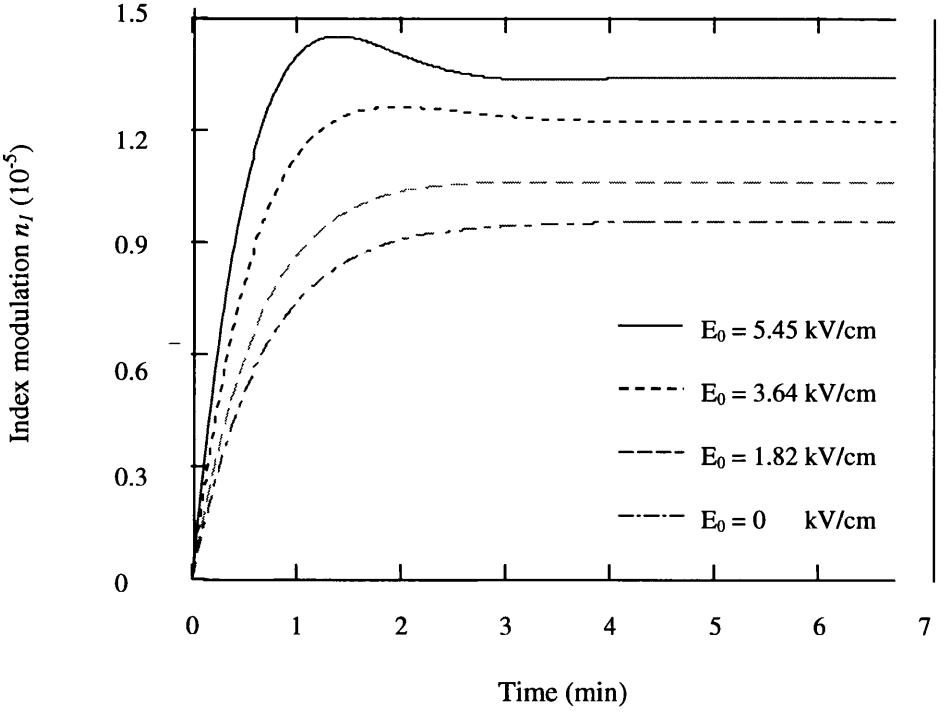

Fig. 4.9 The time evolution of the index modulation amplitude dependence on applied electric field in Ce:KNSBN, Λ_g = 2.57 μm.

Figure 4.9 is the time evolution of the index modulation amplitude depending on applied electric field in Ce:KNSBN calculated by Eq. (3.18). And using the Kogelnik's expression of Eq. (4.31), we got the time evolution of the diffraction efficiency depending on applied electric field as shown in Fig. 4.10.

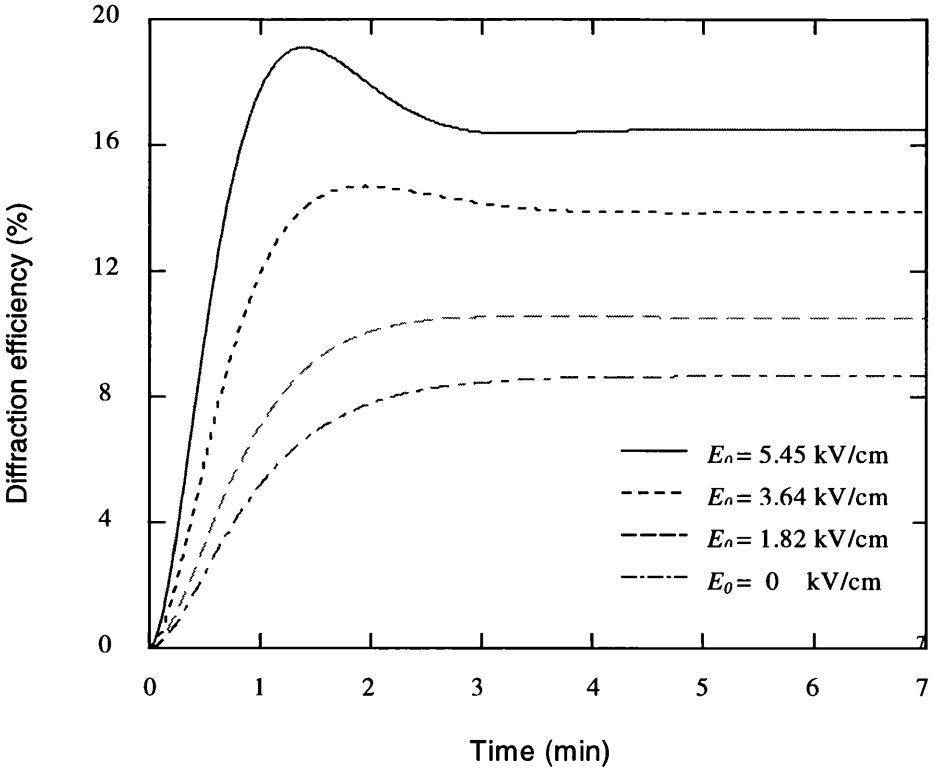

Fig. 4.10 The time evolution of the diffraction efficiency dependence on applied electric field in Ce:KNSBN, Λ_g = 2.57 μm.

We found that the sensitivity increases with the applied electric field, and if the applied field is greater than the certain value (E_0 ~ 3.64 kV/cm, in Fig. 4.10), the diffraction efficiency will first reach its peak value, then, go down to its saturation one. Such time

evolution of the diffraction efficiency is the same as that we observed in our experiment, although the peak value was not shown clearly in Fig. 4.5, we did find such phenomenon during the experiment. However, the calculated results show that the diffraction intensity increases with the applied field, and there is not any optimum applied field value as we found in our experiment.

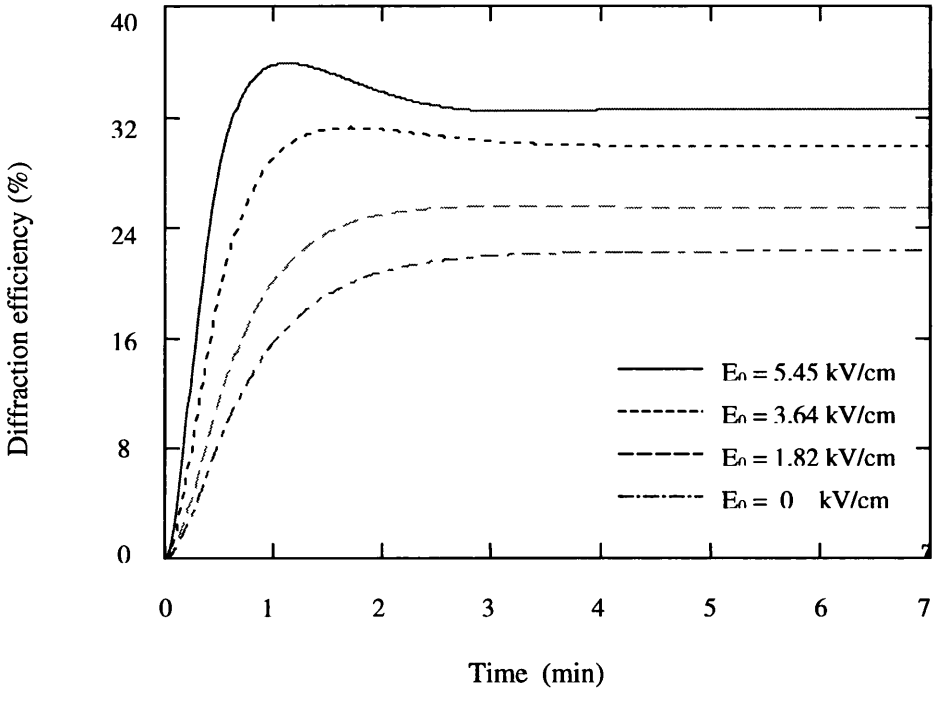

Fig. 4.11 The time evolution of the diffraction efficiency dependence on applied electric field in Ce:KNSBN, considering the effective crystal thickness L_{eff}, $\Lambda_g = 2.57$ μm.

Fig. 4.11 shows the time evolution of the diffraction efficiency dependence on applied electric field in Ce:KNSBN using Eq (4.30), considering the effective crystal thickness

L_{eff}, which reflects the reduced index modulation caused by the initial beam intensity ratio, including the effects of energy coupling between the recording beams (The result of Fig. 4.10 is only the approximation corresponding to Γ approaching zero). We found that the curves are similar to those in Fig. 4.10, but the time evolution is slightly more sensitive with the increasing of the applied electric field. And again the diffraction intensity increases with the applied field, and there exists no optimum applied field value as we found in our experiment.

Comparing the absolute value of the diffraction efficiency in Fig. 4.10 and Fig. 4.11 with our experimental results in Fig. 4.5, we found that the experimental data were near the calculated ones in Fig. 4.10 for lower applied field, and approached the results in Fig. 4.11 for higher applied field, relatively. It means that for lower applied electric field the spacing grating in Ce:KNSBN crystal is in phase with the incident beam interference pattern, and for higher applied field the energy-coupling limits the interaction length in the crystal we should consider the effective crystal thickness in our analysis.

Figure 4.12 shows the variation of saturated diffraction efficiency with applied electric field for different grating spacing, calculated by Eq. (4.30) using the steady-state amplitude of the spacing-charge field, Eqs. (3.12) and (3.13), to substitute for the time evolution expressions of the spacing-charge field $a(t)$ and $b(t)$. We found that in the region of the grating spacings in our experiment, Λ_g from 1.88 μm to 4.60 μm, there seemed no optimum applied field for the diffraction efficiency. When the grating spacing increases, there appears the optimum applied field, and the value of the optimum field

becomes less while the grating spacing increases. In Fig. 4.12 we show the $\eta \sim E_0$ curve for Λ_g = 30 μm. There did exist an optimum applied field, $(E_0)_{opt}$ ~ 3 kV/cm, but the related diffraction efficiency reaches 100%. However, in our experiment, only for the small grating spacing, for example Λ_g = 1.88 μm, we did not observe the optimum field for diffraction efficiency. For most grating spacings (see Fig. 4.8) there exist the optimum field $(E_0)_{opt}$ ~ 3.0 kV/cm, and furthermore, there seems an optimum grating spacing $(\Lambda_g)_{opt}$ ~2.0 μm, which related to the maximum diffraction efficiency.

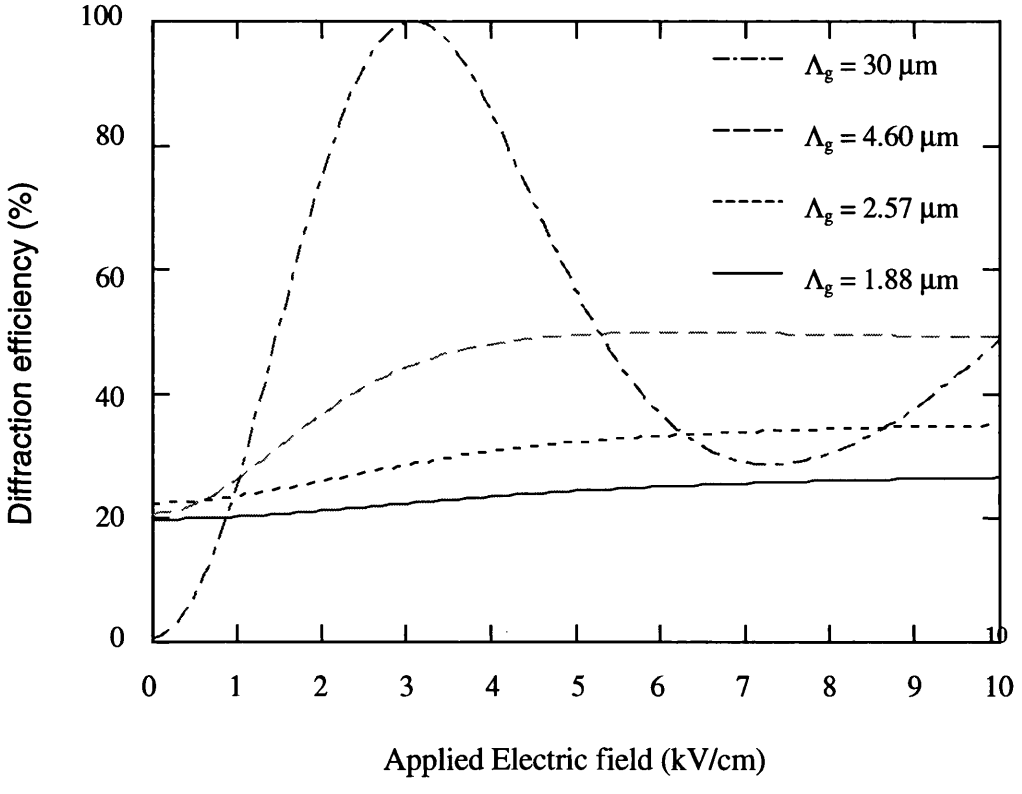

Fig. 4.12 Diffraction efficiency dependence on applied electric field for different grating spacing Λ_g.

The discrepancy between the calculation and the experiment was due to higher-order terms not included in the theory. All the calculations based on Kukhtarev's theory are accurate for low modulation depths. However, in our experiment, the incident beam ratio $m \sim 1$. And the beam fanning was not considered in the calculation, but the fanning loss was very serious for high fields [5]. For the thick Ce:KNSBN crystal in our experiment, we think the diffraction efficiency dropping at high applied field was probably due to fanning loss.

For the Ce:SBN crystal, which has the similar structure of Ce:KNSBN crystals, Ford *et al* [6] used several different theoretical diffraction efficiency calculations: (i) neglecting all coupling (grating bending, energy transfer, and fanning) by substituting the index modulation directly into the Kogelnik volume diffraction formula; (ii) using Vahey's solution [7], which includes coupling but assume that the index evolution follows the local form of the writing interference pattern; and (iii) using Kukhtarev's solution [8], also including both coupling and grating bending. They found similar results as we just mentioned, i.e. all the methods were equally accurate during the initial stages of grating formation but showed different behaviour near saturation, and none matched the experimental results at high fields, where fanning is strong.

There has not been any theory to discuss the applied electric field history's effect on diffraction efficiency we found in our experiment. It is well known that the electric displacement versus external dc electric field applied on the *c* axis of the ferroelectric material shows a hysteresis loop. For Ce:SBN J. Ma *et al* [9] observed a hysteresis loop

showing the relationship between gain G and the applied field E_0. However, the cycles showing the diffraction efficiency depending on the history of the applied electric field in our experiment (see Fig. 4.6 and Fig. 4.7) seem more complicated in detail. The cycles were not symmetric for applied field E_0, and the optimum applied field always changed for different routes. The source of the complication is unknown. There are some possibilities:

1) Higher applied field and longer exposures caused strong fanning effects in the crystal, as we mentioned above.
2) Long term effects of the applied field might cause the crystal to have been partially depoled or experienced some kind of domain reversal [10].
3) Spatial field nonuniformities from charge compensation could cause diffraction nonuniformity across the crystal aperture [11].
4) Thermal effects caused by long illumination might change some characterization parameters in the crystal.

4.5 Conclusions

The time evolution of the diffraction efficiency under an applied electric field can be predicted accurately with the material parameters measured at zero applied field. Although the theoretical calculation shows that the diffraction efficiency increase with the applied electric field and the grating spacing in the crystal, in the experiment there

exist some optimum applied electric fields, which are related to the maximum diffraction efficiency in the experiment. The diffraction efficiency drops at higher applied field was due to the fanning loss in the thick crystal. The applied electric field history's effect on diffraction efficiency is probably due to the hysteresis of ferroelectric material. There are several possibilities which cause the phenomenon to become more complicated in our experiment.

Chapter 4: References:

1. H. Kogelnik, "Coupled wave theory for thick hologram grating", The Bell System Technical Journal, vol. 48, No. 9, pp2909-2947, 1969
2. A. B. Bathia, W. J. Noble, "Diffraction of light by ultrasonic waves II". Proc. Royal Soc. of London, 220A, pp369-385, 1953
3. P. Phariseau, "On the diffraction of light by progressive supersonic waves", Proc. Ind. Acad. Sci., 44A, pp165-170, 1956
4. J. Hong and R. Saxena, "Diffraction efficiency of volume holograms written by coupled beams", Opt. Lett. Vol.16, pp180-182, 1991
5. W.W.Clark, G. L. Wood, M.J. Miller, E. J. Sharp, G. J. Salamo, B. Monson and R. Neurgaonkar, " Enhanced photorefractive beam fanning due to internal and external electric fields", Appl. Opt., vol. 29, pp1249-1258, 1990

6. J. E. Ford, J. Ma, Y. Fainman, S. H. Lee, Y. Taketomi, D. Bize, and R. R. Neurgaonkar, "Multiplex holography in strontium barium niobate with applied field", J. Opt. Am. A, vol. 9, No. 7, pp1183-1192, 1992

7. D. W. Vahey, "A nonlinear coupled-wave theory of holographic storage in ferroelectric materials", J. Appl. Phys. Vol. 46, pp3510-3515, 1975

8. N. V. Kukhtarev, "Kenetics of hologram recording and erasure in electrooptic crystal", Sov. Tech. Phys. Lett. Vol. 2, pp438-440, 1976

9. J. Ma, L.Liu, S. Wu, Z. Wang, L. Xu, and B. shu, "Electrocontrolled beam coupling and bistabel behavior in SBN:Ce crystals", Appl. Phys. Lett. Vol. 53, No. 10, pp826-829, 1988

10. J. P. Wilde and L. Hesselink, "Electro-optic effects an domain reversal in SBN" in *Photorefractive Materials, Effects, and Devices* (OSA Technical Digest Series), vol. 14, pp151-154, 1991

11. V. N. Astratov and A. V. Il'inski, "Direct investigation of the electric field distribution in a BGO crystal with the aid of the transverse electrooptic effect", Sov. Phys. Solid State, vol. 24, pp61-64, 1982

Chapter 5. Phase conjugation

5.1 Introduction

Phase conjugators are optical devices that can produce a time-reversed replica of incident electromagnetic radiation [1] - [4]. The unique property of phase reversal (wavefront reversal) offers the possibility of many novel device applications. These include image restoration in optical fibers [5], [6], phase-conjugate interferometers and image subtractors [7], [8], phase conjugate fiber-optic gyros [10] - [14], and many other applications [15], [16]. Although phase conjugate waves can be generated by using deformable mirrors whose surfaces match exactly the wavefront of the incident wave, a real time operation requires the technique of nonlinear optics. Phase conjugate waves can be generated by stimulated Brillouin scattering (SBS) and optical four-wave mixing in third-order nonlinear media ($\chi^{(3)}$-media) [1], [3]. The operation in $\chi^{(3)}$-media often requires high intensity (~1 MW/cm^2) or high power for the incident electromagnetic waves.

Consider the propagation of an electromagnetic wave along the z axis. Let the electric field be written

$$E = A\cos(\omega t - kz - \phi) \tag{5.1}$$

where ω is the frequency and k is the wave number; the amplitude A and phase ϕ are real functions of position (x, y, z). If the amplitude is a slowly varying function of z compared with $\cos(\omega t - kz - \phi)$, the propagation of the wave can be easily described in terms of the motion of the wavefronts. Wavefronts are three-dimensional surfaces defined as $kz + \phi(r)$ = constants. For any electromagnetic wave given by (5.1), the phase conjugate of it is given by

$$E_c = A\cos(\omega t + kz + \phi) \tag{5.2}$$

E_c and E form a conjugate pair.

By examining (5.1) and (5.2), we find that these two waves have exactly the same wavefronts at any point in space. The motion of these two sets of wavefronts is, however, in opposite directions. If we reverse the sign of t in E, we obtain E_c so the phase conjugate wave is often referred to as a time-reversed wave. As a matter of fact, if E in (5.1) satisfies the wave equation,

$$\left[\nabla^2 - \frac{n^2}{c^2}\frac{\partial^2}{\partial t^2}\right]E = 0 \tag{5.3}$$

it can be shown easily, by virtue of time reversal symmetry, that E_c given by (5.2) is also a solution to the wave equation provided $n(x, y, z)$ is real and independent of t.

Using the analytic representation, we write (5.1) as

$$E = A(\vec{r})e^{i[\omega t - kz - \phi(\vec{r})]} \tag{5.4}$$

where we remember that only the real part of the right-hand side is the physical value of the electric field. If we further define a complex quantity

$$A_1(\vec{r}) = A(\vec{r})e^{-i\phi(\vec{r})} \tag{5.5}$$

then the electric field is written

$$E = A_1(\vec{r})e^{i(\omega t - kz)} \tag{5.6}$$

Using these definitions, the phase conjugate wave can be written

$$E_c = A_1^*(\vec{r})e^{i(\omega t + kz)} \tag{5.7}$$

We note that the phase conjugate wave propagates along the $-z$ direction with a complex amplitude A_1^*. It is important to note that to get E_c from E, we take the complex conjugate of the spatial part only, leaving the factor $\exp(i\omega t)$ intact.

To appreciate the property of phase conjugation, we consider the propagation of a plane wave through a distorting medium such as the atmosphere (Fig. 5.1(a)). Let the distorting

medium be confined in the region between $z = 0$ and $z = L$. As a result of the index inhomogeneity, the wavefronts of the transmitted wave are no longer planar (see Fig. 5.1(a)). Let the electric field of the forward propagating beam ($+z$) be represented by (5.6). Using the slowly varying amplitude approximation, the complex amplitude must obey the following equation:

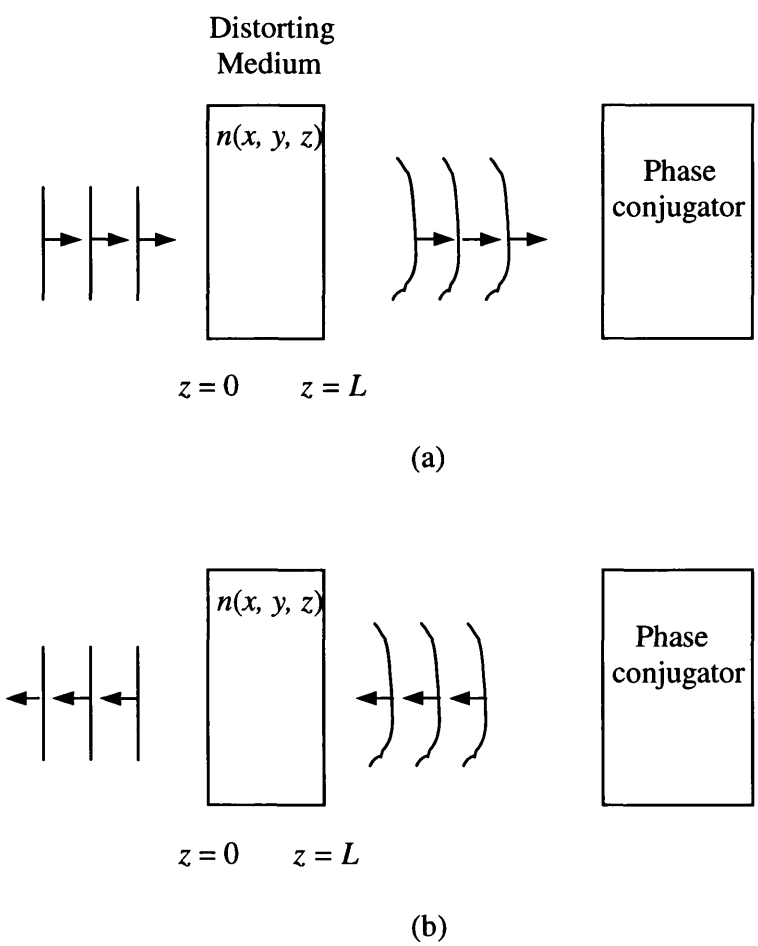

Fig. 5.1 Propagation of phase conjugate waves.

$$\nabla_{\perp}^2 A_1 + \left[\frac{\omega^2}{c^2} n^2(x,y,z) - k^2\right] A_1 - 2ik\frac{\partial}{\partial z} A_1 = 0 \tag{5.8}$$

We recall that this approximation is valid provided the fractional variation of $n(x, y, z)$ in one wavelength is small compared to unity. It is important to note that this is a first order differential equation in z. Thus if A_1 is known for some $z = z_0$ and for all x, y, then A_1 is determined for all points in space provided $n(x, y, z)$ is known.

We now consider the complex conjugate of (5.8) as a purely mathematical operation:

$$\nabla_{\perp}^2 A_1^* + \left[\frac{\omega^2}{c^2} n^2(x,y,z) - k^2\right] A_1^* + 2ik\frac{\partial}{\partial z} A_1^* = 0 \tag{5.9}$$

This is also a scalar wave equation obeyed by a wave propagating in the $-z$ direction of the form

$$E_2 = A_2 e^{i(\omega t + kz)} \tag{5.10}$$

provided we put

$$A_2 = \rho' A_1^* \qquad \text{for all } x, y, z \tag{5.11}$$

where ρ' is an arbitrary constant. What we have shown is that a wave $A_2 exp[i(\omega t + kz)]$ whose spatial component is everywhere the complex conjugate of $A_1 exp[i(\omega t + kz)]$, satisfies the same scalar wave equation. Since the scalar wave equation is first order in z, $A_2(x, y, z)$ for all x, y, z can be determined provided A_2 is known for all x, y, z at some $z = z_0$. In addition, if

$$A_2(x, y, z_0) = \rho' A_1^*(x, y, z_0), \qquad \text{for all } x, y \tag{5.12}$$

then

$$A_2(x, y, z) = \rho' A_1^*(x, y, z), \qquad \text{for all } x, y, z \tag{5.13}$$

Physically, this means that if in some plane $z = z_0$ (say $z_0 = L$ in Fig. (5.1)) we generate, by some means, a wave E_2 whose complex amplitude is the complex conjugate of that of E, then E_2 will propagate backwards and remain everywhere the complex conjugate of E. Its wavefronts everywhere thus coincide with those of E. Figure (5.1b) illustrates the propagation of E_2.

Figure 5.2 is the pictorial summary of optical phase conjugation techniques. From top to bottom: (a) A method of producing a phase conjugate wave is by four wave mixing in a nonlinear medium, traditionally by providing two counter-propagating pumping beams in addition to the input wave. (b) If the nonlinear medium is enclosed in an optical waveguide, only one pumping beam is necessary since the input wave can also act as the

second pumping beam. Two devices in which the pumping beams are internally generated have been demonstrated. (c) The pumping beams are supported in a resonant cavity consisting of external mirrors; (d) the pumping beams are fed back by internal reflection.

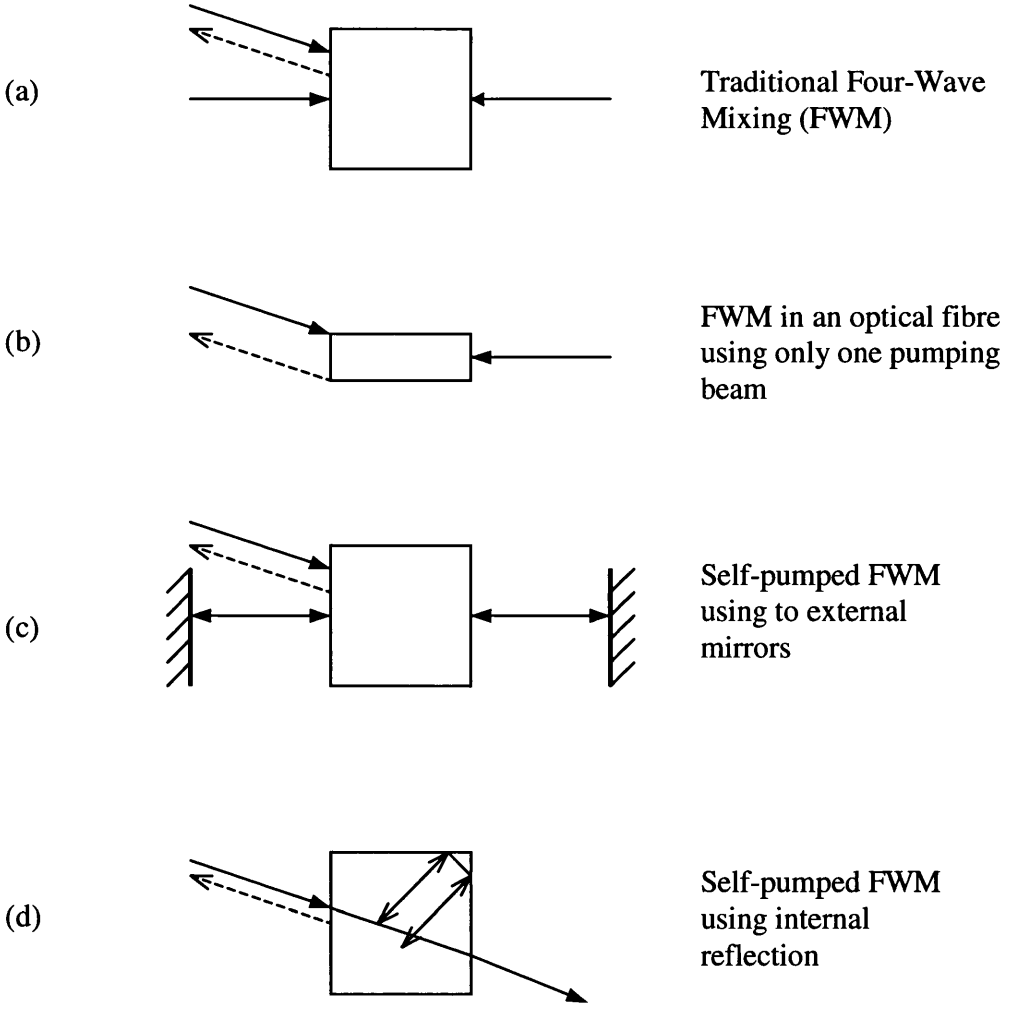

Fig. 5.2. Pictorial summary of optical phase conjugation techniques

5.2 Four-wave mixing phase conjugation

Four-wave mixing (FWM) is a traditional configuration for the generation of phase-conjugated waves. In this method, a nonlinear medium is pumped by a pair of counter-propagating laser beams. When a signal beam is incident into the medium, a fourth beam is generated. This beam is propagating opposite to the signal beam and is a time-reversed replica of the signal beam.

Since Yariv and Pepper [17] first applied the formalism of nonlinear optics to the study of four-wave mixing in nonlinear media, and predicted that amplified phase-conjugate reflection was possible, some photorefractive materials have been used effectively in phase conjugation via FWM configuration, such as BSO (first used in FWM by Huignard *et al* [18]), $BaTiO_3$ (first used in FWM by Feinberg *et al* [19]) and SBN (first used in FWM by Fischer *et al* [20]). These photorefractive crystals have very large electrooptic coefficients. The main disadvantage of these materials is their slow response time. The KNSBN crystal, with large coupling strengths and faster response time, seems very suitable to FWM phase conjugation experiment. However, to our knowledge, there is no report related to phase conjugation via FWM configuration in the KNSBN family. In this section, we will derive the expression of phase conjugation reflectivity in FWM configuration, and then discuss some experimental results for the Ce:KNSBN crystal.

5.2.1 Coupled wave equations and undepleted pumps approximation theory

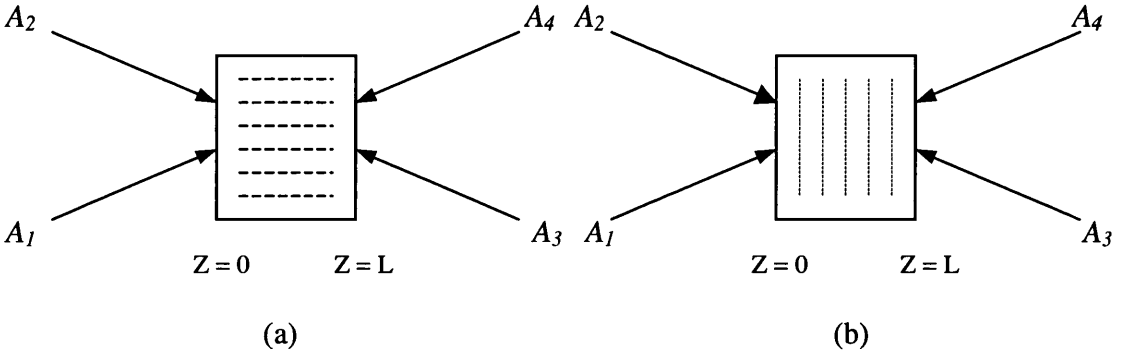

Fig.5.3 Four-wave mixing in photorefractive media. (a) transmission geometry and (b) reflection geometry.

Referring to Fig. 5.3, we consider the interaction of four beams in a photorefractive medium. Figure 5.3(a) shows the interaction of four waves via a transmission grating, whereas Figure 5.3(b) shows the interaction via a reflection grating. In many of the photorefractive wave mixing, the interaction via transmission gratings is often the dominant one. We will limit ourselves to a discussion of the configuration of transmission gratings. We assume that all beams have the same frequency ω. The electric field can be written

$$E = \sum_{j=1}^{4} A_j e^{i(\omega \cdot t - \vec{k}_j \cdot \vec{r})} \tag{5.14}$$

where A_1, A_2, A_3, A_4 are the complex amplitudes of the four waves, $\boldsymbol{k}_1$, $\boldsymbol{k}_2$, $\boldsymbol{k}_3$, $\boldsymbol{k}_4$ are the wavevectors. In (5.14), we assume that all wavevectors are in the same plane and all waves are polarized perpendicular to the plane. In the case when $A_3 = A_4 = 0$, there are only two waves and only one photorefractive grating (true only for the transmission geometry of Figure 5.3). The coupled equations can be written

$$\frac{d}{dz}A_1 = -\frac{1}{2}\Gamma\left(A_1 A_2^*\right)A_2 / I_0 \tag{5.15}$$

$$\frac{d}{dz}A_2 = \frac{1}{2}\Gamma^*\left(A_1^* A_2\right)A_1 / I_0 \tag{5.16}$$

where we assume no absorption ($\alpha = 0$), and Γ is the complex coupling constant.

In (5.15) and (5.16), the term $A_1 A_2^*$ represents the amplitude of the grating formed by A_1 and A_2. When all four waves are present there are in general six gratings in the medium. In the case of four-wave mixing for phase conjugation the wavevectors come in two oppositely directed pairs, i.e.,

$$\boldsymbol{k}_2 = -\boldsymbol{k}_3 \text{ and } \boldsymbol{k}_4 = -\boldsymbol{k}_1 \tag{5.17}$$

Four different gratings are represented by $(A_1 A_2^* + A_3 A_4^*)$, $(A_2 A_4^* + A_1 A_3^*)$, $(A_2 A_3^*)$ and $(A_1 A_4^*)$. The first one is a transmission grating and the second one is a reflection grating. The remaining ones are $2k$ gratings (i.e. gratings with wavevector $2k$).

A complete treatment of the wave interactions is exceedingly complicated and in general it becomes necessary to resort to numerical solutions. Proper attention then has to be paid to the space charge fields set up by the various interference patterns of different spatial frequency and direction with respect to any applied electric field. Furthermore, the propagation direction, polarization, and wavelength of the beams dictate the effective electro-optic coefficient that they experience. The seminal work in understanding phase conjugation in photorefractive materials was carried out by Cronin-Golomb *et al.* [21], who presented analytical solutions under various approximations, the most notable being the one-grating approximation. It stipulates that although there are in general four gratings, in many situations one grating is dominant.

We shall in the following adopt this approach and assume that only the transmission grating is present. In this case, if absorption and optical activity are neglected, the coupled equations for the amplitudes of the four waves simplify to

$$\frac{dA_1^*}{dz} = -j\kappa E_w g A_2^* \tag{5.18}$$

$$\frac{dA_2}{dz} = j\kappa E_w g A_1 \tag{5.19}$$

$$\frac{dA_3^*}{dz} = j\kappa E_w g A_4^* \tag{5.20}$$

$$\frac{dA_4}{dz} = -j\kappa E_w g A_3 \tag{5.21}$$

$$\text{where } g = \frac{A_1^* A_2 + A_3^* A_4}{I_0}, \qquad \kappa = \frac{\pi r_{eff} n^3}{\lambda \cos\theta}, \tag{5.22}$$

I_0 is the total average light intensity $I_0 = I_1 + I_2 + I_3 + I_4$, θ is the incident angle of beam 1 as shown in Fig. 5.4, and r_{eff} is the effective electro-optic coefficient given by [21]

$$r_{eff} = r_{13} \sin[(\theta + \alpha)/2] \tag{5.23}$$

for mixing beams of ordinary polarization and

$$r_{eff} = \left\{ \begin{matrix} n_e^4 r_{33} \sin\theta \sin\alpha + 2n_e^2 n_o^2 r_{42} \cos^2[(\theta+\alpha)/2] \\ + n_o^4 r_{13} \cos\theta \cos\alpha \end{matrix} \right\} \frac{\sin[(\theta+\alpha)/2]}{n_e n_o^3} \tag{5.24}$$

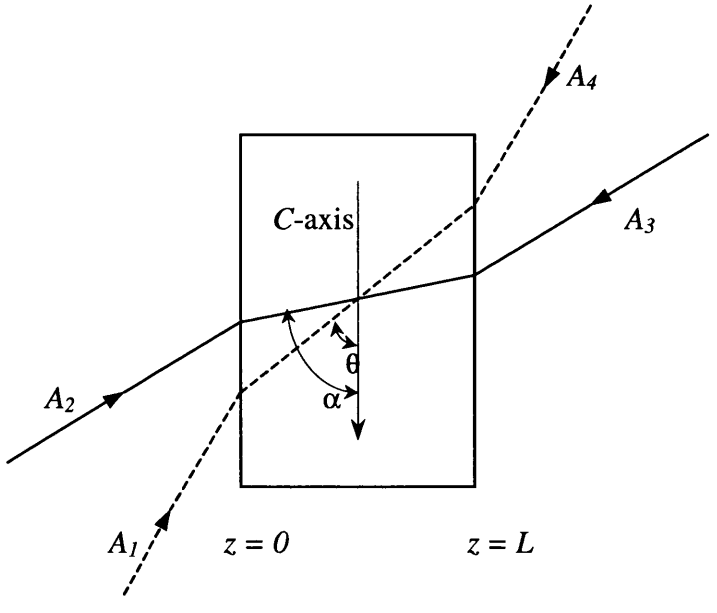

Fig. 5.4 Four-wave mixing arrangement appropriate to phase conjugation showing the pump beams A_2, A_3 (solid) and signal and phase conjugate beams A_1, A_4 (dashed), as well as the relative orientation of the c-axis of the crystal.

for mixing beams of extraordinary polarization, where α is the angle of the pump beams, θ is the angle of the signal and phase conjugate beams, with respect to the optic axis of the crystal. The r_{ij} are the electro-optic coefficients and n_o and n_e are the ordinary and extraordinary refractive indexes, respectively. E_w is the normalized space charge field, i.e.

$$E_w = \frac{iE_d - E_0}{1 + E_d / E_q + iE_0 / E_q} \tag{5.25}$$

where E_0 is the amplitude of the applied field, and E_d, E_q are characteristic fields of the medium as discussed in Chapter 2.

If we further assume that the pump beams are undepleted, i.e. I_2, I_3 >> I_1, I_4. This greatly simplifies the mathematics, while still retaining most of the important features. With A_2 and A_3 being constant, Eqs. (5.18) and (5.21) are readily integrated. For optical phase conjugation via four-wave mixing, the boundary conditions are $A_4(L) = 0$ and $A_1(0)$ is known, the solution for the amplitude of beam 4 and 1 are:

$$A_4(z) = A_1(0)\frac{A_3}{A_2^*}\left[\frac{\exp(-j\kappa E_w(z-L))-1}{r^{-1}\exp(j\kappa E_w L)+1}\right] \tag{5.26}$$

$$A_1(z) = A_1(0)\left[\frac{r^{-1}\exp(-j\kappa E_w(x-L))+1}{r^{-1}\exp(j\kappa E_w L)+1}\right] \tag{5.27}$$

where r is the ratio of the pump intensities I_2 / I_3. These solutions show, first, the amplitude of beam 4 is directly proportional to the phase conjugate amplitude of the beam 1, second, Bragg matching conditions require that if beams 2 and 3 are counterpropagating then so are beams 4 and 1. Taken together, we have that both the phase and direction of propagation of beam 1 have been reversed. In other words, beam 4 is the phase conjugate of beam 1.

The conjugate reflectivity, R_c, defined as the ratio of the intensity of beams 4 and 1 at z = 0, from Eq's (5.26) and (5.27) it is given by [22]

$$R_c = \frac{I_4(0)}{I_1(0)} = r\left|\frac{\exp(j\kappa E_w L)-1}{\exp(j\kappa E_w L)+r}\right|^2 . \tag{5.28}$$

The phase conjugate reflectivity is approximately determined by the intensity independent term κE_w, and the pump ratio r only.

For application as a phase conjugator, it is important that A_2 and A_3 are kept constant throughout the medium. The incident wave A_1 is not, in general, a plane wave. It may consist of many spatial components (or Fourier components). If each of these components is conjugated equally, the result is the generation of the phase-conjugate wave. This requires that each of the Fourier components undergo four-wave mixing individually. Phase conjugation via four-wave mixing requires a pair of counter-

propagating beams (A_2, A_3). The alignment of these two beams to achieve $\boldsymbol{k}_2 + \boldsymbol{k}_3 = 0$ is essential to obtain high-fidelity phase conjugation.

5.2.2 Experimental results and discussions

Fig. 5.5 is the experimental set-up for phase conjugation via four-wave mixing configuration. We use a He-Ne laser (λ = 632.8 nm) as the light source. The $\lambda/2$ half wave plate and the Polarizer are used to adjust the polarization directions of the

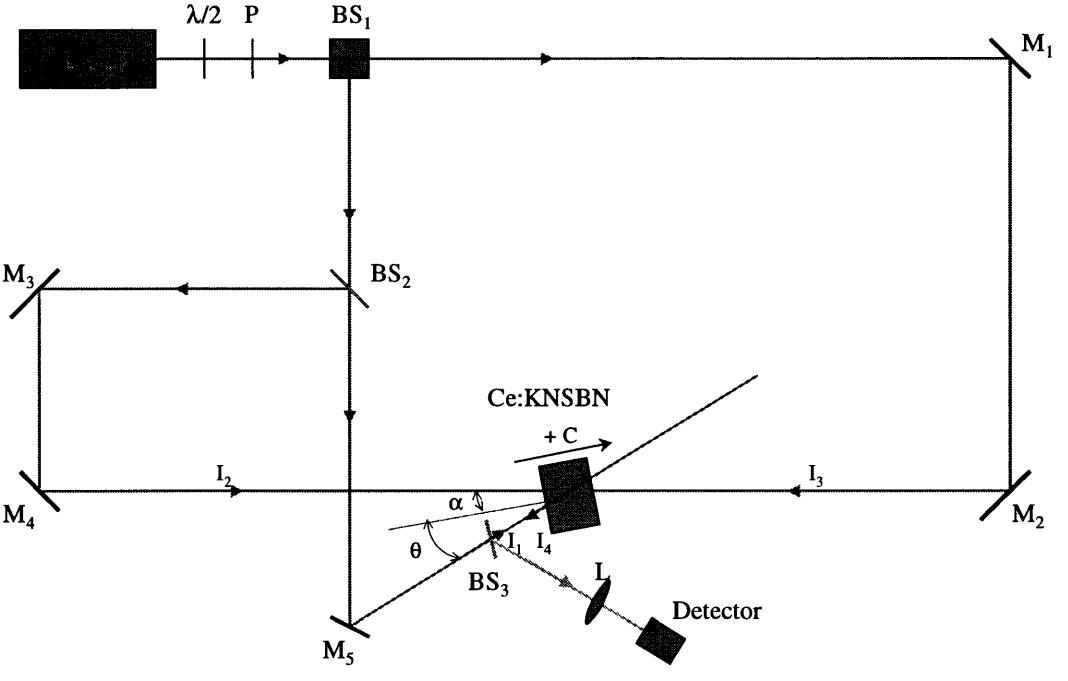

Fig. 5.5 FWM phase conjugation experimental set-up. $\lambda/2$ is a half wave plate; P is a polarizer; M_i are reflective mirrors; BS_i are beam splitters and L is a lens.

extraordinary beam. I_2 and I_3 are the pair of pumping beams, which are aligned carefully to achieve $\boldsymbol{k}_2 + \boldsymbol{k}_3 \rightarrow 0$, and pass through the same distance to reach the Ce:KNSBN crystal. I_1 is the signal beam and I_4 is the generated phase conjugation beam, $\boldsymbol{k}_1 + \boldsymbol{k}_4 = 0$. The phase conjugation beam I_4 is reflected by BS_3 to the detector. The diameters of all the beams are about 2 mm. To avoid collecting the reflected portion of beam I_2, the incident angles of beam I_1 and beam I_2 were chosen to be different, indicated as θ and α in the diagram of the set-up. The c axis of the Ce:KNSBN crystal is in the plane of the paper, and the signal beam entered its negative c face.

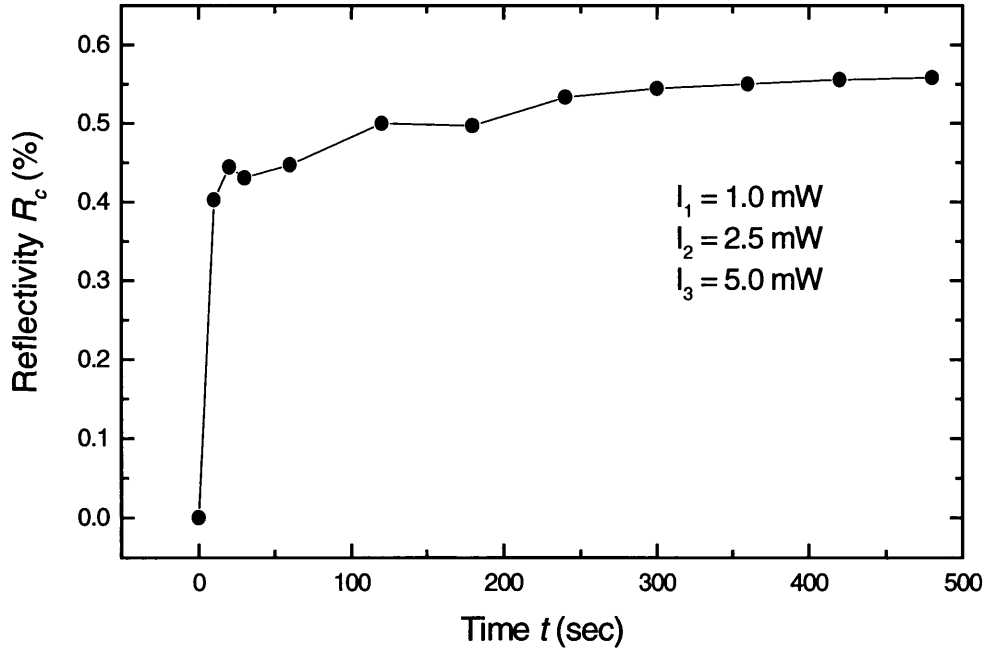

Fig. 5.6 The FWM phase conjugation reflectivity versus the interacted time.

Fig. 5.6 illustrates the time evolution of FWM phase conjugation in Ce:KNSBN crystal. All the beams are extraordinary polarized in the plane of the paper, the incident angles of beam I_1 and beam I_2 are $2\theta = 36.0°$ and $2\alpha = 20.8°$ respectively. The intensities of the pumping beams (I_2, I_3) and signal beam (I_1) are shown in the Fig. 5.6. We found that the phase conjugation reflectivity increased very fast at the beginning, it had 80% of its saturated value in about 30 seconds. The reflectivity reached its saturation in about 300 seconds, the saturated reflectivity was about 0.55% in the above experimental conditions.

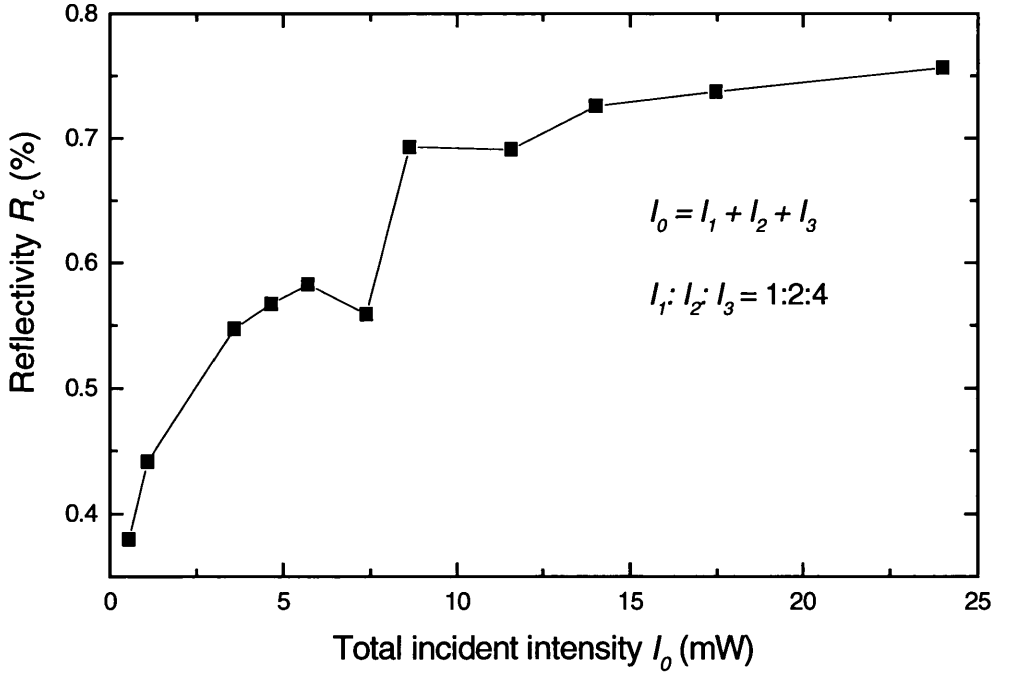

Fig. 5.7 The FWM phase conjugation reflectivity versus total incident intensity

Fig. 5.7 shows the FWM phase conjugation reflectivity versus total incident intensity I_0, where $I_0 = I_1 + I_2 + I_3$. The ratio of their intensities is I_1: I_2: I_3 = 1:2:4. We found that the FWM phase conjugation reflectivity R_c increased with the total incident intensity I_0, especially for lower incident intensity (I_0 < 8mW, in our experiment). According to the FWM phase conjugation reflectivity expression of (5.28), R_c is independent of the incident intensity I_0 (In our case $R_c = I_4/I_1 < 0.8\%$, thus $I_0 = I_1 + I_2 + I_3 + I_4 \approx I_1 + I_2 + I_3$). We think this disagreement is due to the fact that the derivation of the R_c expression is based on some approximations, such as no absorption and undepleted pump beams in the medium. However, for higher incident intensity (I_0 > 14mW, in our experiment), R_c increased very slightly with I_0, and was almost independent on I_0. It seems that the approximate R_c expression is suitable for incident beams with higher intensity.

Fig. 5.8 shows the relations of FWM phase conjugate reflectivity versus pump ratio. The signal beam I_1 and the total incident intensity I_0, $I_0 \approx I_1 + I_2 + I_3$, was kept same in our experiment, the values of I_1 and I_0 were 3.0mW and 18.0mW, respectively. To change the intensities of pump beam 2 and 3 to get different pump ratio, $r = I_2 / I_3$. The results are shown in two pump ratio ranges for $r \leq 0.5$ and $r \geq 0.5$ respectively. We find that the phase conjugate reflectivity (R_c) depending on pump ratio (r) is quite different in the two ranges. For the pump ratio $r \leq 0.5$, the experimental data could be fitted as the function of $y = y_0 + A\exp\left(\frac{x - x_0}{t}\right)$, where y and x stand for the reflectivity and pump ratio, respectively, y_0, x_0, A and t are the fitting parameters shown in the boxes of the top graph in Fig. 5.7. For the pump ratio $r \geq 0.5$, the fitting function is $y = y_0 + A/(x - x_0)$, where

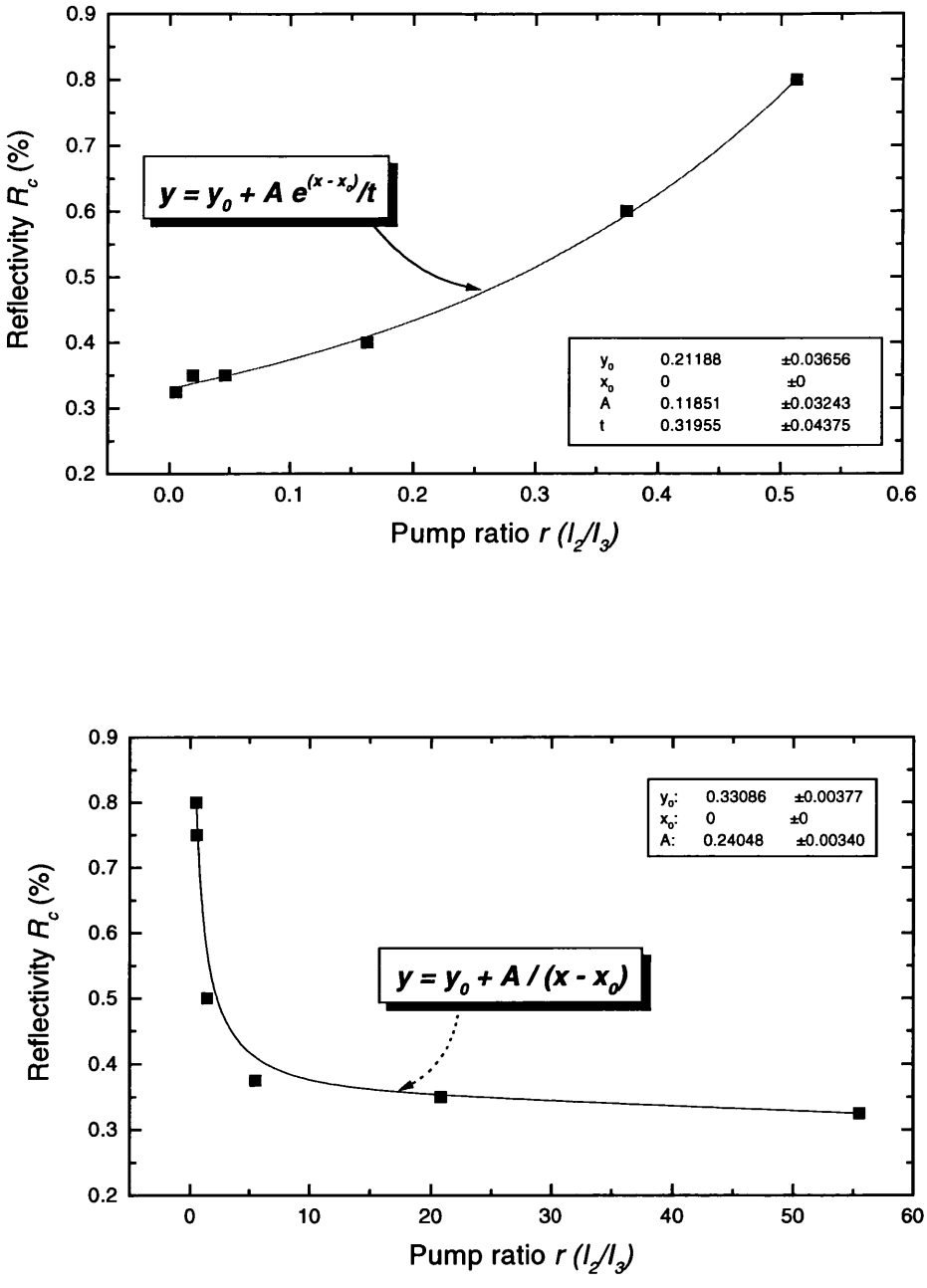

Fig. 5.8 Phase conjugate reflectivity versus pump ratio. The top is for the smaller pump ratio, $r \leq 0.5$. And the bottom is for the larger pump ratio $r \geq 0.5$. The square dots are experimental data, and the curves are the fitting functions. The data in the boxes are the fitting parameters and their relative errors.

y and x stand for the reflectivity and pump ratio as well, y_0, x_0 and A are the fitting parameters shown in the boxes of the bottom in Fig. 5.7.

According to our experimental results and data analysis, the FWM phase conjugate reflectivity R_c increases with the pump ratio r as the exponential function for $r \leq 0.5$, and decays as the inverse function of pump ratio for $r \geq 0.5$. Obviously, there exists a maximum reflectivity $(R_c)_{max}$ related to the optimum pump ratio r_{opt}. In our experiment, the $(R_c)_{max}$ and r_{opt} are 0.8% and 0.5, respectively.

We calculated the phase conjugate reflectivity R_c as the function of pump ratio r, using Eq. (5.28). In the case of pure diffusion with $E_0 = 0$, the normalized space charge field E_w is purely imaginary, which is the function of incident angle of signal beam θ, as discussed in Section 3.5.2. For mixing beams of extraordinary polarization, the effective electro-optic coefficient r_{eff} can be calculated using Eq. (5.24) for the given values of angles α and θ. Using the parameters of Ce:KNSBN mentioned in Section 3.5.1 and our experimental conditions 2θ = 36.0°, 2α = 20.8°, we got $|\kappa E_w L| = 0.394$. Since E_w is purely imaginary, $\exp(j\kappa E_w L)$ = exp(-0.394) = 0.674, from Eq. (5.28), the relation between R_c and r was simplified as

$$R_c(r) = r\left(\frac{0.326}{0.674 + r}\right)^2 \tag{5.29}$$

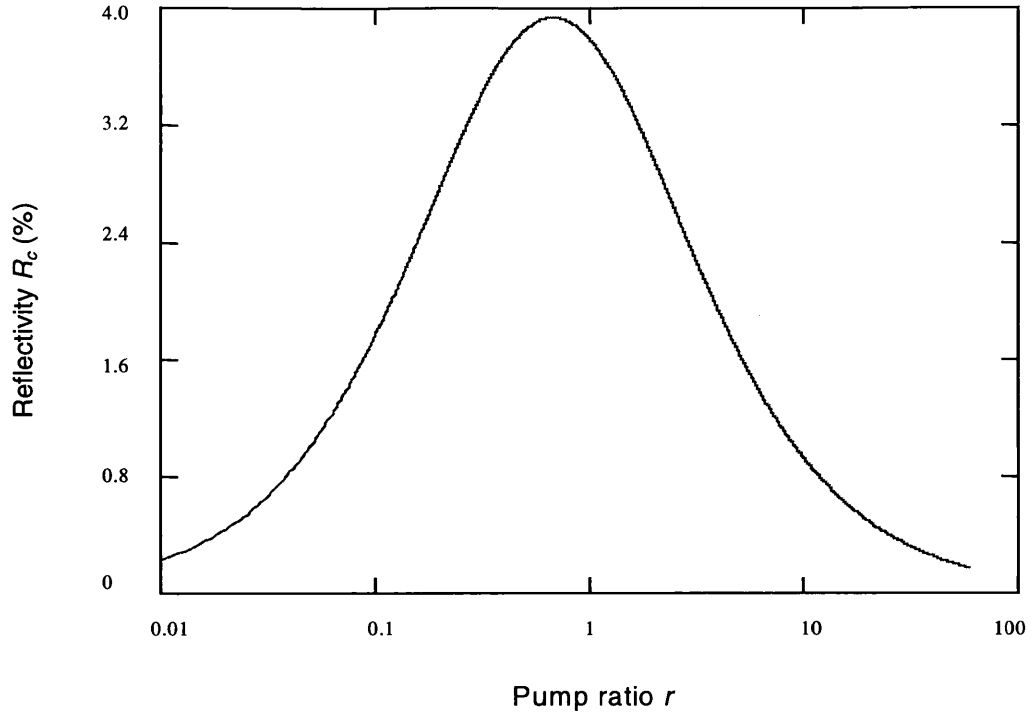

Fig. 5.9 Calculated results of the FWM phase conjugate reflectivity R_c versus the pump ratio r for extraordinary red lights ($\lambda = 632.8$ nm) in the experimental conditions $2\theta = 36.0°$, $2\alpha = 20.8°$ and $E_0 = 0$. The r axis is log scaled.

Fig. 5.9 shows the calculated results in our experimental conditions, to indicate all interested ranges of the pump ratio r, the r axis is log scaled. It is clear that there exists a maximum conjugate reflectivity corresponding to the optimum pump ratio. It is easy, from Eq. (5.29), to get $r_{opt,\ calculated} = 0.674$ and $(R_c)_{max,\ calculated} = 3.94\%$. Our experimental optimum pump ratio $r_{opt} = 0.5$ is near the calculated value 0.674, and our experimental maximum conjugate reflectivity $(R_c)_{max} = 0.8\%$ is about 5 times less than the

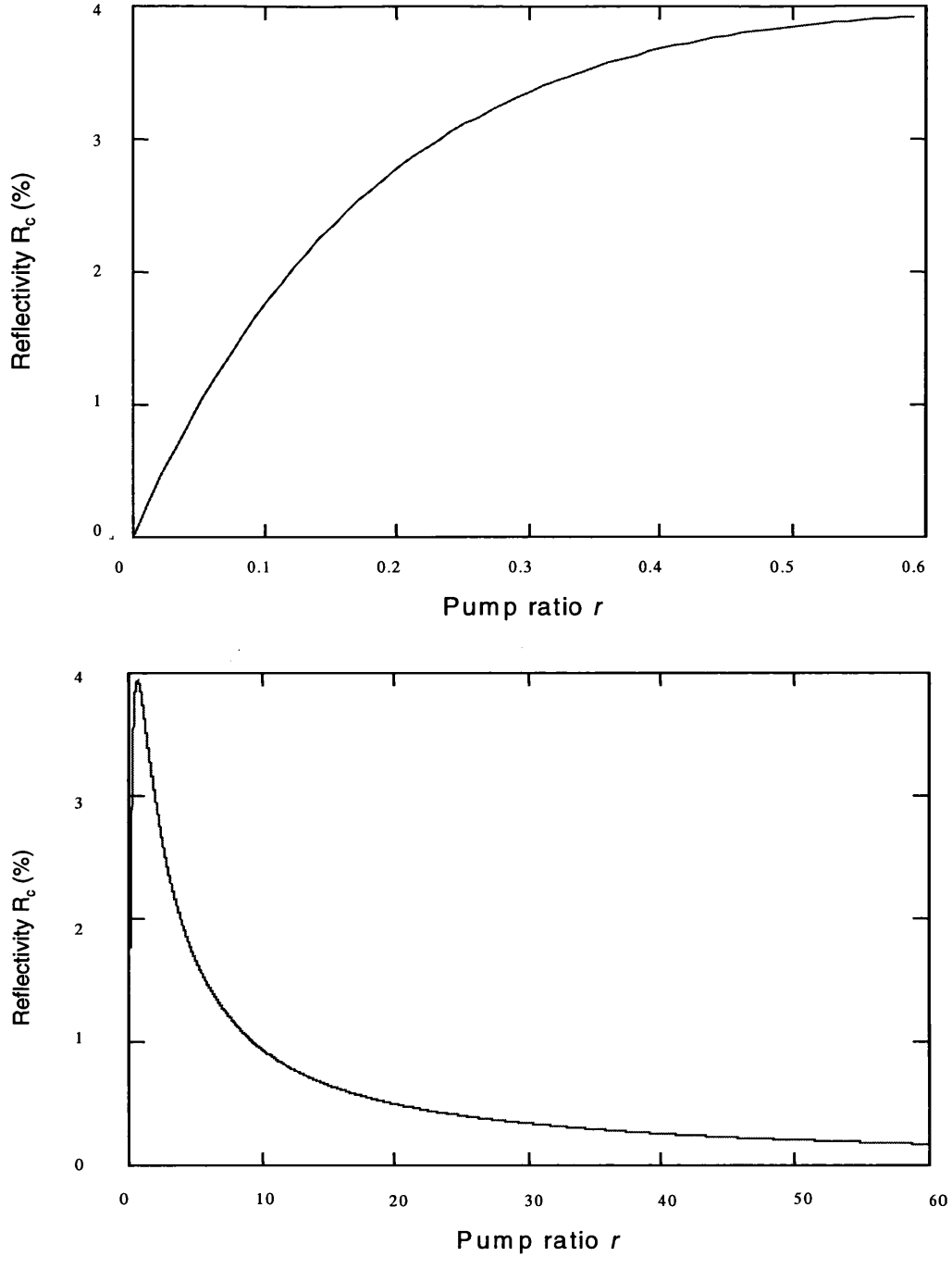

Fig. 5.10 Calculated results of the FWM phase conjugate reflectivity R_c versus the pump ratio r. The top is for smaller pump ratio, $r \leq 0.6$. And the bottom is for larger pump ratio r.

calculated one 3.94%. Our experimental results were acceptable for the calculated ones, if we take into account the following facts: the equations we used are approximate ones and the parameters we chose are the common ones for KNSBN family.

For comparison, we plotted the calculated results of the FWM phase conjugate reflectivity R_c versus the pump ratio r in linear scale as shown in Fig. 5.10. Corresponding to Fig. 5.8, the top is for smaller pump ratio $r \leq 0.6$, and the bottom is for the larger one. For larger pump ratio $r >> 0.674$, from Eq. (5.29), we can derive $R_c(r) \propto (0.326)^2 / r$, i.e. R_c is an inverse function of r, which is the same as our fitting result for experimental data. For smaller pump ratio $r << 0.674$, Eq. (5.29) yields $R_c(r) \propto (0.326/0.674)^2 r$, R_c is a linear function of r. Considering an exponential function will tend to a linear one as its variable becomes small enough, i.e. $y = y_0 + A\exp\left(\frac{x}{t}\right) \propto y_0 + \frac{A}{t}x$, for $\frac{x}{t} << 1$, we conclude that our experimental data fitting result for smaller pump ratio is also agreed with the theoretical calculation.

Fig. 5.11 shows the phase conjugate reflectivity versus incident angle. The sum of pump beam incident angle 2α and signal beam incident angle 2θ kept unchanged in our experiment ($2\alpha + 2\theta \equiv 56.8°$). The incident beam ratios were $I_1 : I_2 : I_3 = 1:2:4$, and the total incident beam intensity was $I_0 \approx I_1 + I_2 + I_3 \approx 14\,\text{mW}$. We find that the FWM phase conjugate reflectivity depends on the pump beam incident angle α, the reflectivity R_c increased from 0.15% to 0.82% when the pump beam angle 2α decreased from 40° to

0°. It should be noted that the sum of pump beam incident angle 2α and signal beam incident angle 2θ remained same in our experiment, the signal beam incident angle increased while the pump beam incident angle decreased. In our experiment, when we removed the pump beams, i.e. to block I_2 and I_3 in Fig. 5.5, there still existed the phase conjugate beam, indicated as self-pump phase conjugation in Fig. 5.11, which also depended on the incident angle. At this time the pumping beams were only fed by internal reflection. This self-pump phase conjugation will be discussed in more detail in the next section.

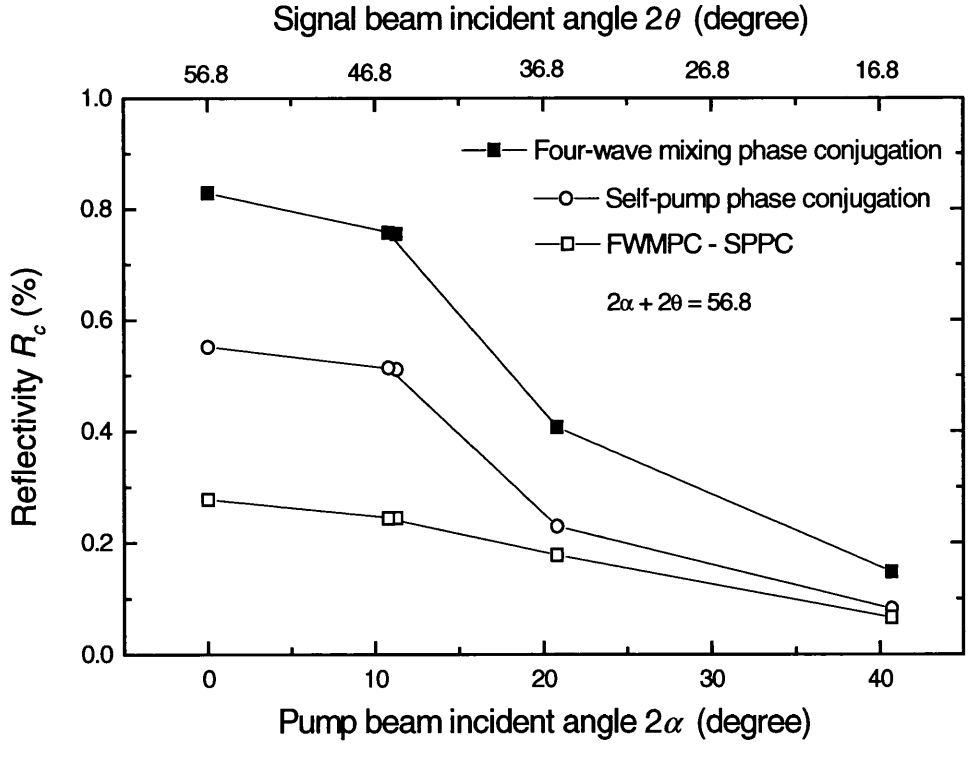

Fig. 5.11 Phase conjugate reflectivity versus incident angle. The sum of pump beam incident angle 2α and signal beam incident angle 2θ, $2\alpha + 2\theta =$ 56.8°, kept unchanged.

From our experimental results as shown in Fig. 5.11, there exist two kinds of pump beams contributing to the phase conjugation in FWM configuration. One is from the external pump beams (I_2 and I_3 in our case), and the other is due to the internal reflection, which generates the so-called "self-pump phase conjugation". The contribution from the internal reflection became the main portion of the phase conjugation when the signal beam incident angle increased. However, the mechanism of FWM phase conjugation is very complicated, it is not the linear addition of the internal reflection contribution and the external pumping one.

5.3 Self-pumped phase conjugation

Phase conjugation via four-wave mixing places a high demand on the quality and alignment of the external pumping beams and the uniformity of the crystal itself. A different class of phase conjugation is the self-pumped phase conjugation (SPPC) that does not need any external pumping beam. In a self-pumped phase conjugation, an incident wave generates its own phase-conjugate wave. Several physical mechanisms can yield self-pumped phase conjugation, such as 1) SPPC with Resonators [23] - [26], 2) SPPC with Stimulated Backward Scattering [27], 3) Ring SPPC [28] and 4) SPPC with semi-resonators [28]. In this section, we only discuss the self-pumped phase conjugate resonators.

Oscillation in photorefractive resonators is known to be sustained by the parametric gain due to two-wave mixing. In the case of a linear resonator (see Fig. 5.2(c)), the oscillation

between the two mirrors provides the counterpropagating beams which are needed in phase conjugation via four-wave mixing. To achieve high fidelity in such a phase conjugator, single mode (spatial mode) oscillation must be maintained in the resonator. It is known that there is a frequency shift associated with a SPPC. Let ω be the frequency of the incident beam. The frequency of oscillation in the resonator is determined by the cavity length. Let $\omega + \delta$ be the frequency of the oscillation. The phase-conjugate wave is shifted in frequency by 2δ.

SPPC can also be achieved by using bi-directional oscillation in ring resonators. We consider a ring resonator in which gains for bi-directional oscillation are provided. The oppositely directed oscillating beams in the ring resonator provide the pumping needed in four-wave mixing. The process thus leads to self-pumped phase conjugation. Self-pumped conjugation can occur in a single cube of photorefractive crystal under the appropriate conditions. As indicated in Fig. 5.2(d), crystal surfaces provide the mirror reflection needed in bi-directional ring oscillation. In fact, total internal reflections occur in many of the oscillations. With an index of refraction around $n = 2.5$, the incident angle for total internal reflection is $\theta > 21.8°$. Thus ring oscillations in the photorefractive crystal cubes involve total internal reflections. These internal ring oscillations suffer loss due only to material absorption and scattering. The frequency of oscillation of these resonators can be shifted relative to that of the pump beam. This leads to a small frequency shift in the phase conjugate wave.

5.3.1 Theory of SPPC with two coupled interaction regions

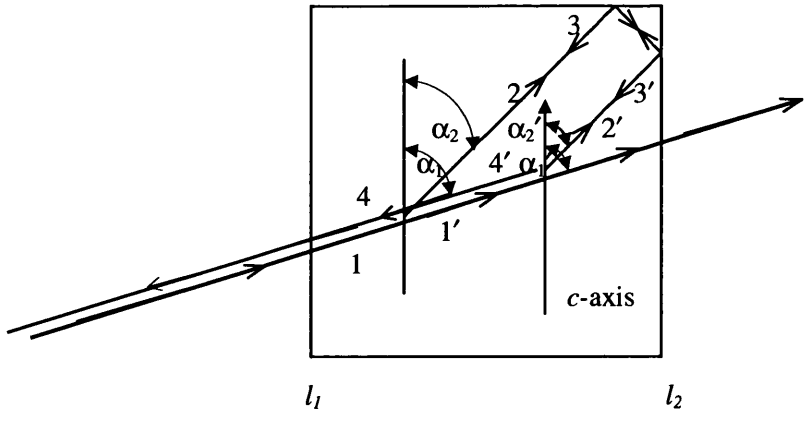

Fig. 5.12 Phase conjugator with two interaction regions coupled by internal reflection

Figure 5.12 shows schematically the orientation of the beams in the self-pumped phase conjugator described in last section. There are two interaction regions. In each interaction region, there are four beams: an input beam and its phase-conjugate and two beams that serve as pumping beams. Both interaction regions contribute to the phase-conjugate output 4′- 4. The outgoing pumping beam from one interaction region is reflected into the other interaction region by either an external mirror or a corner-cube reflector or by two internal reflections at two adjacent crystal faces. If the corner of the crystal is not a right angle ($\alpha_2 \neq \alpha_2'$), the device still works, even though the coupling strengths in the two interaction regions are different. The first interaction region (nearer the left of Fig.5.12) extends from z = l_1 to z = l_2, the second from l_1' to l_2'. (We consistently prime all

quantities that refer to the second interaction region). The only geometric restriction on our results is that the interaction regions do not overlap.

The boundary conditions are

$$A_1'(l_2') = 0 \qquad \text{(no input phase-conjugate wave)} \tag{5.30}$$

$$\left.\begin{aligned} A_2'(l_1) &= 0 \\ A_2'(l_1') &= 0 \end{aligned}\right\} \qquad \text{(no input pumping beams)} \tag{5.31}$$

$$\left.\begin{aligned} A_3(l_2) &= (1-L)^{1/2} e^{i\theta} A_2'(l_2') \\ A_3'(l_2') &= (1-L)^{1/2} e^{i\theta} A_2(l_2) \end{aligned}\right\} \text{(reflection connecting the two interaction regions)} \tag{5.32}$$

$$\left.\begin{aligned} A_4(l_2) &= e^{i\phi} A_4'(l_1') \\ A_1'(l_2) &= e^{i\phi} A_4(l_1) \end{aligned}\right\} \qquad \text{(continuity)} \tag{5.33}$$

where L is the intensity lost by a pumping beam in reflection and θ and ϕ are phases accumulated by the beams in going from one interaction region to the other.

It is possible to show [29] that the coupled equations for the amplitudes of the four waves (Eqs.(5.18) – (5.22)) conserve the following quantities

$$|A_1|^2 + |A_2|^2 = c_1 \tag{5.34}$$

$$|A_3|^2 + |A_4|^2 = c_2 \tag{5.35}$$

$$A_1 A_4 + A_2 A_3 = c \tag{5.36}$$

where c_1, c_2 and c are constants of integration. Equations (5.34) and (5.35) are results of conservation of energy, whereas (5.36) is a direct consequence of reciprocity theorem. The quantities conserved in the two interaction regions are related by

$$c = 2c' \tag{5.37}$$

$$c_1 = c_1' + c_2' /(1-L) \tag{5.38}$$

Normalizing the intensities so that $I_0 = 1$ and combining Equations above, we obtain the solution (see the Ref.[29])

$$\tanh\left(\frac{\gamma l'}{2}\xi\right) = \xi \tag{5.39}$$

and

$$\left[(1+\xi)\frac{a(r)}{b(r)} + (1-\xi)(1-L)\right]\left[(1+\xi)(1-L)\frac{b(r)}{a(r)} + (1-\xi)\right]$$

$$= \frac{4\left[r - \tanh\left(\frac{\gamma l}{2}r\right)\right]^2}{(1-r^2)\tanh^2\left(\frac{\gamma l}{2}r\right)} \tag{5.40}$$

$$R_c \equiv \left|\frac{A_4(l_1)}{A_1^*(l_1)}\right|^2 = \frac{-a(r)b(r)}{4(1-r^2)\tanh^4\left(\frac{\gamma l}{2}r\right)} \tag{5.41}$$

where

$$a(r)=r^2\left[1-\tanh^2\left(\frac{\gamma l}{2}r\right)\right] \tag{5.42}$$

$$b(r)=\left[r-2\tanh\left(\frac{\gamma l}{2}r\right)\right]^2-r^2\tanh^2\left(\frac{\gamma l}{2}r\right) \tag{5.43}$$

$\gamma \equiv \gamma(\alpha_2)$, $\gamma' \equiv \gamma(\alpha_2')$, γ is the coupling coefficient in unit length (mm^{-1}). $l = l_2 - l_1$, $l' = l_2' - l_1'$. R_c is the phase conjugate reflectivity.

In principle, for a given coupling strength $\gamma l'$, Eq.(5.39) is solved iteratively for ξ. For given γl and L, r can be solved numerically.

5.3.2 SPPC experimental results and discussions

The experimental setup for measuring the SPPC reflectivity is shown schematically in Figure 5.13. We use an Innova 90 Laser (λ = 514 nm) and a He-Ne laser (λ = 632.8 nm) as the light sources. The $\lambda/2$ half wave plate and the Polarizer are used to adjust the polarization directions of the extraordinary beams. When we use the ordinary beams, the $\lambda/2$ half wave plate and the Polarizer will be taken away. The neutral density filter is used to change the intensity of the incident beams (When we used the Innova 90 Laser, we moved the neutral filter to the front of D_2 for protecting the detector. The intensity of

output from the Innova 90 laser can be adjusted manually). The lens $L_1(f = 450$ cm) is used to slightly adjust the beam diameter incident on the Ce:KNSBN crystal (in our experiment, the beam diameter is about 1 mm). The beam-splitter reflects part of incident beam to D_2, which monitors the incident intensity (I_{in}), and reflects the phase conjugation beam (I_c) to detector D_1. And L_2 focuses the SPPC beam to D_1. The c axis of the crystal is in the plane of the paper. θ is the angle between the incident beam and the c axis of the crystal, which has the same value of α_1 as shown in Fig. 5.12.

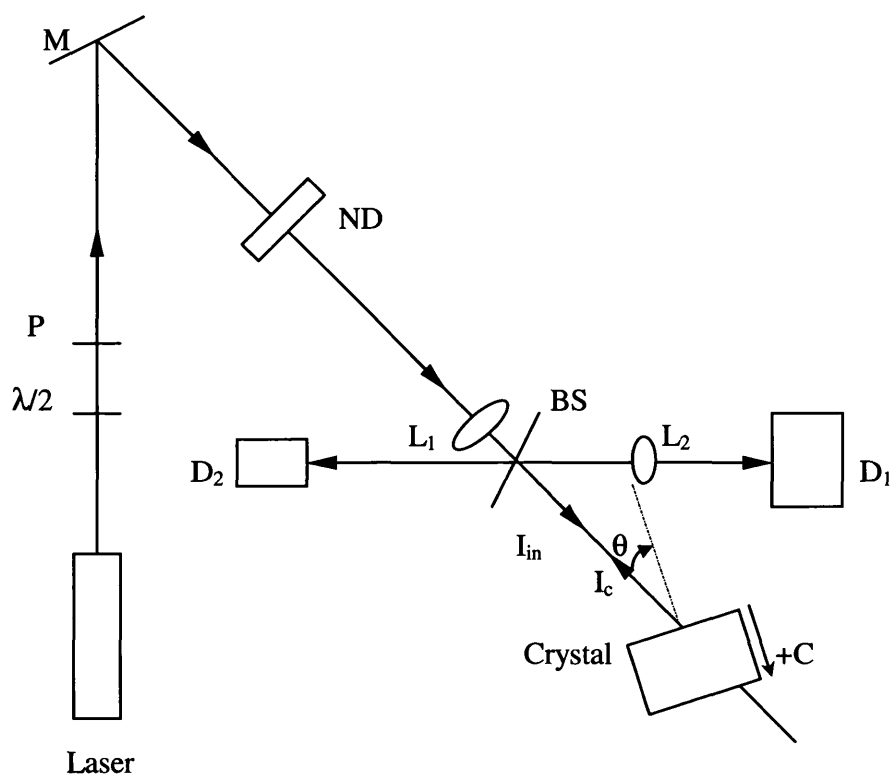

Fig. 5.13 Schematic diagram of the experimental arrangement for SPPC measurement. λ/2: half wave plate; P: polarizer; M: mirror; ND: neutral density filter; L_1, L_2: lens; BS: beam splitter and D_1, D_2: detectors.

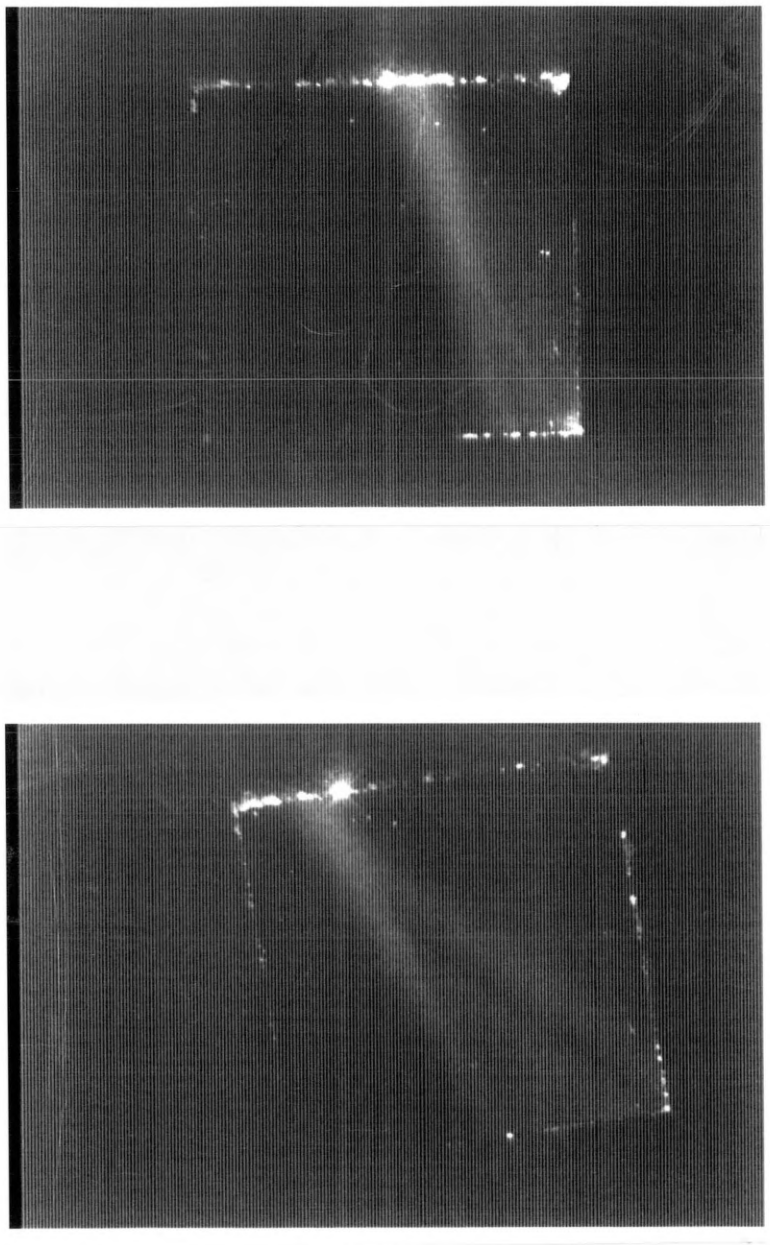

Fig. 5.14 Two photographs of the Ce:KNSBN crystal. In the photographs, the extraordinary ray (λ = 514 nm) enters the top face of the crystal, with different incident angles with the c axis of the crystal. There exist loops between the incident beam and the lower-right-hand edge of the crystal.

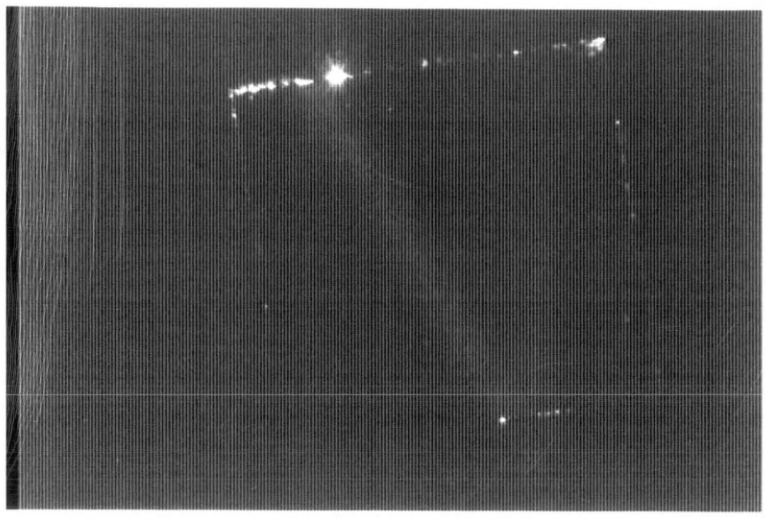

Fig. 5.15 The photograph of the Ce:KNSBN crystal, with ordinary ray ($\lambda = 514$ nm) entering the top face of the crystal. There is no loop between the incident beam and the edge of the crystal.

Figure 5.14 is the photograph of the device in operation. The incident beam ($\lambda = 514$ nm) enters the crystal as an extraordinary ray, which is polarized in the plane of the paper. By the photorefractive effect, this beam suffers asymmetric self-defocusing in the plane formed by the incident beam and the c axis of the crystal, creating a fan of light that illuminates one of the edges of the crystal [30]. This edge acts as a two-dimensional corner-cube reflector and, by two internal reflections, directs the fan of light back toward the incident beam. Referred to Figure 5.12, our result shows that the fan actually collapses into at least two narrow beams. It is speculated that each beam is composed of a pair of counterpropagating beams, so there are two counterpropagating loops of light in

the crystal. Each pair of counterpropagating beams mixes, by the photorefractive effect, with the incident beam 1 to create the phase conjugate beam 4. The phase conjugate beam leaves the crystal exactly back along the direction of the incident beam. Note that beams 1 and 4 can also act as pumping beams and create gain for the loop beams, which then create gain for the conjugate pair (1 and 4), so the process bootstraps.

Figure 5.15 is the photograph of the Ce:KNSBN crystal, with ordinary ray entering the crystal. No loop is found between the incident beam and the edge of the crystal. According to the SPPC theory we discussed above, the generation of phase-conjugate wave is mainly depended on the coupling strength. Comparing to the extraordinary ray (the polarization direction is in the same plane of the crystal *c* axis), the coupling strength is considerably less for ordinary rays [31].

We also used the He-Ne laser (λ = 632.8 nm) as the light sources in our experiment and found that there exist similar phenomena as shown in Figures 5.14 – 5.15, i.e. there are counterpropagating loops of light in the crystal for the extraordinary incident beam, and no loop forms for the ordinary one.

Figure 5.16 is the SPPC reflectivity versus the incident angle with extraordinary incident beams, i.e. the extraordinary polarization is in the same plane of the *c* axis of the crystal. The top graph is for the Innova 90 laser (λ = 514 nm), and the bottom one is for the He-Ne laser (λ = 632.8 nm). For both incident beams, the same phenomena as other tungsten-bronze crystals of point group 4 mm are observed:

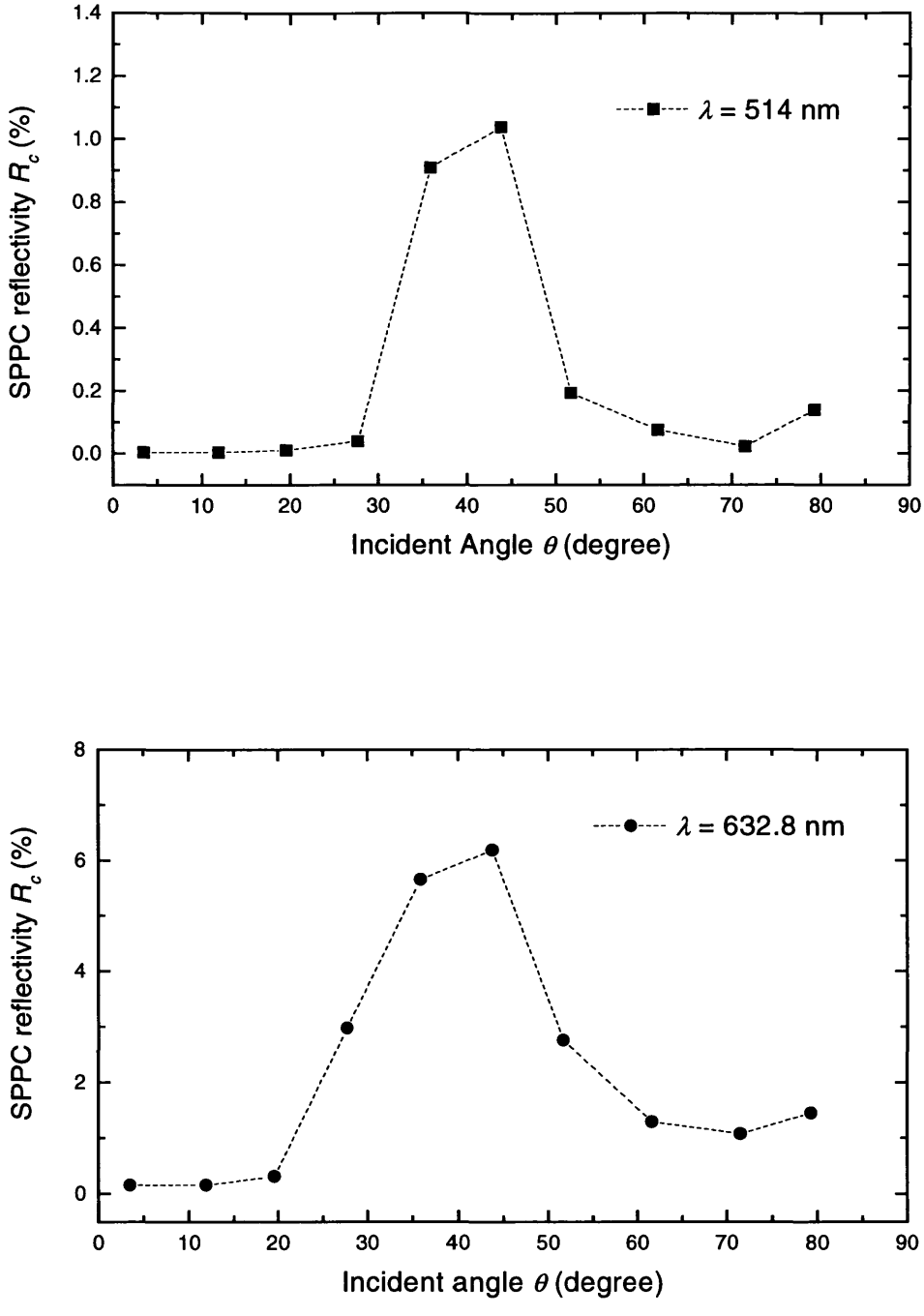

Fig. 5.16 SPPC reflectivity versus the incident angle with extraordinary incident beams. The top graph is for the Innova 90 laser (λ = 514 nm), and the bottom one is for the He-Ne laser (λ = 632.8 nm).

a) There exists a threshold of incident angle for generating SPPC. For the Innova 90 laser (λ = 514 nm), only if the incident angle $\theta > 27°$, SPPC reflections could be achieved, i.e. its threshold of incident angle is 27° for green light. For the He-Ne laser (λ = 632.8 nm), the incident angle is about 20°. (According to [32], with an index of refraction around $n = 2.5$, the incident angle for total internal reflection is $\theta > 21.8°$. For the KNSBN crystal, the index for extraordinary ray is $n_e = 2.30$).

b) There exists an optimal incident angle $\theta_{opt} \sim 43°$ for both incident beams. The SPPC reflectivity reaches its maximum when $\theta = \theta_{opt}$.

c) The SPPC reflectivity versus the incident angle is almost symmetrical to the optimal incident angle θ_{opt}. (The slight asymmetry is due to the changing of the effective diameter of incident beam, while the incident angle increases, the effective diameter will become larger).

Besides the different threshold of incident angles mentioned, the SPPC reflectivity generated by the red light is much higher, by as much as a factor of 6, than that by the green one. In general, for the red light, most photorefractive materials do not have a relative high phase conjugation reflectivity [33] – [35]. However, S. Bian *et. al.*[36] obtained, to our knowledge, the highest SPPC reflectivity of 84.3% from a 18°-cut Ce:KNSBN crystal at a 632.8 nm wavelength. Ce:KNSBN crystals have the specification that phase conjugation is more easily produced by red light.

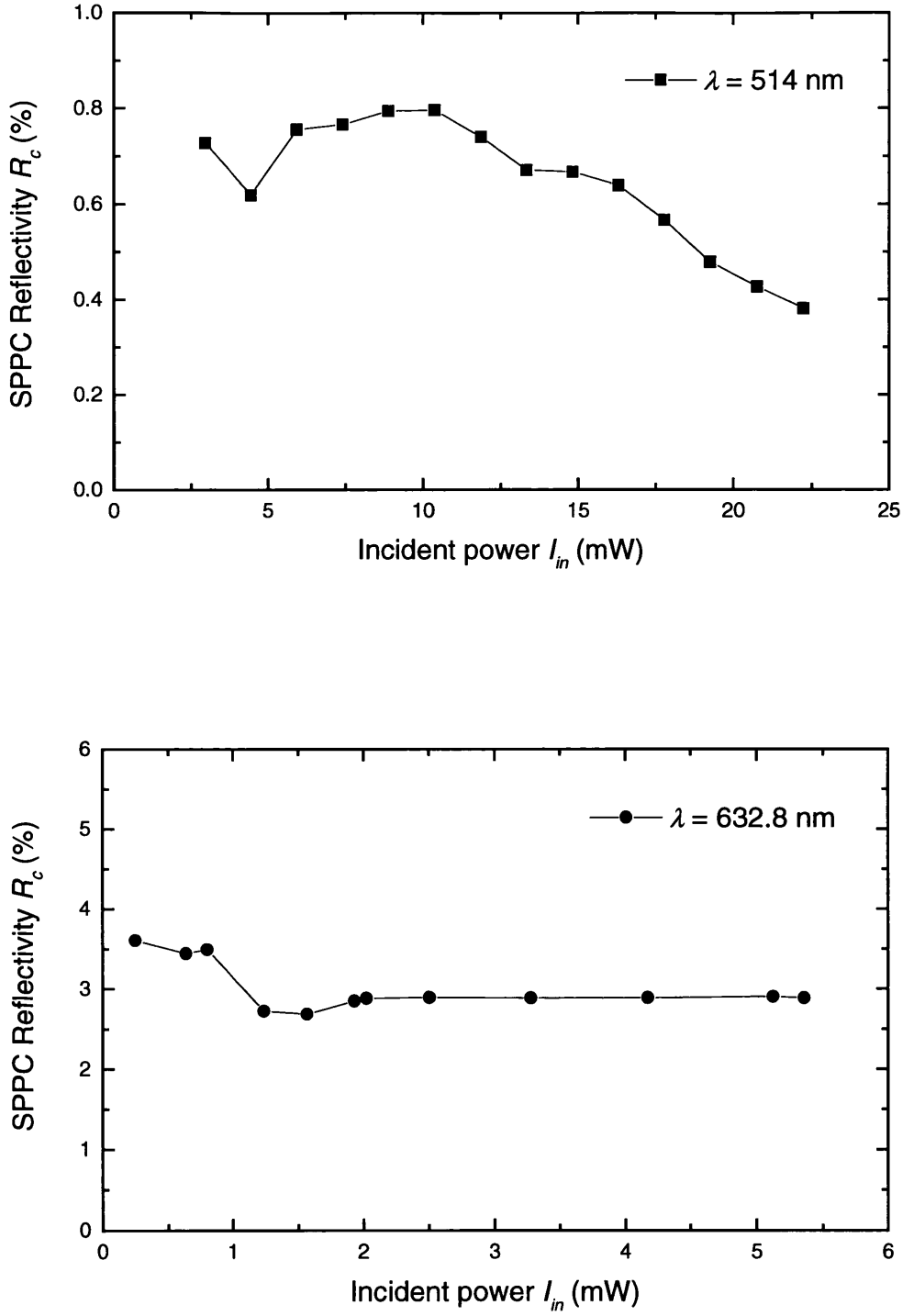

Fig. 5.17 SPPC reflectivity versus the power of incident beams (θ = 43.8°)

Figure 5.17 is the SPPC reflectivity versus the power of different incident beams at incident angle $\theta = 43.8°$. The top graph is for the Innova 90 laser ($\lambda = 514$ nm), and the bottom one is for the He-Ne laser ($\lambda = 632.8$ nm). We found that, for the extraordinary green light ray, which polarization direction is in the same plane of the c axis of the crystal, the SPPC reflectivity begins to drop when the incident power is larger than 10 mW. However, according to the SPPC theory we mentioned, the reflectivity is independent on the incident beam intensity. S. X. Dou *et al* also observed, for the first time to their knowledge, that the reflectivity of SPPC remains almost constant at low power and begins to drop above a certain power in their experiment using Cu:KNSBN crystal [37]. At present we found no obvious explanation to this phenomenon. There are two possibilities:

1) Absorption-induced thermal effects — the local temperature in the crystal will rise due to absorption [38]. This may cause a decrease of the beam coupling as in the case of SBN due to increased dark-conductivity at elevated temperature [39,40]. It may also cause spatial self-phase modulation [41].
2) Intensity dependent deep- and shallow-trap effect and electron-hole competition. However, in these cases, the beam coupling usually rises, reaches a peak, and then decreases when the intensity increases [42].

For the red light of $\lambda = 632.8$ nm, in the incident power regions in our experiment, the SPPC reflectivity is almost constant (for the incident power less than 1mW, the fluctuation of the output from the He-Ne laser may cause some deviation in the results).

Due to limitation of the power output of our He-Ne laser, for red light we could not get the same power range as that of green light, and compare the results in the same condition.

5.4 Conclusions

In the four-wave mixing configuration, we demonstrated the phase conjugate properties for Ce:KNSBN crystal by extraordinary He-Ne laser light (λ = 632.8 nm). Although the interaction mechanism of FWM phase conjugate is exceedingly complicated, we find that for higher incident intensity (the total incident intensity I_0 > 14mW, in our experiment), the experimental results of the phase conjugate reflectivity are almost agreed with the theoretical expression based on the one-grating approximation.

The self-pumped phase conjugation (SPPC) phenomenon has been observed and researched extensively in photorefractive crystals for two decades. Most photorefractive materials require argon-ion laser light (λ = 514.5 nm), which is expensive and inconvenient in applications. However, for the Ce-doped KNSBN crystal in our experiment with the CAT conjugator, we found that a He-Ne laser light (λ = 632.8 nm) can generate higher SPPC reflectivity than that by argon-ion laser (by as much as a factor of 6), with a relative low threshold of incident angle. For both wavelengths, the SPPC generated by extraordinary ray with its polarization in the same plane of the c axis of the crystal is sensitive to the incident angle, and there exist an optimum angle, to which the SPPC reflectivity is almost symmetrical. In our experiment, for the extraordinary

polarised argon-ion laser light (λ = 514.5 nm), the SPPC reflectivity begins to drop when the incident power is larger than 10 mW. This unusual power dependence of photorefractivity of the crystal implies that certain effects begin to appear or play an important role in the crystal at high intensity and further research on its nature may be useful to understand the mechanism of the photorefractive effect in Ce:KNSBN crystal.

Chapter 5: Reference

1. A. Yariv and P. Yeh, Optical Waves in Crystals. New York: Woley, 1984,ch.13.
2. R. A. Fisher, Ed., Optical Phase Conjugation. New York: Academic; b. Ya. Zel'dovich, N. F. Pilepetsky, and V. v. Shkunov, Principles of Phase conjugation. New York: Springer-Verlag, 1985.
3. D. M. Pepper, "Nonlinear optical phase conjugation," in Laser Handbook, M. L. Stich and M. Bass, Eds. Amsterdam, The Netherlands: North-Holland, 1985, vol. 4, pp. 333-485.
4. A. Yariv, "Phase conjugate optics and real-time holography," IEEE J. Quantum Electron, vol. QE-14, pp. 650-66-, 1978.
5. A. Yariv, "Transmission and recovery of three-dimensional images in optical waveguides," J. Opt. Soc. Amer., vol. 66, pp. 301-312,1976.

6. P. Beckwith, I. McMichael, and P. Yeh, "Image destortion in multimode fibers and restoration by polarization-preserving phase conjugation," Opt. Lett., vol. 12, pp. 510-512, 1987.

7. A. E. T. Chiou, P. Yeh, and M. Khoshnevisan, "Coherent image subtraction using phase-conjugate interferometry," in Nonlinear Optics and Applications, Pochi Yeh, Ed., SPIE, vol. 613, pp. 201-206, 1986.

8. A. E. T. Chiou and P. Yeh, "Parallel image srbtraction using phase-conjugate Michelson Interferometer," Opt. Lett., vol. 11, pp. 306-308, 1986.

9. S. K. Kwong, G.A. Rakuljic and A. Yariv, "Real time image subtraction and "XOR" operation using a self-pumped phase conjugate mirror", Appl. Phys. Lett., vol. 48, pp201-203, 1986

10. P. Yeh, I. McMichael, and M. Khoshnevisan, "Phase-conjugate fiber optic gyros," J. Opt. Soc. Amer., vol. 13, pp. 67-68, 1985.

11. P. Yeh, M. Khoshnevisan, M. D. Ewbank, and J. Tracy, "Possibility of relatibe position sensing by using double-phase conjugate resonators," Opt. Comm. Vol. 57, pp. 387-391, 1986.

12. P. Yeh, I. McMichael, and M. Khoshnevisan, "A phase-conjugate fiber optic gyro," Appl. Opt. Vol. 25, 1029-1031, 1986.

13. I. McMichael and P. Yeh, "Self-pumped phase conjugate fiber-optic gyre," Opt. Lett., vol. 11, pp. 686-688, 1986.

14. I. McMichael, P. Beckwith, and P. Yeh, "Phase-conjugate multimode fiber gyro," Opt. Lett., vol. 12, pp. 1023-1025, 1987.

15. D. Pepper, "Applications of optical phase conjugation," Sci. Amer., vol. 254, p. 74, 1986.

16. C. R. Giuliano, "Applications of optical phase conjugation," Phys. Today, pp. 27-35, Apr. 1981.

17. A. Yariv and D. M. Peper, "Amplified reflection, phase conjugation and oscillation in degenerate four-wave mixing", Opt. Lett., vol. 1, pp. 16-18, 1977

18. J. P. Huignard, J. P. Jerriau, P. Auborug and E. spitz, "Phase-conjugate wavefront generation via real-time holography in BSO crtstals", Opt. Lett., vol 4, pp. 21-23, 1979

19. J. Feinberg, D. Heiman, a. r. Tanguay, Jr., and R. W. Hellwarth, "Photorefractive effects and light induced charge migration in burium titanate", J. Appl. Phys., vol. 51, pp. 1297-1305, 1980

20. B. Fischer, M. Cronin-Golomb, J. O. White, A. Yariv and R. Neurgaonkar, "Amplifying continuous wave phase conjugate mirror with strontium barium niobate", Appl. Phys. Lett., vol. 40. pp. 863-865, 1982

21. M. C. Golomb, B. Fischer, J. O. White and A. Yariv, "Theory and applications of four-wave mixing in photorefractive media", IEEE J. Quantum Electron, vol. QE-20, pp.12-30, 1984

22. L. Solymar, D. J. Webb and A. Grunnet-Jepsen, "The physics and applications of photorefractive materials", Oxford University Press, Oxford, p258, 1996

23. J. O. White, M. Cronin-Golomb, B. Fischer, and A. Yariv, "Coherent oscillation by self-induced gratings in photorefractive crystals," Appl. Phys. Lett., vol. 40, pp450-452, 1982

24. P. Yeh, "Theory of unidirectional photorefractive resonators", J. Opt. Soc. Amer. B, vol. 2, pp1924-1928, 1985

25. M. D. Ewbank and P. Yeh, "Frequency shift and cavity length in photorefractive resonators", Opt. Lett., vol. 10, pp496-498, 1985

26. J. Feinberg, "Self-pumped continuous-wave phase conjugator using internal reflection", Opt. Lett., vol. 7, pp. 386-388, 19

27. T.Y. Chang and R.W. Hellwarth, "Optical phase conjugation by backscattering in the photorefractive crystal barium titanate", Opt. Lett., vol. 10, pp408-410, 1985

28. M. C. Golomb, B. Fischer, J. O. White and A. Yariv, "Theory and applications of four-wave mixing in photorefractive media", IEEE J. Quantum Electron, vol. QE-20, pp.12-30, 1984

29. M. C. Golomb, J. O. White B. Fischer, and A. Yariv, "Exact solution of a nonlinear model of four-wave mixing and phase conjugation", Opt. Lett., vol.7, pp.313-315, 1982

30. J. Feinberg, "Asymmetric self-defocusing of an optical beam from the photorefractive effect", J. Opt. Soc. Am. 72, p46, 1982

31. K. R. MacDonald and J. Feinberg, "Theory of a self-pumped phase conjugator with two coupled interaction regions", J. Opt. Soc. Amer, vol. 73, No. 5, pp548-553, 1983

32. P. Yeh, "Photorefractive phase conjugators", Proceedings of the IEEE, vol. 80, No. 3, pp436-450, 1992

33. S.R. Montgomery, J. Y. Rice, D. O. Pederson, G. J. Salamo, M. J. Miller, W. W. Clark II, G. L. Wood, E. J. Sharp and R. R. Neurgaonkar, J. Opt. Soc. Am. B, vol. 5, p.1775, 1988

34. X. Lu, X. Yue, Y. Song, D. Sun, Q. Jiang, Z. Shao and H. Chen, Acta Opt. Sinica, vol. 12, p228, 1992

35. X. Yue, X. Lu, Y. Song, Z. Shao, D. Sun, Q. Jiang and H. Chen, App;. Phys. B, vol. 53, p319, 1991

36. S. Bian, J. Zhang, X. Su, K. Xu, W. Sun, Q. jiang, H. Chen and D. Sun, "Self-pumped phase conjugation of 18°-cut Ce doped KNSBN crystal at 632.8 nm", Opt. Lett., vol. 18, No. 10, pp769-771, 1993

37. S. X. Dou, Y. Ding, H. J. Eichler, P. X. Ye, X. L. Lu and H. C. Chen, "Anomalous power dependence of reflectivity and response time of KNSBN:Cu self-pumped phase conjugators", Opt. Comm., vol. 145, pp166-170, 1998

38. D. W. Rush, B. M. Dugan and G. L. Burdg, Opt. Lett., vol. 16, pp1295-1297, 1991

39. K. Sayano. G. A. Rakuljic, A. Agranat, A. Yariv and R. R. Neurgaonkar, Opt. Lett., vol. 14, p459, 1989

40. D. Rytz, B. A. Wecjsler, R. N. Schwartz, C. C. Nelson, C. D. Brandle, A. J. Brandle, A. J. Valentino, and G. W. Berkstresser, J. Appl. Phys., vol. 66, p1920, 1989

41. M. Horowitz, R. Daisy, O. Werner and B. Fischer, Opt. Lett., vol. 17, p475, 1992

42. Y. Li, D. Sun, K. Xu and F. Hou, Proc. SPIE, vol. 2896, p179, 1996

Chapter 6 Enhancement of Self-Pumped Phase Conjugation by Doppler frequency detuning

6.1 Introduction

MacDonald and Feinberg have suggested [1] that the photorefrative gratings in self-pumped conjugators could translate (and therefore shift the frequency of the diffracted beams) in order to increase their four-wave mixing efficiency. The enhancement is a fundamental property of the four-wave mixing process and occurs under fairly general conditions when the nonlinear interaction is strong, as is certainly the case in self-pumped conjugators. To see how a frequency shift can increase the four-wave mixing efficiency, assume first that the two beams writing the photorefractive grating have the same frequency. The two-wave mixing interaction causes a net transfer of energy from one beam to the other. In materials such as barium titanate, this interaction can be so strong that the energy transfer is nearly total in a distance that is short compared to the width of the amplified beam. The ability of a grating to scatter a third (reading) beam to form a phase-conjugate wave by four-wave mixing (the grating's "diffraction efficiency") depends, at each point, on the relative intensities of the writing beams (through the modulation of their interference fringes). The rapid depletion with distance of one of the writing beams by two-wave mixing results in a small average fringe modulation and a corresponding small diffraction efficiency.

Introducing a small frequency shift into one of the writing beams changes the phase relationship between the interference fringes and the refractive-index variation [2] and reduces two-beam coupling. By thus reducing the depletion of the writing beam, the average modulation of the fringes, and hence the diffraction efficiency of the grating, increases. (Note, however, that too large a frequency shift simply washes out the grating).

A plane-wave calculation of the diffraction efficiency as a function of frequency shift shows that under general conditions, the maximum four-wave diffraction efficiency occurs at two nonzero values of the frequency shift. The enhancement occurs whenever the average amplitude of the grating is small due to depletion of the probe beam by energy coupling. The experimental dependence of the four-wave mixing efficiency on the frequency shift between two writing beams is in qualitative agreement with the theory for the photorefractive crystal $BaTiO_3$ [1]: two maxima of the diffraction efficiency occur at nonzero values of the frequency shift.

For the self-pumped phase conjugation configuration (CAT conjugator) as we discussed in section 5.3, the well-accepted plane-wave mode [3] does not allow frequency shifts. In this theory of SPPC with two coupled interaction regions, although the contribution to the phase-conjugate output is based on four-wave mixing mechanism, the two pumping beams are generated by the internal reflection in the crystal. However, in our experiments with the Ce:KNSBN CAT conjugator, we are first to find (to our knowledge) that the Doppler frequency detuning of input beam could enhance the phase conjugate reflectivity, and improve the uniformity of the reflectivity and the fidelity of the phase-

conjugation beam. In the following, we first show the experimental results and then discuss some of the possible mechanisms.

6.2 Experimental results of SPPC enhancements

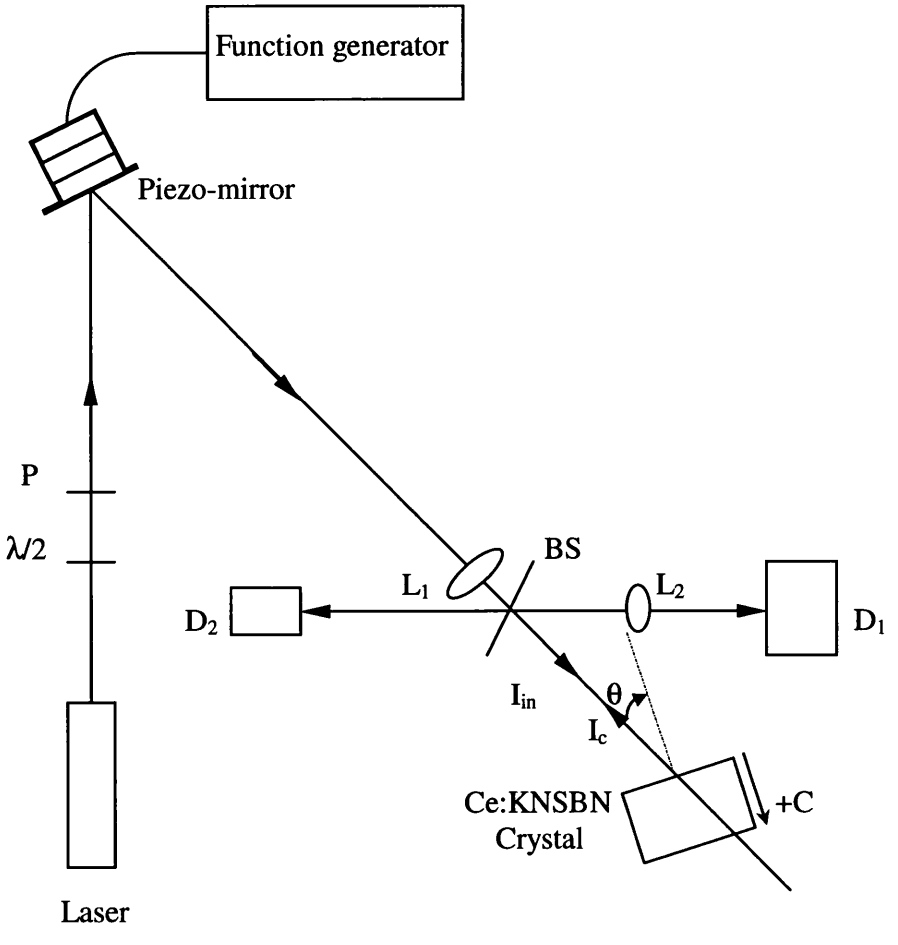

Fig. 6.1 Schematic diagram for SPPC enhancement experiment. λ/2: half wave plate; P: polarizer; L_1, L_2: lens; BS: beam splitter and D_1, D_2: detectors.

Fig. 6.1 is the experimental setup of the self-pumped phase-conjugation by Doppler frequency detuning. The extraordinary input beam (λ = 632.8 nm) comes from a helium-neon laser. The $\lambda/2$ half wave plate and the Polarizer are used to adjust the polarization directions of the extraordinary beam. The lens $L_1(f$ = 450 cm) is used to slightly adjust the beam diameter incident on the Ce:KNSBN crystal (the incident beam diameter is about 0.2 mm in our experiment). The beam-splitter reflects part of incident beam to D_2, which monitors the fluctuation of the incident intensity (I_{in}), and reflects the phase conjugation beam (I_c) to detector D_1. And L_2 focuses the SPPC beam to D_1. The c axis of the crystal is in the same plane of the polarization direction of input beam, the plane of the paper. θ is the angle between the propagation direction of the incident beam and the c axis of the crystal. A piezo-mirror is used to create the Doppler frequency detuning.

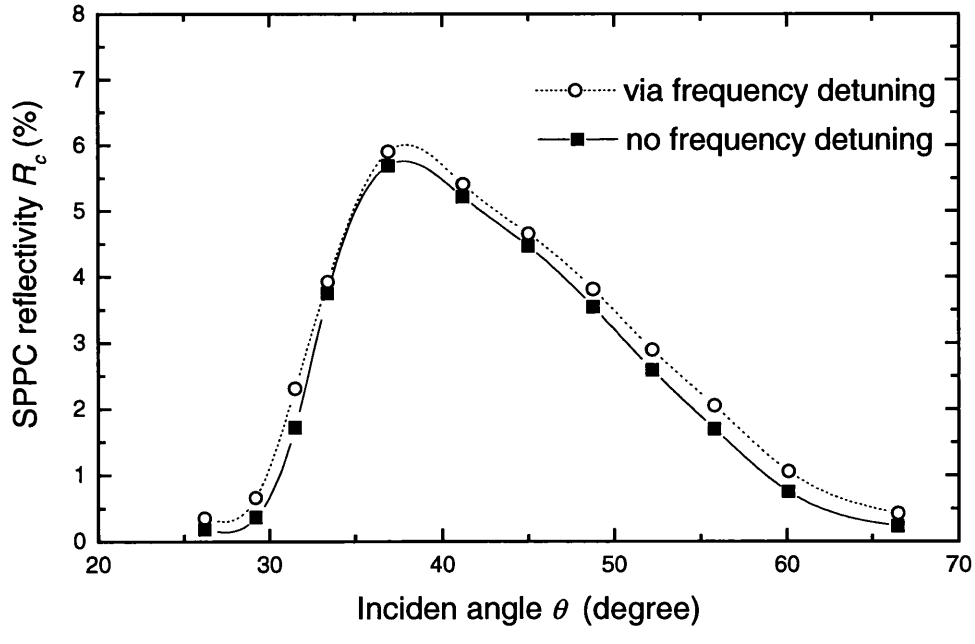

Fig. 6.2 SPPC reflectivity via Doppler frequency detuning at different incident angles (X = 2.5 mm).

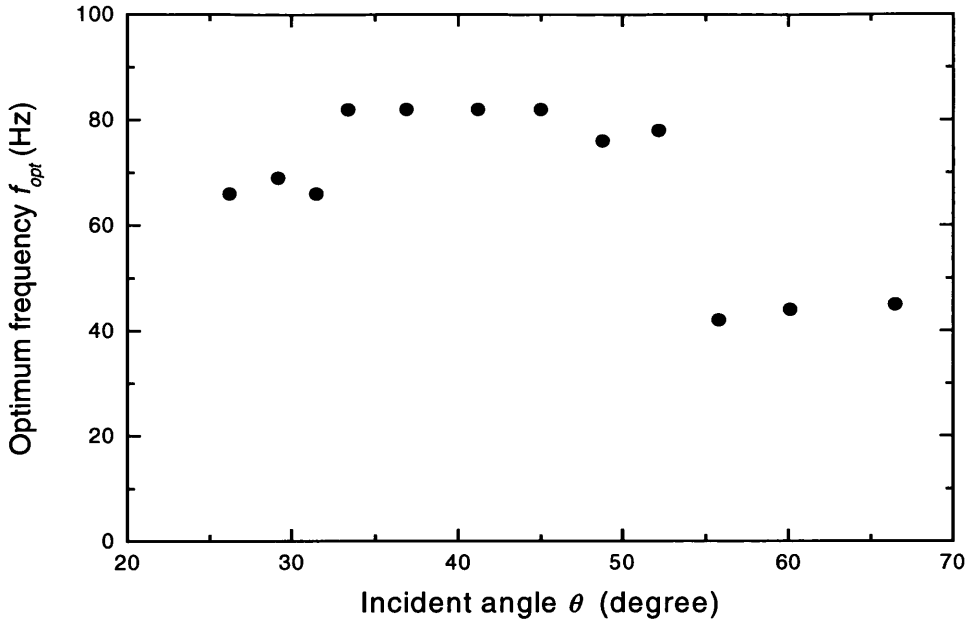

Fig. 6.3 Optimum detuning frequency for SPPC enhancement (X = 2.5 mm)

Fig. 6.2 shows the effect of the Doppler frequency detuning on the phase-conjugate reflectivity respect to incident angle θ under the conditions X = 2.5 mm (where X is the distance of the incident point from the left edge of the crystal). For each incident angle θ we first measured the SPPC reflectivity without frequency detuning, and then switched on the Function Generator (HP 33120A), which connected to a LVPZ controller (PI P-862), using a burst function to act on the piezo-mirror. For different detuning frequencies, the enhanced SPPC reflectivity could be changed. We recorded the maximum SPPC reflectivity related to the optimum frequency f_{opt}. (Fig. 6.3 shows the optimum detuning frequency versus the incident angle. In some ranges of the incident angle, the optimum frequencies were almost same. In this experiment there roughly existed three ranges, i.e.

$\theta < 33°$, $33° \leq \theta \leq 54°$ and $\theta > 54°$. The corresponding optimum frequencies were about 68Hz, 82Hz, and 44Hz). It can be seen that the Doppler frequency detuning technique enhances the SPPC reflectivity for all the incident angles.

If we define the SPPC enhancement coefficient G_e as follows

$$G_e = \frac{R_D - R_N}{R_N} \times 100\% \tag{6.1}$$

where R_D is the SPPC reflectivity at optimum Doppler frequency detuning, and R_N is that without Doppler frequency detuning, and plot the curve of the SPPC enhancement versus the incident angles (as shown in Fig. 6.4), we can find that the enhancement is quite obvious in the ranges where the SPPC reflectivities without Doppler frequency

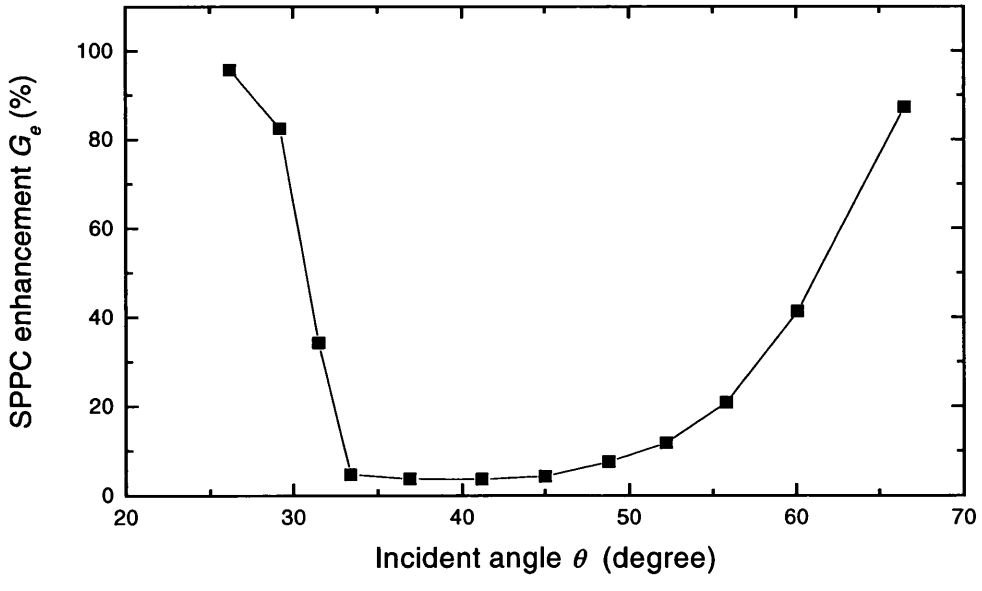

Fig. 6.4 SPPC enhancement at different incident angles (X = 2.5 mm)

detuning are relatively small. For the ranges of incident angle $\theta < 30°$ and $\theta > 65°$ the SPPC enhancement is over 80%. While in the range where the SPPC reflectivity without Doppler frequency is relatively high, the detuning contribution is less, for the range of incident angle $34° < \theta < 45°$, the SPPC enhancement is only about 4%.

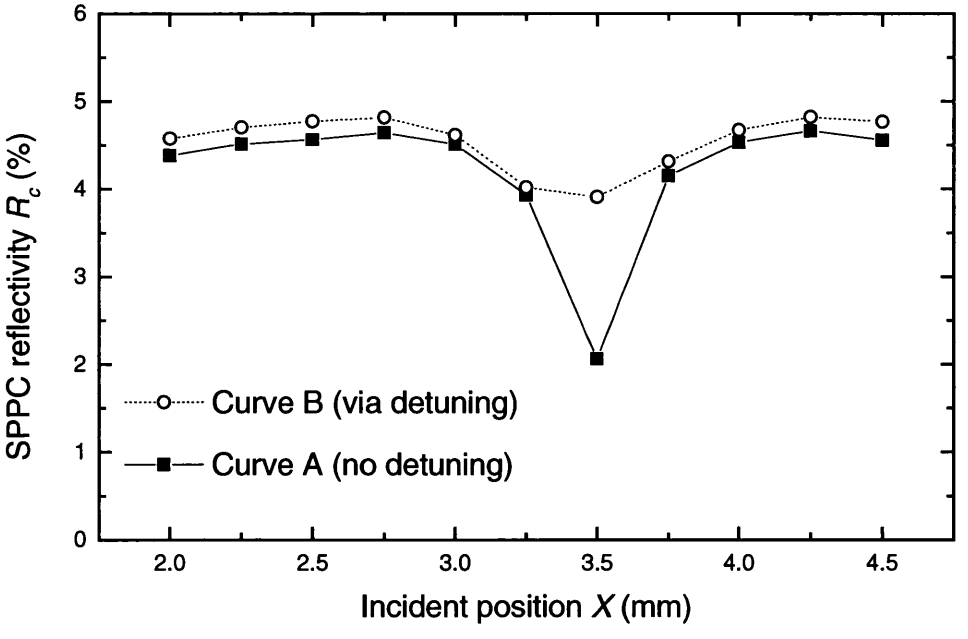

Fig. 6.5 SPPC reflectivity versus incident position at incident angle θ =45°

Fig. 6.5 shows the variation of the SPPC reflectivity with respect to the incident position on the crystal with certain incident angle ($\theta = 45°$). Curve A is obtained without Doppler frequency detuning, and curve B is obtained with the optimum Doppler frequency detuning. It can be seen that Doppler frequency detuning works at all data points, and the

poorer SPPC acquires higher enhancement. At the position X = 3.5mm, since the incident beam met the lower-right corner of the crystal (refer to the loops in Fig. 5.14), the SPPC reflectivity without frequency detuning was much lower compared to other positions (the SPPC reflectivity at X = 3.5mm was 2%, and it was between 3.9% and 4.6% at other positions). The Doppler frequency detuning enhanced the SPPC reflectivity at X = 3.5mm to 3.9%, the enhancement reached 90% at this specific point, while the enhancements are about 4.5% at other positions.

The above results seem that the Doppler frequency detuning technique not only enhances the SPPC reflectivity, but also makes the uniformity of the reflectivity over a certain area much better. To show this point we define the maximum deviation σ_{MAX} and the average deviation σ_{AVE} of the SPPC reflectivity as

$$\sigma_{MAX} = \frac{R_{MAX} - R_{MIN}}{R_{AVE}} \tag{6.2}$$

$$\sigma_{AVE} = \frac{\sum_{1}^{N} |R_c - R_{AVE}|}{N R_{AVE}} \tag{6.3}$$

where R_{MAX}, R_{MIN} and R_{AVE} are the maximum, minimum and average of the SPPC reflectivity, respectively, and N is the number of the measurement data. From curve A we obtained the maximum deviation and the average deviation of the SPPC reflectivity without Doppler frequency detuning were σ_{MAX} = 0.62 and σ_{AVE} = 0.11, and from curve

B we got the related deviations with Doppler frequency detuning were $\sigma_{MAX} = 0.20$ and $\sigma_{AVE} = 0.056$, respectively. It can be seen that the improvement of the uniformity of the reflection is attractive.

In our experiments the SPPC enhancement happened for most Doppler detuning frequencies, however, for certain conditions there always existed an optimum frequency where we could get the maximum SPPC enhancement. Fig. 6.6 and Fig. 6.7 show the SPPC enhancement depending on the detuning frequency at the conditions of $X = 2.5$mm, $\theta = 30°$ and $X = 2.0$mm, $\theta = 58°$ respectively. For the condition of $X = 2.5$mm, $\theta = 30°$ (Fig. 6.6), in the frequency range of $30Hz < f < 100Hz$, there exist two peaks at $f_1 =$ 44Hz and $f_2 = 68$Hz, the related SPPC enhancement achieve $Ge_1 = 73\%$ and $Ge_2 = 98\%$.

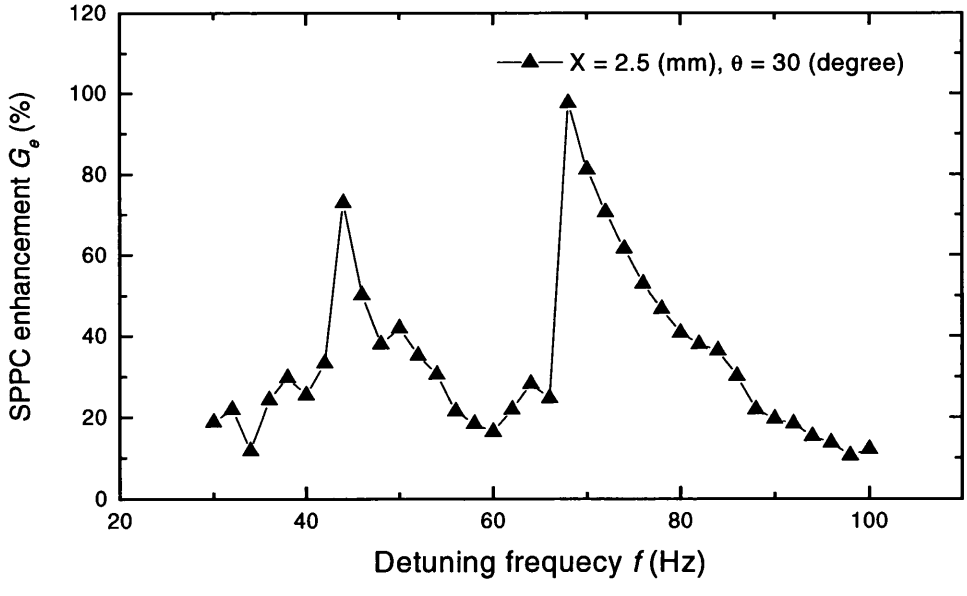

Fig. 6.6 SPPC enhancement versus detuning frequency at the conditions of X = 2.5mm, $\theta = 30°$.

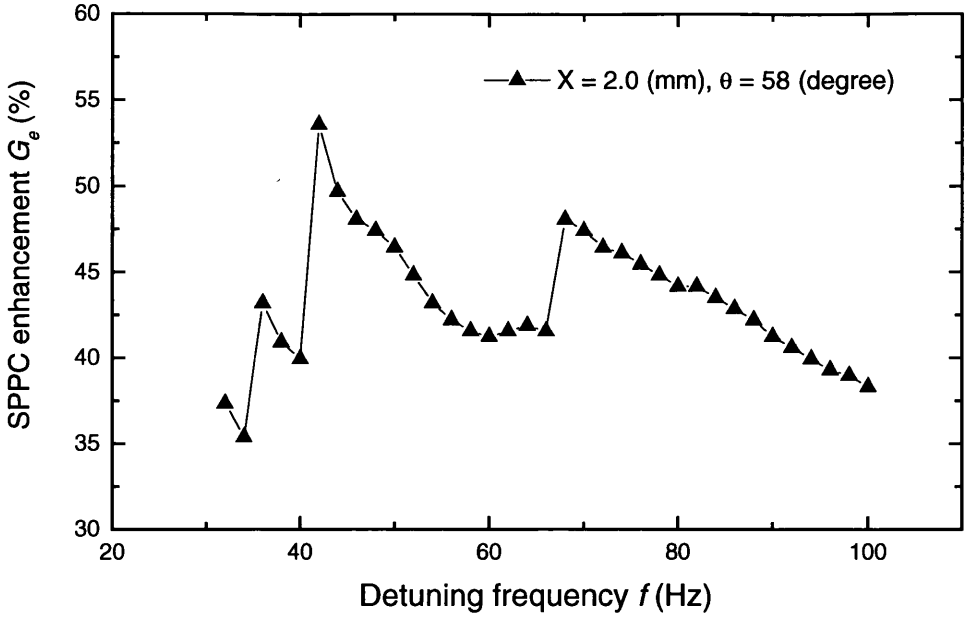

Fig. 6.7 SPPC enhancement versus detuning frequency at the conditions of X = 2.0mm, θ = 58° respectively.

While the SPPC enhancement for most detuning frequencies is around 20%. We treat f_2 = 68Hz as the optimum detuning frequency, which related the maximum SPPC enhancement (98%), for this condition. For the condition of X = 2.0mm, θ = 58° (Fig. 6.7), in the frequency range of $30Hz < f < 100Hz$, there also exist two peaks at f_1 = 42Hz and f_2 = 68Hz, the related SPPC enhancement achieve G_1 = 54% and G_2 = 48% respectively. We treat f_1 = 42Hz as the optimum detuning frequency, which related the maximum SPPC enhancement (54%). Although the optimum detuning frequency was arbitrary in our experiment, there were some specific frequencies such as 44Hz and 68Hz

(also referred to Fig. 6.3) seemed specific for our phase conjugation configuration in some conditions.

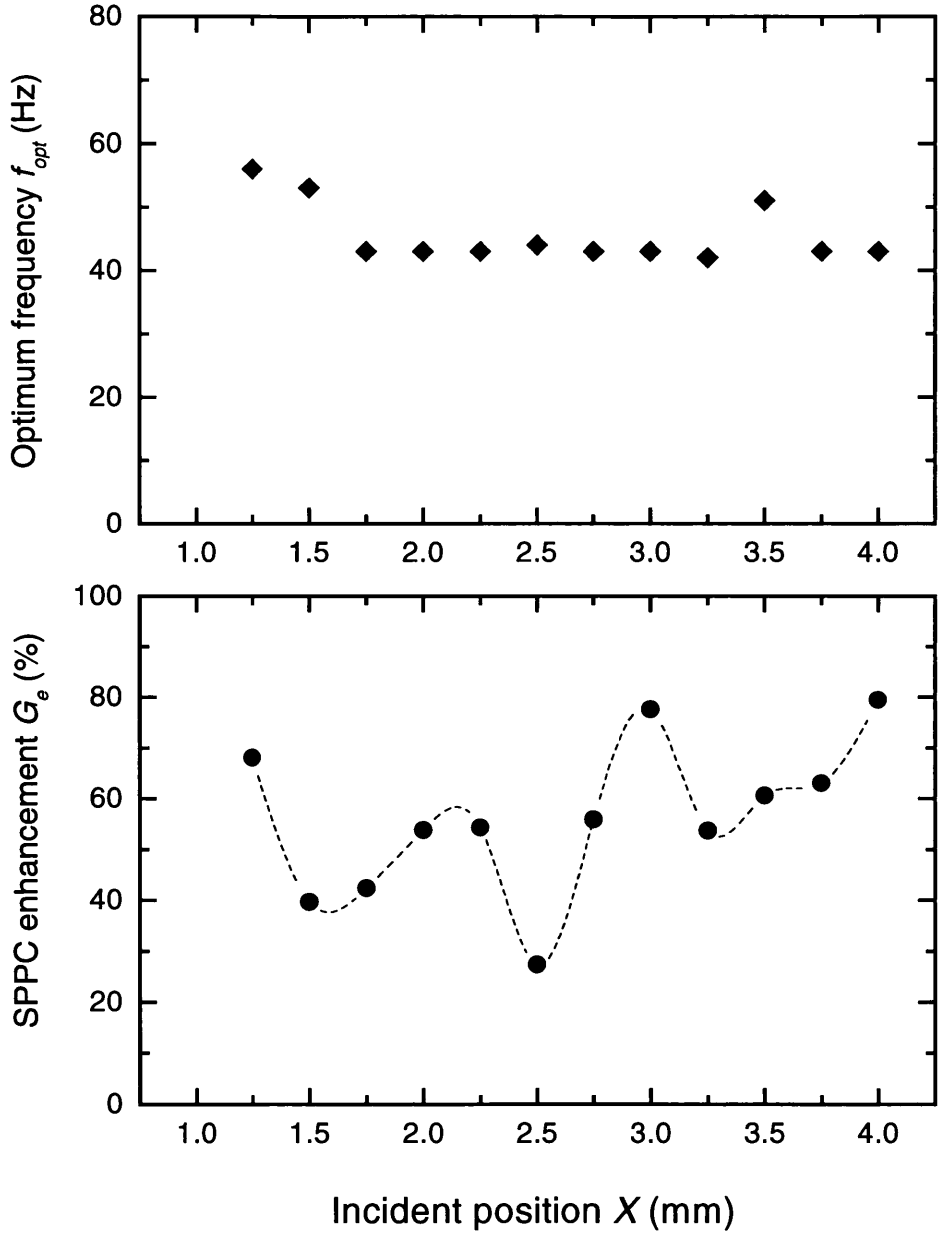

Fig. 6.8 SPPC enhancement and optimum detuning frequency versus incident position at incident angle of $\theta = 58°$.

Fig. 6.8 shows the experimental results of the dependence of the optimum Doppler detuning frequency on the incident position, and the related SPPC enhancement at the incident angle $\theta = 58°$. Generally the optimum Doppler detuning frequency and the SPPC enhancement varies arbitrarily in the range of $1.25mm \leq X \leq 4.0mm$. However, in the ranges of $1.75mm \leq X \leq 3.25mm$ and $3.75mm \leq X \leq 4.0mm$, we can find that the optimum detuning frequency almost keeps the same as $f_{opt} \approx 43Hz$. If we could get an appropriate detuning frequency in the experiment, with this frequency the uniformity of the SPPC reflectivity could be considerably improved, and the Doppler frequency detuning technique would be very useful in applications.

Fig. 6.9 shows the SPPC reflectivity versus incident position at $\theta = 58°$ for different conditions: a) without Doppler frequency detuning; b) with detuning at related optimum frequencies; and c) with detuning at the fixed frequency $f \approx 43Hz$. Table 6.1 gives the

Table 6.1 The deviation calculation for different conditions at incident angle $\theta = 58°$

	Without detuning	Optimum frequency Detuning	Fixed frequency $f \approx 43Hz$
Maximum deviation σ_{MAX}	0.35	0.17	0.25
Average deviation σ_{AVE}	0.098	0.053	0.067

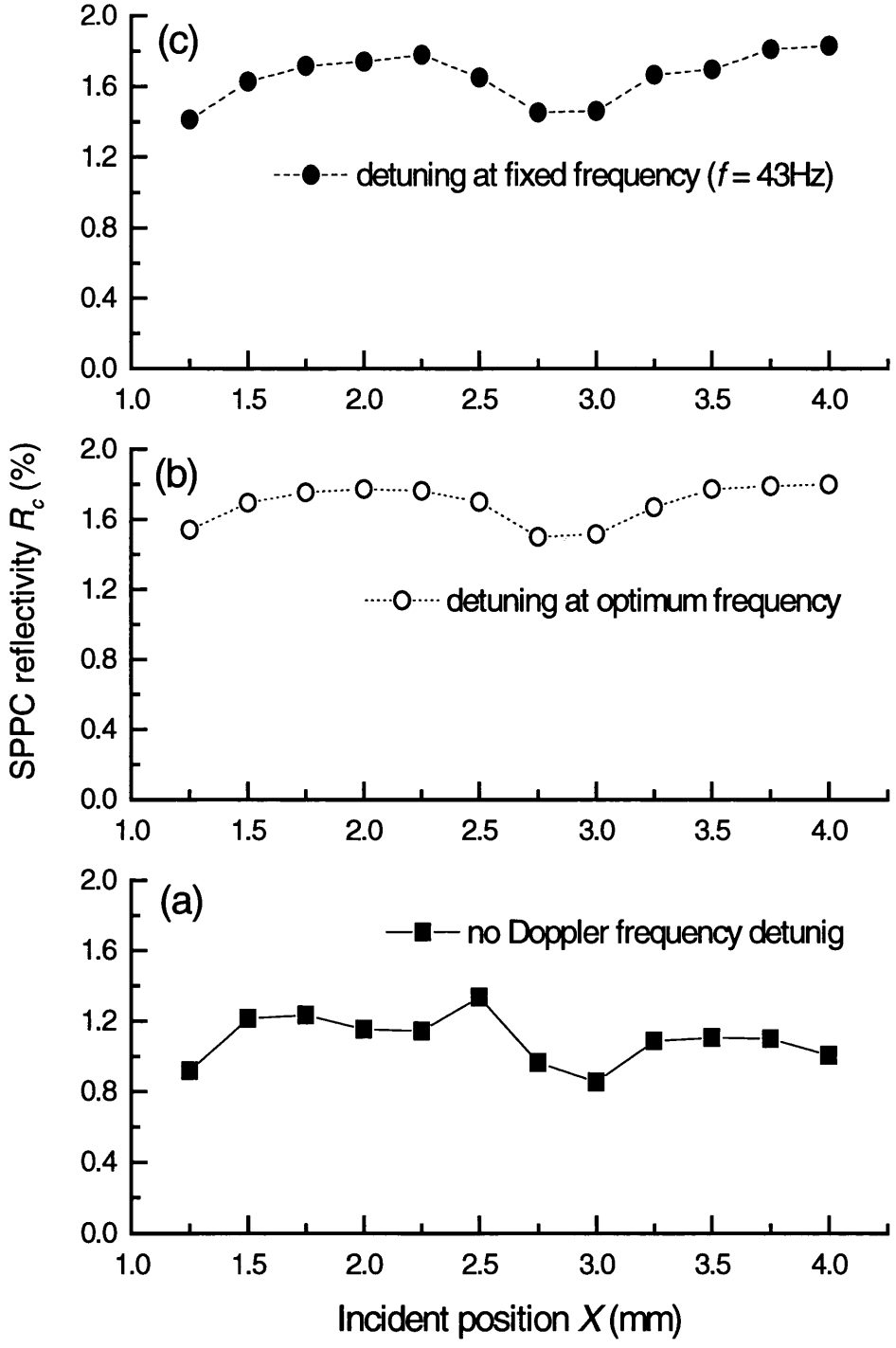

Fig. 6.9 SPPC reflectivity versus incident position at $\theta = 58°$.

corresponding maximum deviation σ_{MAX} and average deviation σ_{AVE} calculated by Eqs. (6.2) - (6.3). We find that the uniformity of the SPPC reflectivity was really improved by the appropriate detuning frequency $f \approx 43Hz$ at this experimental condition, the maximum deviation was improved from 0.35 to 0.25 and average deviation was from 0.098 to 0.067.

Fig. 6.10 shows the effect of the Doppler frequency detuning on the fidelity of the phase conjugate beam, the pump beam incident angle is $\theta = 58°$ (In the experimental set-up of Fig. 6.1, we used a CCD camera to replace the detector D_1). The top one (a) is the normal SPPC beam spot, and the bottom (b) is the SPPC beam spot with Doppler frequency detuning at optimum value, $f \approx 43Hz$. It can be seen that the intensity distribution of the phase conjugate beam is somewhat distorted (the profile of incident beam from He-Ne laser is a Gaussian distribution). The distortion of the phase conjugate beam is largely corrected when we applied the Doppler frequency detuning into the system. It seems that the Doppler frequency detuning technique would be very useful in the application of image replica using phase conjugation configurations.

6.3 Mechanisms for SPPC enhancements

The idea of SPPC enhancement via Doppler frequency detuning was based on the phenomena we found in our experiment: 1) when the intensity of light incident on the CAT conjugator was suddenly increased or decreased to certain value, the SPPC beam

(a)

(b)

Fig. 6.10 The phase conjugate beam spots at the conditions of X = 2.0mm, θ = 58°: a) without Doppler frequency detuning; b) with Doppler frequency detuning at $f \approx 43Hz$.

could achieve a peak instantly and then decay to a normal intensity which corresponded to that intensity value of incident light; 2) when the position of light incident on the CAT conjugator was suddenly changed to a new one, the SPPC beam could achieve a peak instantly and then decay to a normal intensity which corresponded to that new position. These phenomena suggested that the process of changing the incident light would transiently enhance phase conjugate beam, while a sudden change in the input power could cause a transient frequency shift of the phase conjugate beam [4]. Thus the Doppler frequency detuning seems to be capable of getting SPPC enhancement. We have demonstrated the SPPC enhancement via Doppler frequency detuning on the CAT conjugator. However, the physical origin of this enhancement is uncertain. Here we only discuss some of the possible mechanisms.

1) *Pyroelectric field.* The incident light via Doppler frequency detuning on a CAT conjugator has both a frequency shift towards the red end of the spectrum, and, conversely, a blue shift. This transient effect will cause a thermal unequilibrium state in the crystal [4], which probably produces a pyroelectric field. The extra pyroelectric field would not only increase the coupling strength between the pumping beams in the closed loop inside the CAT conjugator, and hence enhance SPPC reflectivity, but also smooth the field distribution in different positions of the crystal, and improve the fidelity of the phase conjugate beam. Obviously an effective pyroelectric field would be dependent on the proper detuning frequency as the optimum frequency mentioned in our experiment.

2) *Resonator condition.* As we mentioned in Section 5.3, in the case of a unidirectional ring resonator (see Fig. 5.2(c)), the oscillation between the two mirrors provides the counterpropagating beams which are needed in phase conjugation via four-wave mixing. This kind of resonator has two interesting properties: (i) the oscillating beam generally has a slight different frequency than the pumping beam [5]; (ii) oscillation occurs almost regardless of the optical path length of the cavity, even when only one spatial mode is allowed to oscillate. These two properties are related, and it has been shown that for (almost) any resonator length, the frequency shift between the resonator beam and the pumping beam could supply the correct amount of phase to satisfy the resonator condition [6,7]. It was also found theoretically [8] there is a frequency shift between the counterpropagating bi-directional oscillation beams in ring resonators. In a CAT conjugator, the crystal surfaces provide the mirror reflection needed in the bi-directional ring oscillation. We observed that the self-generated pumping beams form a closed loop in our experiment (see Fig. 5.4). However, in CAT phase conjugators, the length of the resonator is not well defined, there probably exist many oscillating modes, each having a different frequency shift [5, 9]. Obviously the Doppler frequency detuning could help the circulating beams to satisfy the resonator condition related to the frequency shift, hence to receive the SPPC enhancement.

6.4 Conclusions

In conclusion we have applied Doppler frequency detuning technique into SPPC to improve the SPPC beam. More than 80 % enhancement of the reflectivity is achieved at certain incident positions and incident angles with the optimum Doppler detuning frequency. The uniformity of the reflectivity over a reasonable area is considerably improved with an appropriate fixed Doppler detuning frequency. The distortion of the SPPC beam, especially at the worst positions, is largely corrected by the technique.

The possible mechanisms of SPPC enhancement have been discussed. In this demonstration, the phase conjugate efficiency was not very high for the crystal used. It is no doubt that with a good sample of the crystal, a much higher phase conjugate reflectivity can be obtained with the proposed technique.

Chapter 6: Reference

1. K. R. MacDonald and J. Feinberg, "Enhanced four-wave mixing by use of frequency-shifted optical waves in photorefractive $BaTiO_3$", Phys. Rev. Lett., vol. 55, p821, 1985
2. D. M. Bloom and G. C. Bjorklund, "Conjugate wave-front generation and image reconstruction by four-wave mixing", Appl. Phys. Lett., vol. 31, p592, 1977

3. K. R. MacDonald and J. Feinberg, "Theory of a self-pumped phase conjugator with two coupled interaction regions", J. Opt. Soc. Amer, vol. 73, No. 5, pp548-553, 1983

4. M. C. Gower, "Photoinduced voltages and frequency shifts in a self-pumped phase conjugating $BaTiO_3$ crystal", Opt. Lett., vol. 11, p458, 1986

5. J. Feiberg, G. D. Bacher, " Self-scanning of a continuous-wave dye laser have a phase-conjugating resonator cavity", Opt. Lett., vol. 9, p420, 1985

6. P. Yeh, "Theory of unidirectional photorefractive ring oscillators", J. Opt. Soc. Am. B, vol. 2, p1924, 1985

7. A. Yariv, S. K. Kwong, "Theory of laser oscillation in resonators with photorefractive gain", Opt. Lett., vol. 10, p454, 1985

8. P. Yeh, "Photorefractive coupling in ring resonators", Appl. Opt., vol. 23, p2974, 1984

9. M. Cronin-Golomb and A. Yariv, "Plane-wave theory of nondegenerate oscillation in the linear photorefractive passive phase-conjugate mirror", Opt. Lett., vol. 11, p242, 1986

Chapter 7 Summary

The doped KNSBN photorefractive crystals have attracted the attention of researchers recently due to their excellent properties including large electro-optic coefficients, a relatively high Curie temperature, single domain, good mechanical properties, and appropriate spectrum response. Cu, Ce, Cr and Mn dopants have been added to the melt during crystal growth to modify the photorefractive properties of KNSBN crystals. However, most researchers have only focused on the investigations of the Cu:KNSBN crystals.

The properties of the Ce:KNSBN crystal were investigated thoroughly in our work. Using different methods based on two wave mixing theory at zero applied electric field, we measured, derived and calculated most photorefractive parameters of the Ce:KNSBN crystal, such as coupling gain coefficient, intensity absorption, effective photorefractive charge density, product of effective electro-optic coefficient and hole-electron competition factor, product of carrier mobility and recombination time constant, dark conductivity, and etc. We found that most parameters of the Ce:KNSBN crystal were in the same orders with those of the Cu:KNSBN crystal. However, the maximum coupling gain coefficient of Ce:KNSBN (Γ_{max} = 3.6 cm^{-1}) is about 6 times less than Γ_{max} of Cu:KNSBN, and the product of carrier mobility and recombination time constant $\mu\tau_R$ for Ce: KNSBN crystal is about 5 times greater than the product of $\mu\tau_R$ for Cu:KNSBN. Ce-

doping and Cu-doping KNSBN crystals have some competitive properties in this new photorefractive material family.

We observed the effects of applied electric fields on the diffraction efficiency in the Ce:KNSBN crystal. The rise-time of the diffraction becomes less while the applied electric field increases, and the application of the applied electric field enhances the diffraction efficiency. In our experiment there existed the optimum applied electric field and the optimum grating spacing related to the maximum diffraction efficiency, although the theoretical calculations showed that diffraction efficiency would increase with the applied electric field and the grating spacing as well. We also found that the history of the applied electric field could influence the value of diffraction efficiency. Such phenomenon could not be simply explained by the hysteresis of ferroelectric materials. We think that some effects, such as strong fanning and thermal effect, should be considered when an electric field is applied to the Ce:KNSBN crystal.

We demonstrated the phase conjugate properties in Ce:KNSBN crystal for different configurations. In the four-wave mixing configuration, we find that the experimental results of the phase conjugate reflectivity agree with the theoretical expression based on the one-grating approximation (for relative high incident intensity), although the interaction mechanism of FWM phase conjugate is exceedingly complicated. In the self-pumped phase conjugation based on total internal reflection (CAT configuration), we used the extraordinary incident beams from a He-Ne laser light and an argon-ion laser as well. We observed the same phenomena as those from other tungsten-bronze crystals of

point group 4 mm for both beams, i.e. the self-generated pumping beams form a closed loop inside the crystal, and the SPPC is sensitive to the incident angle, and there exist an optimum angle, to which the SPPC reflectivity is almost symmetrical. However, we found that the He-Ne laser light could generate higher SPPC reflectivity than that by the argon-ion laser (by as much as a factor of 6), with a relatively low threshold of incident angle. We also observed an anomalous SPPC reflectivity dependence on incident power, i.e. the SPPC reflectivity dropped when the incident power was larger than 10 mW (the SPPC reflectivity is independent on the incident power in the well-accepted SPPC theory). Further research on its nature may be useful for understanding the mechanism of the photorefractive effect in Ce:KNSBN crystal.

An especially important result was that we first, to our knowledge, applied Doppler frequency detuning technique to the SPPC CAT configuration. In our experiment we demonstrated that Doppler frequency detuning could not only enhance the SPPC reflectivity, but also improve the uniformity of the reflectivity over a reasonable area. Possible mechanisms for these results are discussed.

In conclusion, we have studied the photorefractive properties of the Ce:KNSBN crystal. We found some new phenomena and special characteristics in the application for the CeKNSBN crystal, which have not been reported for other photorefractive materials, and we explained those phenomena by some possible mechanisms. In the future we plan to get more Ce:KNSBN crystals, with different sizes, to investigate the properties of

Ce:KNSBN material in more detail, and further to confirm some phenomena in our experiments and the mechanisms we suggested.

Appendix List of publications

1. H. Zhang, C. Cartwright, M. Ding, and A. Gillespie, Image feature extraction with wavelet transforms in a photorefractive joint transform correlator, Optics Communications (to be accepted)
2. H. Zhang, C. M. Cartwright, M.S. Ding and A. Gillespie, Optical implementation of a photorefractive joint transform correlator with wavelet filters, Optics Communications, **181** (2000) pp223-230
3. H. Zhang, C. M. Cartwright, M.S. Ding, Z.Q. Wang, N.J. cook and A. Gillespie, Experimental implementation of a photorefractive joint transform correlator with circular harmonic filters, Optics Communications, **173** (2000) pp129-136
4. M.S. Ding, C. M. Cartwright, H. Zhang and A. Gillespie, The effect of applied electric field history on the diffraction efficiency of Ce:KNSBN, Trends in Optical and Photonics, **17** (1999) pp380-382
5. H. Zhang, C. M. Cartwright, M.S. Ding and A. Gillespie, A triple joint transform correlator, SPIE proceeding, **3715** (1999) pp185-196
6. Zhaoqi Wang, Hui Zhang, Colin M. Cartwright, Meisong Ding, Nick J. Cook and W. Allan Gillespie, Edge enhanced optical correlation by the use of moving grating in BSO crystal and its application to optical correlation, Applied Optics, **37** (1998) pp4449-4456
7. H. Zhang, Z. Q. Wang, C. M. Cartwright, M. S. Ding, N. J. Cook and W. A. Gillespie, A circular harmonic quantized amplitude compensated matched filter, Optik, **109** (1998) p119-123

8. Z. Q. Wang, H. Zhang, C. Cartwright, M. Ding, N. Cook, W. Gillespie, "A Fresnnel lens-encoded quantized amplitude-compensated matched filter with circular harmonic expansions", Journal of Optoelectronics Laser, **9** (1998) pp179-185